UNIVERSIDADE FEDERAL DE SANTA CATARINA
CENTRO TECNOLOGICO
PROGRAMA DE PÓS-GRADUAÇÃO EM ENGENHARIA MECÂNICA

Alexandre Neves Trichez Júnior

**Changes in contact mechanics of the glenohumeral joint in the presence of osseous defects: a numerical study**

Florianópolis
2024

Alexandre Neves Trichez Júnior

**Changes in contact mechanics of the glenohumeral joint in the presence of osseous defects: a numerical study.**

Tese submetida ao Programa de Pós-Graduação em Engenharia Mecânica da Universidade Federal de Santa Catarina como requisito parcial para a obtenção do título de Doutor em Engenharia Mecânica na área de Análise e Projeto Mecânico.

Orientador: Prof. Eduardo Alberto Fancello, Dr.
Coorientador: Prof. Carlos Rodrigo de Mello Roesler, Dr.

Florianópolis
2024

Trichez Junior, Alexandre Neves
Changes in contact mechanics of the glenohumeral joint in the presence of osseous defects: a numerical study / Alexandre Neves Trichez Junior ; orientador, Eduardo Alberto Fancello, coorientador, Carlos Rodrigo de Mello Roesler, 2024.
143 p.

Tese (doutorado) - Universidade Federal de Santa Catarina, Centro Tecnológico, Programa de Pós-Graduação em Engenharia Mecânica, Florianópolis, 2024.

Inclui referências.

1. Engenharia Mecânica. 2. Método dos Elementos Finitos. 3. Articulação Glenoumeral. 4. Estabilidade Articular. 5. Defeitos Ósseos. I. Fancello, Eduardo Alberto. II. Roesler, Carlos Rodrigo de Mello. III. Universidade Federal de Santa Catarina. Programa de Pós-Graduação em Engenharia Mecânica. IV. Título.

Alexandre Neves Trichez Júnior

**Changes in contact mechanics of the glenohumeral joint in the presence of osseous defects: a numerical study.**

O presente trabalho em nível de Doutorado foi avaliado e aprovado, em 23 de Setembro de 2024, pela banca examinadora composta pelos seguintes membros:

Prof. Arnaldo Amado Ferreira Neto, Dr.
Universidade de São Paulo

Prof. Jakson Manfredini Vassoler, Ph.D.
Universidade Federal do Rio Grande do Sul

Prof. Heiliane de Brito Fontana, Dra.
Universidade Federal de Santa Catarina

Certificamos que esta é a versão original e final do trabalho de conclusão que foi julgado adequado para obtenção do título de Doutor em Engenharia Mecânica

ICP-Edu
Documento assinado digitalmente
**Henrique Simas**
Data: 20/03/2025 19:27:02-0300
CPF: ***.194.639-**
Verifique as assinaturas em https://v.ufsc.br

Coordenação do Programa de Pós-Graduação

ICP-Edu
Documento assinado digitalmente
**Eduardo Alberto Fancello**
Data: 19/03/2025 14:20:16-0300
CPF: ***.089.757-**
Verifique as assinaturas em https://v.ufsc.br

Prof. Eduardo Alberto Fancello, Dr.
Orientador

Florianópolis, 2024.

To myself.

## AGRADECIMENTOS

A conclusão deste trabalho só foi possível graças ao apoio e contribuição de muitas pessoas e instituições, a quem gostaria de expressar minha profunda gratidão.

Primeiramente, agradeço ao meu orientador, Prof. Dr. Eduardo Alberto Fancello, por sua orientação, paciência e por compartilhar seu vasto conhecimento ao longo de todo o desenvolvimento desta pesquisa. Suas sugestões e conselhos foram fundamentais para o amadurecimento das ideias e para a evolução do trabalho. Ao meu coorientador, Prof. Dr. Carlos Rodrigo de Mello Roesler, meu agradecimento pelo apoio técnico, pelas contribuições valiosas ao projeto e por todas as oportunidades.

Agradeço também aos professores que participaram da minha banca de qualificação e defesa, cujas sugestões enriqueceram este trabalho, em especial aos Professores Drs. Jakson Manfredini Vassoler e Arnaldo Amado Ferreira Neto, e à professora Dra. Heiliane de Brito Fontana. A todos os docentes do programa de pós-graduação, minha gratidão pelos ensinamentos ao longo desses anos.

À CAPES e ao CNPq, agradeço pelo apoio financeiro que viabilizou a realização deste projeto, e ao Laboratório de Engenharia Biomecânica e ao GRANTE pelo espaço e equipamentos disponibilizados para a realização dos trabalhos.

Sou imensamente grato aos meus colegas de laboratório, em especial Bruno, Otávio, José, Jonas, Matheus, Guilherme e Luiza, pela parceria, pelas discussões científicas e pelo companheirismo em momentos de desafios. Sem vocês, essa jornada teria sido muito mais difícil.

À minha família, especialmente aos meus pais Alexandre e Marcia, que sempre me incentivaram e acreditaram em meu potencial, mesmo nos momentos em que duvidei de mim mesmo. Suas palavras de apoio e amor incondicional foram meu maior combustível. Agradeço também à Marina, minha companheira de vida, por sua paciência, carinho e compreensão durante todos os momentos de tensão e dedicação ao longo desta trajetória.

Por fim, a todos os amigos que, de alguma forma, me ajudaram a manter o equilíbrio e o bom humor em meio aos desafios da vida acadêmica, meu muito obrigado.

A todos vocês, dedico este trabalho.

*"And so, does the destination matter? Or is it the path we take? I declare that no accomplishment has substance nearly as great as the road used to achieve it. We are not creatures of destinations. It is the journey that shapes us. Our callused feet, our backs strong from carrying the weight of our travels, our eyes open with the fresh delight of experiences lived."* (Brandon Sanderson, The Way of Kings)

## RESUMO

A articulação glenoumeral, inerentemente instável devido à sua geometria, pode estar sujeita a luxações anteriores do ombro que causam rompimento dos tecidos moles e defeitos ósseos, comprometendo a estabilidade articular. Esta tese apresenta um modelo computacional para analisar a mecânica de contato da articulação glenoumeral na presença de defeitos ósseos na borda anterior da glenoide, visando preencher a lacuna nas avaliações quantitativas de como tamanhos variados de defeitos afetam a estabilidade da articulação e a mecânica de contato. Utilizando análise em elementos finitos e modelagem de corpo rígido, a biomecânica da articulação glenoumeral é simulada, focando em tamanhos de defeitos de 0 mm a 6 mm. O modelo incorpora cartilagens com superfícies articulares elipsoidais e não congruentes e considera as mudanças nas direções das forças musculares devido às translações da cabeça do úmero. Os resultados revelam que a estabilidade é mantida para ângulos de abdução superiores a 90° com defeitos de até 4 mm. O aumento do tamanho do defeito altera significativamente as forças de reação articular, a pressão de contato máxima e a largura da trilha da glenoide. No entanto, o tamanho do defeito não afeta significativamente a área de contato e as translações da cabeça do úmero. Visualizações e dados quantitativos indicam uma relação direta entre o tamanho do defeito e o comprometimento mecânico da articulação, destacando o impacto crítico de defeitos moderados na função e estabilidade articular. Em conclusão, esta pesquisa avança na compreensão da biomecânica da articulação glenoumeral, oferecendo uma abordagem computacional refinada para avaliar o impacto de defeitos ósseos anteriores na mecânica de contato articular e nas translações da cabeça do úmero.

**Palavras chaves:** MEF, articulação glenoumeral, modelo do ombro, estabilidade articular, defeitos ósseos.

**ABSTRACT**

The glenohumeral joint, inherently unstable due to its geometry, may be subjected to anterior shoulder dislocations that cause soft tissue detachments and osseous defects, compromising joint stability. This thesis develops a computational model to analyze the contact mechanics of the glenohumeral joint in the presence of osseous defects in the anterior border of the glenoid, aiming to bridge the gap in quantitative assessments of how varying defect sizes affect joint stability and contact mechanics. Utilizing finite element analysis and rigid body modeling, we simulate the glenohumeral joint's biomechanics, focusing on defect sizes from 0 mm to 6 mm. The model incorporates cartilages with ellipsoidal and non-congruent articular surfaces and considers the changes in muscle force directions due to humeral head translations. Results reveal that stability is maintained for abduction angles greater than 90° with defects up to 4 mm. Increasing defect size significantly alters joint reaction forces, peak contact pressure, and glenoid track width. However, the defect size does not significantly affect the contact area and humeral head translations. Visualizations and quantitative data indicate a direct relationship between defect size and the mechanical compromise of the joint, highlighting the critical impact of even moderate defects on joint function and stability. In conclusion, this research advances the understanding of glemohumeral joint biomechanics, offering a refined computational approach to evaluate the impact of anterior osseous defects on joint contact mechanics and humeral head translations.

**Keywords:** FEM, articular contact, shoulder model, joint stability, anterior osseous defects.

## RESUMO EXPANDIDO

A articulação glenoumeral, devido à sua geometria inerentemente instável, é a mais frequentemente deslocada no corpo humano. Luxações anteriores do ombro podem levar a rompimentos de tecidos moles e defeitos ósseos, comprometendo a estabilidade articular. A tese busca preencher uma lacuna no conhecimento, fornecendo avaliações quantitativas de como diferentes tamanhos de defeitos ósseos afetam a estabilidade da articulação e a mecânica de contato. Estudos anteriores focaram em determinar tamanhos críticos de defeitos para indicar a necessidade de enxerto ósseo, mas sem detalhar o impacto mecânico de diferentes tamanhos. Este trabalho avança nesse campo, utilizando um modelo computacional para simular a biomecânica da articulação glenoumeral.

O estudo emprega uma combinação de análise de elementos finitos (MEF) e modelagem de corpo rígido para simular a biomecânica da articulação glenoumeral. O modelo computacional inclui:

- **Geometria da Articulação**: Cartilagens com superfícies articulares elipsoidais e não congruentes.
- **Defeitos Ósseos**: Simulação de defeitos na borda anterior da glenoide, variando de 0 mm a 6 mm.
- **Forças Musculares**: Incorporação das mudanças nas direções das forças musculares devido às translações da cabeça do úmero. O modelo considera os músculos deltoide, supraespinhal, subescapular, infraespinhal e redondo menor, divididos em segmentos para melhor representação anatômica.
- **Movimento de Abdução**: Simulação do movimento de abdução do ombro no plano coronal, com o braço em rotação externa, e análise das forças de reação articular, pressão de contato, área de contato e translações da cabeça do úmero.
- **Rastreamento da Glenoide**: Cálculo da largura da trilha da glenoide, que corresponde à área de contato entre a glenoide e a cabeça umeral. O ponto M, localizado na borda anterior da glenoide, é projetado na

cabeça umeral, e a distância entre este ponto projetado e a margem medial da inserção do manguito rotador define a largura da trilha.

O modelo foi construído com base em dados de exames de imagem (MRI e CT) de um sujeito saudável, combinados com informações da literatura. O software Abaqus/Explicit foi utilizado para simular o movimento e o contato entre as superfícies articulares. Os resultados da simulação revelam que a estabilidade da articulação glenoumeral é mantida para ângulos de abdução superiores a 90° quando os defeitos ósseos na glenoide não excedem 4 mm. A pesquisa também encontrou que:

- **Forças de Reação Articular**: O aumento do tamanho do defeito altera significativamente as forças de reação articular, com um incremento proporcional ao tamanho do defeito.
- **Pressão de Contato**: A pressão de contato máxima também é afetada, aumentando com o tamanho do defeito.
- **Largura da Trilha da Glenoide**: A largura da trilha da glenoide diminui com o aumento do tamanho do defeito.
- **Área de Contato e Translações da Cabeça do Úmero**: Ao contrário das forças de reação articular e da pressão de contato, o tamanho do defeito não afeta significativamente a área de contato e as translações da cabeça do úmero.

Os dados quantitativos e visualizações fornecidos pelo modelo mostram uma relação direta entre o tamanho do defeito e o comprometimento mecânico da articulação. Defeitos maiores resultam em maior instabilidade e alterações nas forças de reação articular. A estabilidade foi mantida até 105° de abdução para defeitos de 3 mm e 4 mm, mas apenas até 45° para defeitos de 5 mm e 6 mm.

A pesquisa destaca que defeitos ósseos moderados têm um impacto crítico na função e estabilidade articular, corroborando estudos anteriores. A análise das forças musculares mostra que músculos como o supraespinhal, subescapular e infraespinhal desempenham um papel crucial na estabilização da articulação, com forças variando conforme o ângulo de abdução e o tamanho do defeito. O modelo computacional oferece uma análise mais detalhada da biomecânica da articulação glenoumeral do que estudos experimentais *in vivo* ou *in vitro*, que são limitados por questões éticas e tecnológicas.

A presente tese contribui significativamente para a compreensão da biomecânica da articulação glenoumeral em casos de defeitos ósseos. O modelo computacional desenvolvido fornece uma ferramenta refinada para avaliar o impacto de defeitos ósseos anteriores na mecânica de contato articular e nas translações da cabeça do úmero. A pesquisa destaca a importância de avaliações quantitativas para o planejamento de tratamentos para instabilidade do ombro, como a reparação artroscópica de Bankart ou enxertos ósseos, que são procedimentos invasivos. Os resultados desta tese têm implicações clínicas importantes. A identificação de que defeitos acima de 4 mm impactam significativamente a estabilidade da articulação glenoumeral pode ajudar os cirurgiões a tomar decisões mais informadas sobre a necessidade de intervenções cirúrgicas como enxertos ósseos. A avaliação precisa do tamanho do defeito e sua relação com a largura da trilha da glenoide é fundamental para determinar o risco de recorrência de luxações.

A tese também aponta para futuras direções de pesquisa, incluindo aprimoramentos do modelo computacional, como a incorporação de outros ligamentos e músculos, além de simulações com diferentes planos de movimento. Estudos adicionais também poderiam investigar o impacto da lesão de Hill-Sachs na estabilidade da articulação, em combinação com os defeitos da glenoide, bem como a influência do ritmo escápulo-umeral na mecânica da articulação.

Em resumo, a presente tese de doutorado oferece uma análise abrangente e detalhada da biomecânica da articulação glenoumeral em condições de defeitos ósseos, utilizando um modelo computacional avançado e validado, representando um avanço significativo no conhecimento desta complexa articulação.

**Palavras chaves:** MEF, articulação glenoumeral, modelo do ombro, estabilidade articular, defeitos ósseos.

## LIST OF FIGURES

## LIST OF TABLES

## LIST OF ACRONYMS

| | |
|---|---|
| ABR | Arthroscopic Bankar repair |
| BB | Bone bridge |
| CT | Computational tomography |
| DoF | Degrees of freedom |
| DSEM | Delft shoulder and elbow model |
| DSM | Delft shoulder model |
| DTD | Distance to dislocation |
| EMG | Electromyography |
| FDK | Force dependent kinematics |
| FE | Finite element |
| GH | Glenohumeral |
| HHT | Humeral head translation |
| HS | Hill-Sachs |
| HSI | Hill-Sachs interval |
| HSL | Hill-Sachs lesion |
| LSP | Load sharing problem |
| MRI | Magnetic resonance imaging |
| PCSA | Physiological-cross sectional area |
| RB | Rigid Body |
| SD | Standard deviation |

## LIST OF SYMBOLS

| | |
|---|---|
| $\theta$ | Abduction angle. |
| $\boldsymbol{p}$ | Arm weight vector. |
| $P$ | Arm weight amplitude. |
| $\boldsymbol{d}_p$ | Arm weight unitary vector. |
| $\boldsymbol{m}_p$ | Arm weight moment. |
| $\boldsymbol{x}_m$ | Arm weight application point. |
| $\boldsymbol{f}_m$ | Force exerted by muscle segment $m$. |
| $F_m$ | Amplitude of the force exerted by muscle segment $m$. |
| $\boldsymbol{d}_m$ | Unitary vector of the force exerted by muscle segment $m$.. |
| $\boldsymbol{m}_m$ | Moment exerted by muscle segment $m$ |
| $\boldsymbol{x}_m$ | Application point of the force exerted by muscle segment $m$. |
| $\boldsymbol{r}_a$ | Joint reaction force. |
| $\boldsymbol{r}_{a,x}$ | Component of the joint reaction force in the $x$ direction. |
| $\boldsymbol{r}_{a,y}$ | Component of the joint reaction force in the $y$ direction. |
| $\boldsymbol{r}_{a,z}$ | Component of the joint reaction force in the $z$ direction. |
| $\boldsymbol{m}_a$ | Joint reaction moment. |
| $\varepsilon_m$ | Relative residual moment. |
| $C_x$ | Glenohumeral ratio constraint in direction $x$. |
| $C_y$ | Glenohumeral ratio constraint in direction $y$. |
| $R_c$ | Joint reaction force amplitude constraint. |
| $B$ | Reduction factor for $R_c$. |
| $F_m^{max}$ | Maximum force amplitude that a muscle segment $m$ can exert. |
| $\boldsymbol{F}$ | Vector containing the amplitudes of the forces exerted by the muscles. |
| $\boldsymbol{\Omega}$ | Search space containing all the possible solutions of the LSP. |
| $\boldsymbol{m}_e$ | Estimated joint reaction moment. |
| $tol_\varepsilon$ | Specified tolerance for the relative residual moment. |
| $tol_m$ | Specified tolerance to assess the converge of the Simulation Framework. |
| $\boldsymbol{g}_\theta$ | Position of the humerus at joint angle $\theta$. |

| | |
|---|---|
| $\boldsymbol{F}_{init}$ | Vector containing the muscle force amplitudes to be used as initial population for the optimization procedure. |
| $\overline{\boldsymbol{F}}$ | Vector containing the smallest admissible amplitudes of the forces exerted by the muscles that generate mechanical equilibrium. |
| $\bar{F}_m$ | Smallest admissible amplitude of the force exerted by muscle segment $m$ that generate mechanical equilibrium. |
| $\bar{\boldsymbol{f}}_m$ | Force vector exerted by muscle segment $m$ as a function of $\bar{F}_m$. |
| $\overline{\boldsymbol{g}}_\theta$ | Position of the humerus in mechanical equilibrium at joint angle $\theta$ as a function of $\overline{\boldsymbol{F}}$. |
| $\overline{\boldsymbol{m}}_a$ | Joint reaction moment in mechanical equilibrium as a function of $\overline{\boldsymbol{F}}$. |
| $\bar{\boldsymbol{r}}_a$ | Joint reaction force as a function of $\overline{\boldsymbol{F}}$. |
| $\bar{\varepsilon}_m$ | Relative residual moment as a function of $\overline{\boldsymbol{F}}$. |
| $E$ | Young's modulus. |
| $\nu$ | Poisson's coefficient. |
| $F_{compress}$ | Compression force defined as a force perpendicular to the glenoid plane. |
| $F_{translate}$ | Tangential force defined as a force parallel to the glenoid plane. |
| $F_{translate,crit}$ | Tangential force that causes a dislocation to occur. |
| $\lambda_L$ | First Lamé parameter. |
| $\mu$ | Second Lamé parameter. |
| $\bar{\mathrm{I}}_1$ | First invariant of the isochoric part of the right Cauchy-Green deformation tensor. |
| $W$ | Elastic strain energy potential for compressible Neo-Hookean hyperelastic materials. |

## SUMMARY

# 1 INTRODUCTION

## 1.1 CONTEXT AND OBJECTIVES

The glenohumeral (GH) joint is the most frequently dislocated joint in the human body due to its inherently unstable geometry (CUTTS; PREMPEH and DREW, 2009). Unlike the acetabulum of the hip joint, the glenoid fossa is not a deep, stabilizing socket. Its small surface captures only a limited portion of the humeral articular surface, and the glenohumeral ligaments are lax in most functional positions of the joint, providing significant stabilization mostly at the extremes of joint movement (ITOI, 2017).

Anterior shoulder dislocation, in particular, can lead to detrimental outcomes such as the detachment of the anterior and anteroinferior labral complex and the development of osseous defects that compromise the concavity of the glenoid fossa (ITOI *et al.*, 2000). These alterations in the joint geometry further aggravate the instability of the glenohumeral joint, especially when the integrity of capsuloligamentous structures is compromised. The stability of this joint is not only a matter of anatomical integrity but also of the biomechanical characteristics of joint contact, such as joint reaction force, area, and pressure, particularly in the presence of osseous defects. Understanding these biomechanical aspects is vital, as they directly influence the severity of instability and the effectiveness of therapeutic interventions. Despite the acknowledged importance of these factors, there remains a significant gap in the quantitative analysis of how varying sizes of anterior osseous defects affect those joint contact characteristics.

In the context of osseous defects on the anterior border of the glenoid, while the determination of a critical defect size that necessitates bone grafting has been a focal point of prior research, the broader implications of these defects on glenohumeral joint contact mechanics remain underexplored. Studies performed using cadaveric shoulders provided valuable insights into the critical sizes of osseous defects, ranging from 19% to 21% of the glenoid length, which require bone grafting to restore joint stability (ITOI *et al.*, 2000; YAMAMOTO, N. *et al.*, 2009, 2010). These investigations, utilizing methodologies with limitations such as non-physiological joint compressive forces, highlight the necessity for further research using physiological conditions to fully understand the biomechanical consequences of osseous defects. KLEMT *et al.* (2019) advanced this field by using a finite element (FE) model to assess critical defect sizes under physiological forces, suggesting a threshold for bone grafting at defects larger than 16% of the glenoid length. These studies, while focused on surgical thresholds, inadvertently underscore the gap in understanding the specific impact of varying defect sizes on joint contact mechanics.

Building upon the existing foundation, further research by YAMAMOTO, A. *et al.* (2014) on cadaveric shoulders has begun to bridge this gap by quantifying glenohumeral contact pressures in the presence of anterior labral and osseous defects. Under compressive forces of 220 N and 440 N, the study identified changes in contact area and peak pressures at abduction angles of 60° and 90° combined with neutral and external arm rotation, using Tekscan pressure sensors and a self-centering glenoid system. Despite the innovative approach, the limitations of the Tekscan sensors for non-linear surfaces and the non-physiological behavior of the self-centering glenoid mechanism point to the need for research methodologies that can more accurately replicate *in vivo* conditions.

Given the outlined limitations of existing methodologies and the need for a deeper understanding of glenohumeral joint mechanics in the presence of anterior osseous defects, **the general objective of this study is as follows:**

**A novel investigation of the impact of osseous defects of varying sizes (0 mm, 2 mm, 3 mm, 4 mm, 5 mm, and 6 mm) on the anterior border of the glenoid on glenohumeral joint stability and contact mechanics along shoulder abduction in the coronal plane with the arm externally rotated. Specifically, the following outcomes are analyzed:**

- Joint reaction force,
- Contact pressure,
- Contact area,
- Glenoid track width,
- Humeral head translations, and
- Muscle forces.

This objective is achieved using a computational model of the glenohumeral joint. The use of such models to answer clinical questions became a common practice to acquire quantitative information that cannot be obtained *in vivo* or *in vitro* due to ethical and technological limitations (ZHENG *et al.*, 2016). Over the years, many computational shoulder models were developed with the aim of enlightening several aspects of shoulder function related to activities of daily living (CHARLTON; JOHNSON, 2006; DAMSGAARD *et al.*, 2006; KLEMT *et al.*, 2018; NIKOOYAN, A. A. *et al.*, 2011), wheelchair propulsion (DUBOWSKY *et al.*, 2008), rotator cuff tear (KHANDARE; ARCE; VIDT, 2022; TERRIER *et al.*, 2007), osseous defects (KLEMT *et al.*, 2019; WALIA *et al.*, 2015), joint stability (FAVRE *et al.*, 2012; KLEMT *et al.*, 2017; QUENTAL *et al.*, 2016), humeral head translations (ENGELHARDT *et al.*, 2017; FAVRE *et al.*, 2012; SARSHARI *et al.*, 2017), shoulder arthroplasty (BOLA; SIMÕES; RAMOS, 2022; SINS *et al.*, 2015), joint contact (JUNIOR *et al.*, 2022; PÉCORA *et al.*, 2020; SAHARA *et al.*, 2019; SARSHARI *et al.*, 2017) and more. Many of these models are based on rigid body (RB) dynamics that simplify the articulations as spherical mechanical joints without translations. Despite their considerable usage in the analysis of diverse shoulder functions, they unfortunately fall short when the topic is joint contact mechanics and humeral head translations, significant aspects to correctly evaluate joint stability.

The inclusion of a deformable contact formulation into shoulder models permits the incorporation of humeral head translations along with the moment applied on the humerus due to the contact between the humeral head and the glenoid (SARSHARI *et al.*, 2017). The moment generated from the joint contact is called joint reaction moment and affects the prediction of joint stability based on the mechanical balance of the forces and moments acting on the glenohumeral joint. In this context, finite element models emerge as effectual tools to predict internal loading conditions that otherwise cannot be predicted *in-vivo, in-vitro* or from RB models. Furthermore, FE models permit the inclusion of biofidelic soft tissue geometries, such as the labrum and joint cartilages with ellipsoidal articular surfaces (ZUMSTEIN *et al.*, 2014a), along with the consideration of the joint's translational degrees of freedom (FAVRE *et al.*, 2012; SADEQI *et al.*, 2023; TERRIER *et al.*, 2007; ZHENG *et al.*, 2020).

Finite element models often simulate a sequence of static positions from specific joint movements. Some of these models are integrated with RB frameworks that can resolve the indeterminacy of the load sharing among the muscles, thereby generating stability in the position of interest. The loads and moments calculated in this manner are applied to the FE model to analyze the desired outcomes, such as contact mechanics and tissue stress. However, the loads and moments thus applied causes the humeral head to translate to a position that ensures mechanical equilibrium that is often different from the position firstly assumed in the RB model. This new position changes the original lines of action of the muscles, altering the previously calculated muscle forces and moments, and creates a new contact situation that changes the previously assumed joint reaction moment, in cases where this variable is included in the framework. No finite element model using joint kinematics as inputs to calculate the loads acting on the joint has yet considered the implications of these changes due to humeral head translations.

**An associated objective of this study is the development of a computational model of the shoulder that can assess joint stability and contact mechanics, including the influence of humeral head translations and joint reaction moment.**

The computational model consists of a rigid body model and a finite element model that work iteratively together. The RB model calculates the smallest muscle forces required to stabilize the glenohumeral joint, while the FE model imports these muscle forces to determine the position at which mechanical equilibrium is achieved. The new humeral head position and joint reaction moment obtained from the FE model are then fed back into the RB model for another iteration. This process continues until a stable convergent position is reached, defined as the humeral head position where the differences between the RB model and the FE model fall below a specific threshold. The model includes the humerus, scapula, humeral head cartilage, glenoid cartilage, deltoid muscle, and rotator cuff muscles. The articular surfaces of the cartilages are modeled as ellipsoidal and non-congruent and are represented using a deformable material model.

This work seeks to offer insights into the ways in which glenoid osseous defects influence glenohumeral joint mechanics, thereby laying a foundation for more effective diagnostic and therapeutic strategies. By addressing these critical questions, this research hopes to contribute to a deeper understanding of shoulder instability mechanisms, ultimately guiding clinical decision-making and improving patient outcomes.

## 1.2 STRUCTURE OF THE THESIS

The structure of this thesis is designed to provide a comprehensive exploration of the computational modeling of the glenohumeral joint, focusing on the analysis of contact mechanics in the presence of osseous defects. The thesis is organized into several chapters, each addressing key components of the research.

- Chapter 2 describes the shoulder physiology and its biomechanics, including a brief review about the glenohumeral joint stability, mobility, and the role of the muscles associated with this joint.
- Chapter 3 is a review of the state of art of shoulder models, presenting their development over the years and highlighting nowadays trends. It also includes brief discussions about the geometry and computational modeling of the GH joint cartilages and muscles, along with methods to solve the indeterminacy problem associated with the calculation of muscle forces.
- Chapter 4 details the development of the subject-specific computational model, describing the modeling of the considered structures in both CAD and FE softwares. It explains the proposed resolution to the load sharing problem and the iterative process between the rigid body model and the finite element model, emphasizing the novelty and technical aspects of the approach. This Chapter ends with the procedure to create the osseous defects in the anterior border of the glenoid.
- Chapter 5 reports the effects of the arm weight amplitude on joint reaction force and humeral head translations. It discusses the findings related to percentual increases in joint reaction force as a function of arm weight amplitude, the translation pattern in all cases studied, and the dispersion of humeral head translations along the abduction movement using the minimum bounding sphere technique.

- Chapter 6 presents the results of the simulations, focusing on the impact of various osseous defect sizes on joint stability and contact mechanics. It includes quantitative analyses and visualizations that illustrate the effects of osseous defect on joint reaction force, muscle forces, contact pressure, contact area, humeral head translation and glenoid track width.
- Chapter 7 discusses the findings of the simulations, comparing the results with existing studies. Some parts of the text have been extracted from a previous publication by the author (JUNIOR *et al.*, 2022) and revised to better adapt to the present study.
- Chapter 8 summarizes the conclusions drawn from the research, reiterating the significance of the findings and their contribution to the field of shoulder biomechanics. It also outlines potential future research directions to enhance the model's performance and applicability.

This doctoral thesis builds upon the author's master's dissertation, where the initial version of the model was developed. Significant improvements were made during the doctoral research, from which partial results have been published (JUNIOR *et al.*, 2022; PÉCORA *et al.*, 2020). Key updates to the model include:

- **Non-congruent and ellipsoidal articular surfaces** for both cartilages, providing a more accurate representation of joint contact geometry.
- **Consideration of the individual action of all muscle segments**, allowing for a more detailed analysis of muscle forces.
- **Inclusion of additional abduction angles** based on previously obtained positions, expanding the model's applicability.
- **Enhancement of the Simulation Framework**, specifically improving the coupling between the RB model and the FE model.
- **Improvement in resolving the load sharing problem**, utilizing MatLab optimization tools to achieve better performance and outcomes.
- **Refinement of muscle path tracing** for muscle segments in Abaqus/Explicit, ensuring the capability to **incorporate the effects of humeral head translations** on muscular lines of action, capturing more realistic joint dynamics.

# 2 THE HUMAN SHOULDER

## 2.1 SHOULDER PHYSIOLOGY AND BIOMECHANICS

### 2.1.1 Shoulder mobility and stability

The shoulder complex is composed by the humerus, the scapula, the clavicle and three joints that provide to the shoulder the greatest mobility of the human body (JOBE; PHIPATANAKUL; COEN, 2009). The sternoclavicular joint connects the thorax to the clavicle and the acromioclavicular joint connects the clavicle to the scapula. These joints, in combination with the junction between the anterior surface of the scapula and the thoracic cage, are collectively known as the scapulothoracic joint[1] (INMAN; SAUNDERS; ABBOTT, 1944). It enables and integrates the movement of the upper limb with the torso. The glenohumeral joint, also known as the shoulder joint, is a synovial joint (Figure 1). It is responsible for roughly two thirds of the shoulder total mobility, that covers about 65% of a sphere (ENGIN; CHEN, 1986). This great range of motion is only possible because the articular surface of the glenoid is considerably smaller than the articular surface of the humeral head. While the humeral head constitutes approximately one third of the surface of a sphere, the glenoid surface is pear shaped and covers roughly only one quarter to one third of the humeral head surface (ITOI; MORREY; AN, 2009).

Figure 1 – Glenohumeral joint, comprising the humerus, the scapula, and the clavicle. The articular surfaces of the humeral head and of the glenoid fossa are represented in green.

From Kenhub[2].

[1] Some authors consider the junction between the anterior surface of the scapula and the thoracic cage as the fourth joint, as exemplified by Hall (2012). Here, the definition by Inman (1944) is used.
[2] Available at <https://www.kenhub.com/en/library/anatomy/the-shoulder-joint>. 14 October 2024.

The relationship between the contribution of the glenohumeral joint and the scapulothoracic joint to shoulder mobility is called scapulohumeral rhythm (Figure 2). It is said that the overall ratio to glenohumeral-to-scapulothoracic motion is 2:1 during arm elevation (BERGMANN, 1987). However, this ratio is not linear throughout the movement. At the first 30 degrees of abduction the glenohumeral motion prevails over the scapulothoracic, where the scapulohumeral rhythm may vary from 4:1 (POPPEN; WALKER, 1976) to 7:1 (DOODY; FREEDMAN; WATERLAND, 1970).

Figure 2 – Scapulohumeral rhythm. The top image shows the arm at 30° abduction, where most of the movement occurs at the glenohumeral joint. The image below shows the arm is 90° abduction with a scapulohumeral rhythm ratio of 2:1.

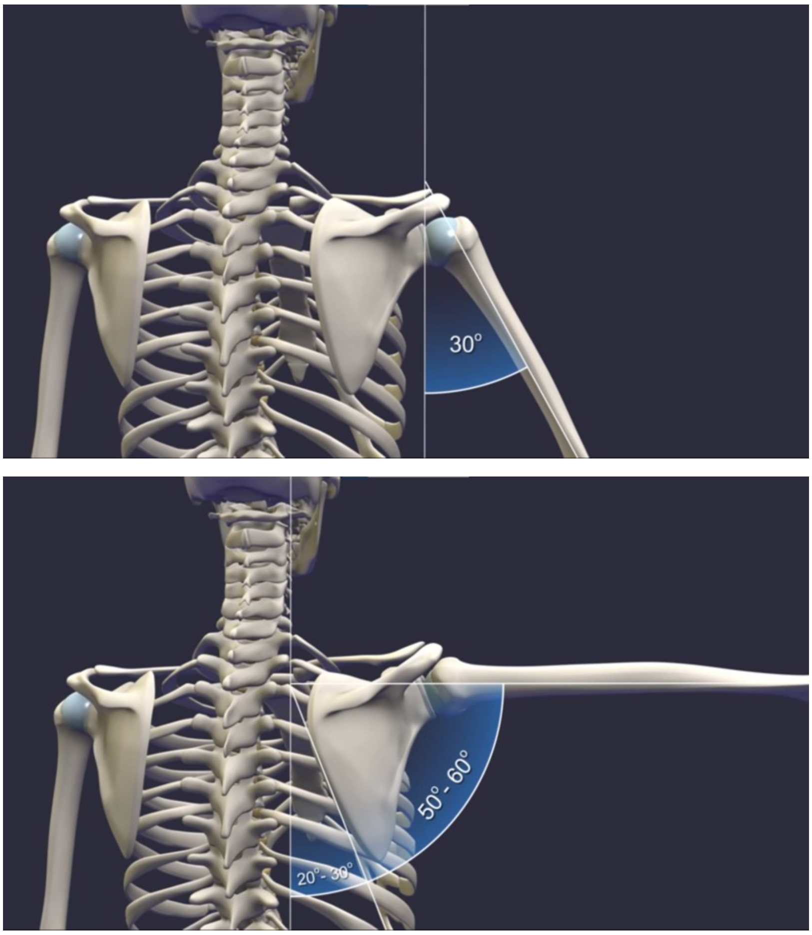


Compilation by the author[3].

[3] Images obtained from <https://www.youtube.com/watch?v=rpzBGlOEW4E>. 14 October 2024.

The same glenohumeral joint that gives the shoulder its great mobility is, however, inherently unstable. The articular surface of the glenoid is too shallow and the contact area between the bones is not big enough to sustain the loads on the joint. There are several stabilization mechanisms that take place depending on whether the arm is in mid-range or end-range of motion (ITOI; MORREY and AN, 2009). End-range of motion happens at the limits of a shoulder movement, *e.g.*, at high degrees of abduction with external rotation of the arm. The capsuloligamentous structures are then tight and provide most of the joint stability, preventing the translations of the humeral head. Outside the end-range of motion, the arm is in mid-range of motion. The capsuloligamentous structures are lax and stability is ensured by mechanisms such as intra-articular pressure and the concavity-compression effect. The intra-articular pressure acts as a stabilizing mechanism when the shoulder muscles are silent (*e.g.*, arm in hanging position), sucking the humeral head into the glenoid socket and preventing a downward translation. The concavity-compression effect occurs by contraction of the muscles around the joint, compressing the humeral head into the glenoid fossa. The deeper the glenoid socket, the greater the concavity-compression effect.

### 2.1.2 The glenoid labrum and the capsuloligamentous structures

The glenohumeral joint is surrounded by a loose fibrous capsule on all sides (Figure 3). It is overall lax and does not offer much resistance to movement. The joint capsule arises from the scapular neck on its anterior and inferior sides, and blends with the glenoid labrum on its posterior and superior sides. Except on specific places, it is reinforced by the tendons of the rotator cuff muscles and, on its anterior side, by the glenohumeral ligaments.

Figure 3 – Glenohumeral articular capsule and coracohumeral ligament.

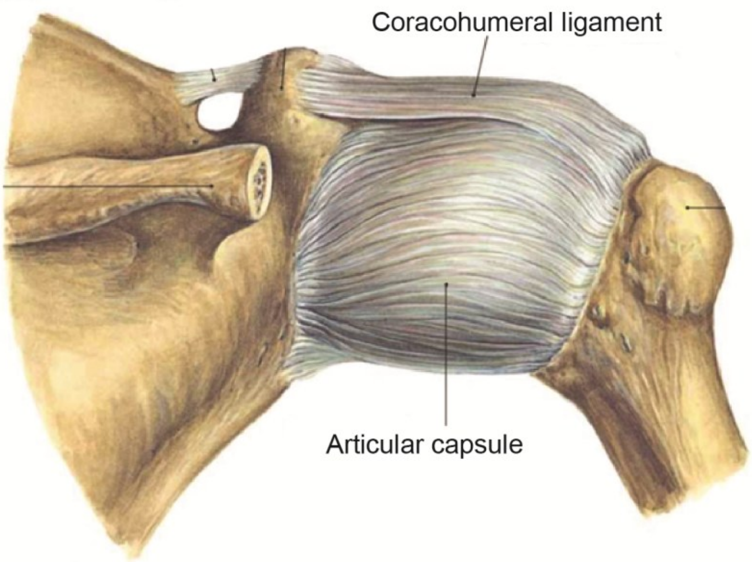


Adapted from PAULSEN & WASCHKE (2013).

The glenoid labrum is a fibrocartilaginous structure attached to the glenoid rim (Figure 4). It assists the joint mid-range stability by conferring depth and concavity to the glenoid fossa, resisting the translations of the humeral head (ZHENG *et al.*, 2016). It also serves as an anchor to the glenohumeral ligaments and the biceps brachii tendon (BELTRAN *et al.*, 2002).

The coracohumeral ligament has as its origin the coracoid process at the scapula and attaches to the greater and lesser tuberosities of the humerus. From its origin, it extends itself as two bands over the top of the shoulder to blend with the capsule near its insertion on the humerus. When the arm is externally rotated, it becomes taut and functions as a possible inferior joint stabilizer (ITOI; MORREY; AN, 2009).

Figure 4 – Glenoid labrum and surrounding structures.

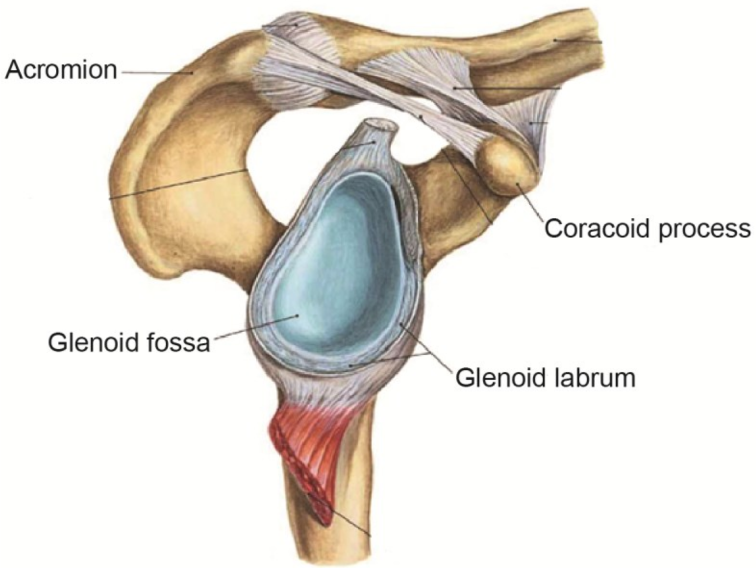


Adapted from PAULSEN & WASCHKE (2013).

According to BELTRAN *et al.* (2002, p. 253), “the glenohumeral ligaments are infoldings of the glenohumeral capsule, extending from the anterior and inferior glenoid margin of the glenoid to the region of the anatomical neck of the humerus”, as illustrated in Figure 5. There are the superior glenohumeral ligament, the middle glenohumeral ligament and the inferior glenohumeral ligament. Their anatomy may vary between individuals and their function is debatable, as it is dependent on the position of the humerus relative to the glenoid. The superior glenohumeral ligament originates “from the tubercle of the glenoid anterior to the origin of the long biceps tendon and runs inferior and lateral to insert on the head of the humerus near the proximal tip of the lesser tuberosity” (ITOI; MORREY; AN, 2009, p. 239). Its function is similar to the coracohumeral ligament, acting on inferior stability and limiting external rotation of the arm (BURKART; DEBSKI, 2002).

The anatomy of the middle glenohumeral ligament is akin to the superior glenohumeral ligament. According to (STEINBECK; LILJENQVIST; JEROSCH, 1998), its origin is found on the supraglenoid tubercle and anterosuperior region of the labrum between the 1 and 3 o’clock positions, blending with the subscapularis tendon and attaching at the lesser tuberosity of the humerus. TURKEL *et al.* (1981) observed that when the shoulder is abducted and externally rotated, the middle glenohumeral ligament becomes taut, and hence it is considered as an anterior stabilizer. As stated by PASSANANTE *et al.* (2017, p. 65), the inferior glenohumeral ligament complex is "a hammock-like structure with anchor points on the anterior and posterior glenoid and an attachment to the proximal humeral neck near the head/neck junction". It encompasses the anterior band, the posterior band and the axillary pouch. The anterior band is attached partly on the bony glenoid and partly on the anterior labrum, restraining anterior and inferior translations of the humerus when the arm is abducted and externally rotated. The posterior band has its origin at the posterior glenoid rim and helps with posterior stability when the arm is in flexion and internally rotated (WARNER *et al.*, 1992). The axillary pouch is the "hammock" between the anterior and posterior bands and has its origin at the inferior glenoid labrum. The inferior glenohumeral ligament is inserted at the inferior margin of the humeral articular surface and around the anatomic neck of the humerus.

Figure 5 – Illustration of the glenohumeral ligaments.

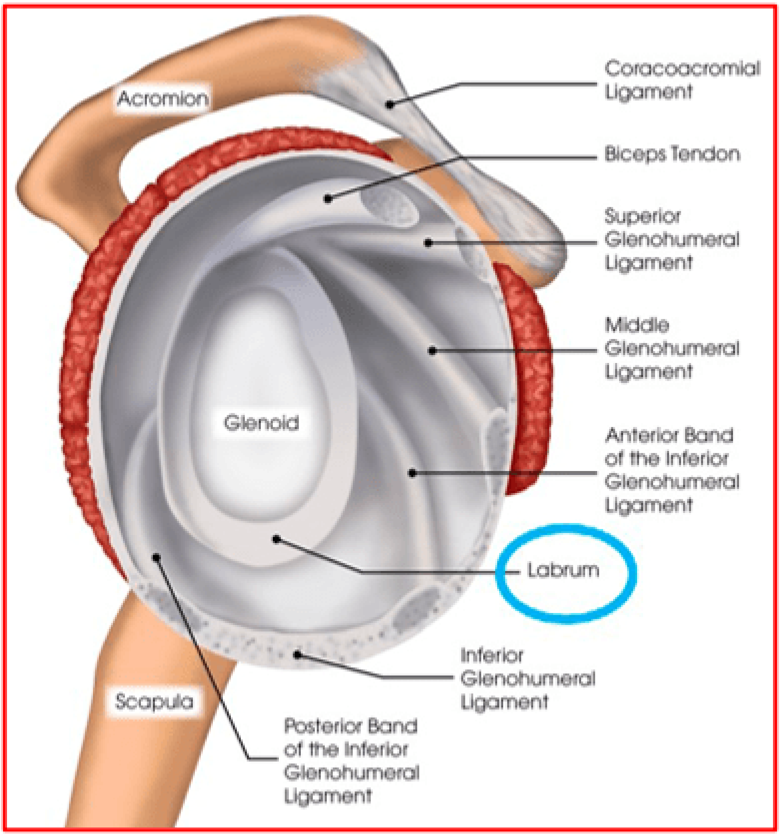


From Dr. Anand Jadhav[4].

[4] Available at <https://dranandjadhav.in/shoulder-instability-dislocations/>. 14 October 2014.

### 2.1.3 Glenohumeral joint muscles

Most voluntarily controlled skeletal muscles have the function of producing movements of body parts (TORTORA; DERRYCKSON, 2011). By contracting, a muscle produces tension that is transferred to its tendons and to the bones attached to them, creating a torque at the joint and pulling the bones together when the contraction is concentric. The function of a muscle depends on the movement in execution and on the joint angle. It can be an agonist, contracting to produce movement, or an antagonist, acting against the movement (HALL, 2012). However, a muscle generally acts in tandem with other muscles so that the joint motion can be executed in a controlled manner. The election of which muscle must be activated comes from the central nervous system, but the choosing criteria is not yet completely understood.

There are eleven muscles around the glenohumeral joint that act together to move and to stabilize it. The deltoid and the rotator cuff muscles are the primary mover and stabilizers, respectively, during the abduction movement. The supraspinatus, subscapularis, infraspinatus and teres minor are collectively known as rotator cuff muscles (Figure 6). Their tendons merge with the joint capsule (and sometimes with one another), creating a cuff around the joint, surrounding it posteriorly, superiorly and anteriorly (HALL, 2012). The main function of these muscles is to stabilize the joint, compressing the humeral head into the glenoid fossa to prevent excessive translations, while also acting as important rotators of the arm.

Figure 6 – Rotator cuff muscles. On the left a posterior view of the scapula depicting the subscapularis and the posterior part of the supraspinatus. On the right an anterior view of the scapular depicting the infraspinatus, teres minor and the anterior part of the supraspinatus.

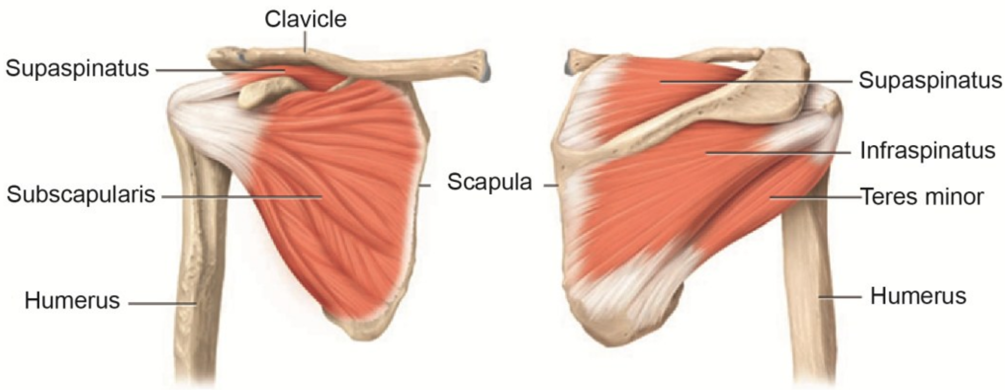


Adapted from TORTORA & DERRYCKSON (2011).

The supraspinatus fossa is located above the spine of the scapula, and it is the origin site of the supraspinatus muscle. This muscle's tendon inserts on the greater tuberosity of the humerus in common with the coracohumeral ligament anteriorly and with the infraspinatus posteriorly (JOBE; PHIPATANAKUL; COEN, 2009). It aids the deltoid in the abduction of the arm, mainly at the beginning of the movement, and is an important inferior stabilizer. The subscapularis muscle originates at the subscapular fossa on the anterior surface of the scapula and inserts onto the lesser tubercle of the humerus. It represents 53% of the muscle mass of the rotator cuff muscles (KEATING *et al.*, 1993) and is the main internal rotator of the arm. By releasing the subscapularis tendon on cadaveric specimens, MARQUARDT *et al.* (2006) found that it also helps with anterior-inferior stabilization of the humeral head in mid-range of motion, and it is considered the most important anterior stabilizer by DEPALMA; COOKE; PRABHAKAR (1967).

Figure 7 – Illustration of the deltoid muscle in a side view. In blue, the posterior deltoid; in green, the middle deltoid; and in red the anterior deltoid.

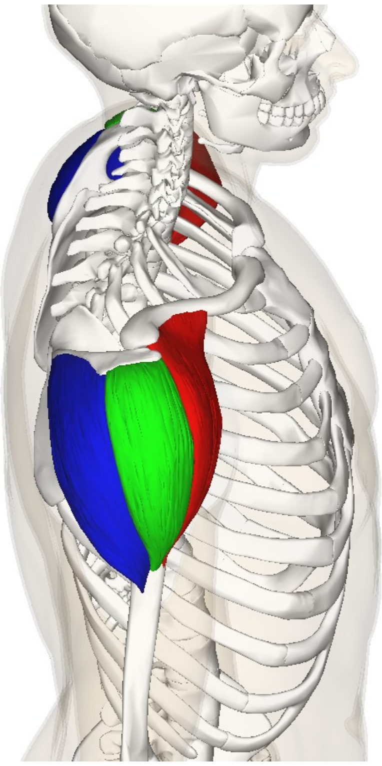

From Wikipedia[5].

The infraspinatus muscle has a wide origin at the posterior surface of the scapula and inserts on the grater tubercle of the humeral head, blending with the supraspinatus tendon superiorly and with the teres minor tendon inferiorly (BACLE *et al.*, 2017). The infraspinatus and the teres minor act synergistically as external rotators of the arm. The deltoid has a U-shaped origin that comprises the spine of the scapula, the acromion and the lateral end of the clavicle, all of them sharing the same insertion at the deltoid tuberosity on the shaft of the humerus (Figure 7). It is generally divided into three functionally distinct parts in accordance with its origin: the anterior (clavicular) deltoid, the middle (acromial) deltoid, and the posterior (spinal) deltoid (MOSER *et al.*, 2013). The middle deltoid is the main abductor of the arm and an elevator of the humeral head (ITOI; MORREY; AN, 2009). The anterior deltoid helps with arm flexion and internal rotation of the humerus, while the posterior deltoid helps with external rotation.

[5] Available at <https://en.wikipedia.org/wiki/Deltoid_muscle>. 14 October 2024.

The biceps brachii is a bi-articular muscle, crossing the joints at the elbow and shoulder (Figure 8). It consists of a large head and a short head that merge into a common belly. The large head originates from the supraglenoid tubercle of the glenoid fossa and merges with the glenoid labrum superiorly. Its tendon passes through the bicipital groove of the humerus, encircling the glenohumeral joint. The short head originates from the coracoid process of the scapula. The muscle belly has two tendinous insertions at the forearm. The biceps brachii works primarily at the elbow joint as a flexor and is a powerful supinator of the forearm (LANDIN; THOMPSON; JACKSON, 2017). Its role as a stabilizer of the humeral head is debatable. Some studies on cadavers verified that, when a load was applied at the long head of the biceps, its tendon acted as compressor of the humeral head into de glenoid fossa (PAGNANI *et al.*, 1996; YOUM *et al.*, 2009). RODOSKY; HARNER; FU (1994) verified the role of the biceps on resisting torsional forces during the throwing movement of baseball players; and an old study suggests that it acts as a depressor of the humeral head when electrically stimulated (ANDREWS; CARSON; MCLEOD, 1985). However, two studies measured the muscle activity in isolated shoulder movements with controlled elbow and shoulder joints angles. In a series of movements that include flexion abduction, internal and external rotation, LEVY *et al*. (2001) found that the only substantial activity of the biceps brachii occurred at the first 30° of flexion by electromyography (EMG) measurements. LANDIN *et al*. (2008) analyzed the isometric torque produced by the shoulder in the scapular plane when the muscle was electrically stimulated in a variety of combined shoulder and elbow angles. They found a peak torque at 0° abduction, that became insignificant after 30°, but not substantial enough to say that the long head of the biceps played a major role in stabilizing the humeral head. Both studies support the statement from JOBE *et al*. (2009) that the action of the biceps brachii on shoulder stability is unusual on patients without shoulder pathologies.

Figure 8 – Illustration of the biceps brachii in green. The long head passes through the bicipital groove and short head originates from the coracoid process of the scapula.

From Kenhub[6].

The other muscles that cross the glenohumeral joint do not act significantly on the abduction of the arm. The teres major helps with internal rotation, adduction and extension of the arm when there is some form of resistance. The coracobrachialis acts on the adduction and flexion of the glenohumeral joint. The latissimus dorsi functions as an internal rotator and adductor of the arm and the function of the pectoralis major depends on the joint start position, but it is not related to the abduction movement. While the triceps brachii is thought to help in shoulder adduction against resistance, it acts mainly as an elbow extensor. Figure 9 illustrates these muscles from origin to insertion.

[6] Available at <https://www.kenhub.com/pt/library/anatomia/musculo-bicipite-braquial>. 14 October 2024.

Figure 9 – Illustrations of the pectoralis major (sternal and clavicular portions), latissimus dorsi, teres major, coracobrachialis and triceps brachii.

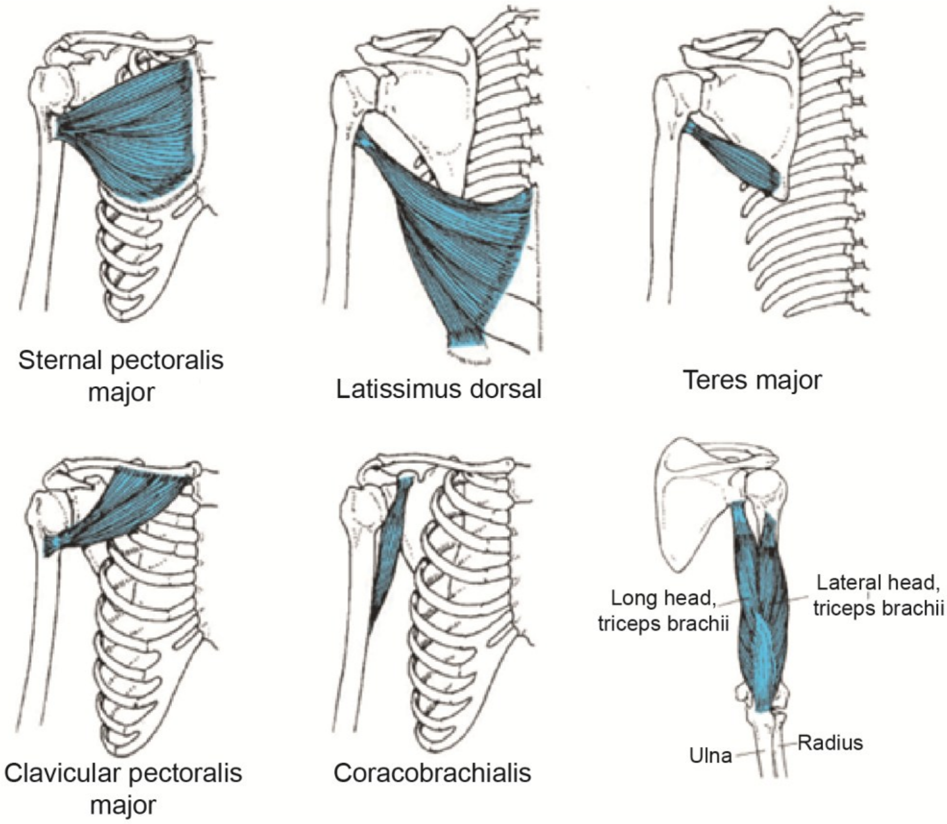


Adapted from HALL (2012).

## 2.2 SHOULDER PATHOLOGIES AND THE GLENOID TRACK

Anterior shoulder instability is a common affliction of the shoulder due to the anatomy of the glenohumeral joint. Severe cases of instability can lead to dislocations, *i.e.*, the loss of articular contact. The glenohumeral joint is the joint that presents the most cases of dislocations (CUTTS; PREMPEH; DREW, 2009). ZACCHILLI & OWENS (2010) carried out an analysis of shoulder dislocation incidence in the USA from 2002 to 2006 and found an incidence rate of 23,9 per 100000 person-years. Similarly, an incidence rate of 40,4 per 100000 person-years in men was found in the UK between 1995 and 2015 (SHAH *et al.*, 2017). In Oslo, 2009, there was an incidence rate of 56,3 per 100000 person-years (LIAVAAG *et al.*, 2011). In all studies, the highest risk of dislocation is associated with young men below 30 years of age.

The biomechanical reasons for the occurrence of dislocations are associated with tangential forces acting on the articular surfaces that surpass the stabilization capability of the joint stabilizers (ZHENG *et al.*, 2016). The occurrence of dislocation may cause structural damage to bones and soft tissues, such as a Bankart lesion, a bony Bankart lesion, and a Hill-Sachs lesion. The Bankart lesion is the detachment of the anteroinferior labral complex, and it increases the risk of further dislocations (Figure 10). The Hill-Sachs lesion (HSL) is a posterolateral humeral head compression fracture that results from impacts with the anterior glenoid rim (Figure 11). The bony Bankart is a fracture to the anteroinferior glenoid rim that reduces the articular contact area of the glenoid (Figure 12). Arthroscopic Bankart Repair (ABR) is the most common procedure to recover the shoulder anterior stability (DEFRODA *et al.*, 2017) by reattaching the capsule-labral complex. However, the presence of a HSL is a risk factor that may lead to further dislocations and to the failure of the ABR. ITOI (2017) says that the risk of a HSL causing instability is zero if it is covered by the glenoid, but the risk of recurrent dislocation is high if it is out of glenoid coverage because it may engage with the anterior rim of the glenoid. The risk intensifies when both an HSL and a bony Bankart coexist, termed bipolar bone loss (DI GIACOMO; ITOI; BURKHART, 2014), affecting approximately 80% of patients with anterior instability (ITOI, 2017).

Figure 10 – Illustration of a Bankart lesion.

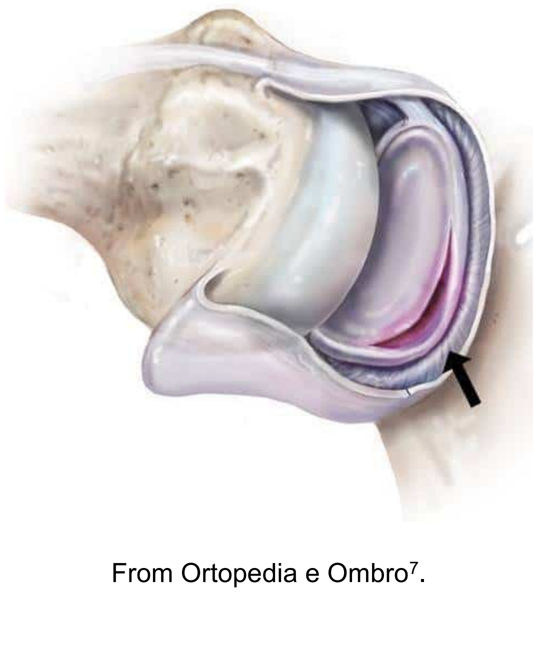

From Ortopedia e Ombro[7].

[7] Available at < https://ortopediaeombro.com.br/lesao-de-hill-sachs-e-lesao-de-bankart-lesao-do-labio-anterior/>. 14 October 2024.

Figure 11 – Illustration of a Hill-Sachs lesion.

From Central Coast Orthopedic[8].

Figure 12 – Bony Bankart. $\boldsymbol{D}$ represents the glenoid width and $\boldsymbol{d}$ the size of the bony defect.

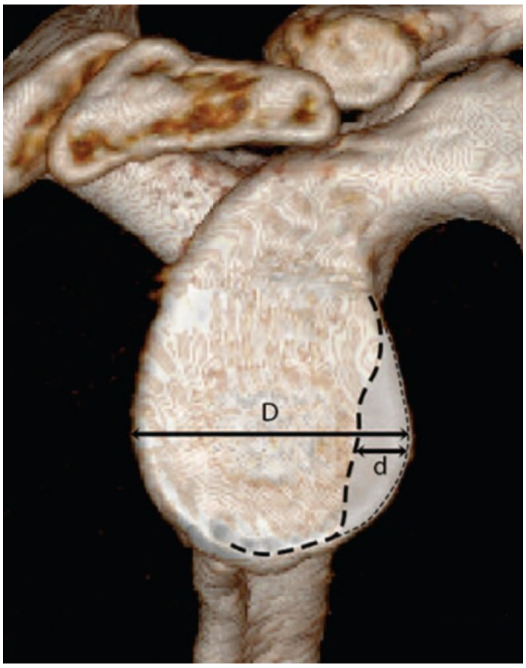


Adapted from STEFANIAK *et al*. (2020).

[8] Available at < https://centralcoastortho.com/patient-education/hill-sachs-lesion/>. 14 October 2024.

According to DI GIACOMO; ITOI; BURKHART (2014, p. 90), “there are no clear guidelines on how to address patients with bipolar bone lesions who have varying degrees of bone loss of the glenoid as well as the proximal humerus (Hill-Sachs defects)”. They discuss some methods to assess the risk factors related to bone losses that may lead to further instability of the shoulder, before or after an ABR. Many of them, however, rely mostly on qualitative data and are related to arbitrary sizes of bone losses. To improve decision making processes on how to treat shoulder instability, to avoid unnecessary surgeries, and to reduce the occurrence of recuring dislocations, quantitative data are paramount. To this end, DI GIACOMO; ITOI; BURKHART (2014) conceived the concepts of *on-track* and *off-track* HSL based on the position of the HSL in relation to the glenoid track.

The concept of the glenoid track was proposed by YAMAMOTO *et al*. (2007) for a better understanding of the interaction between anterior glenoid osseous defects and the humeral head. According to ITOI (2017, p. 349), “the glenoid track is the area of posterior humeral articular surface in contact with the glenoid when the arm moves along the posterior end-range of movement” (Figure 13). Posterior end-range movement occurs when the arm is in abduction and external rotation, causing the anteroinferior capsule to tighten and preventing humeral head translation.

Figure 13 – Representation of the glenoid track by overlapping the glenoid fossa contour on the surface of the humeral head.

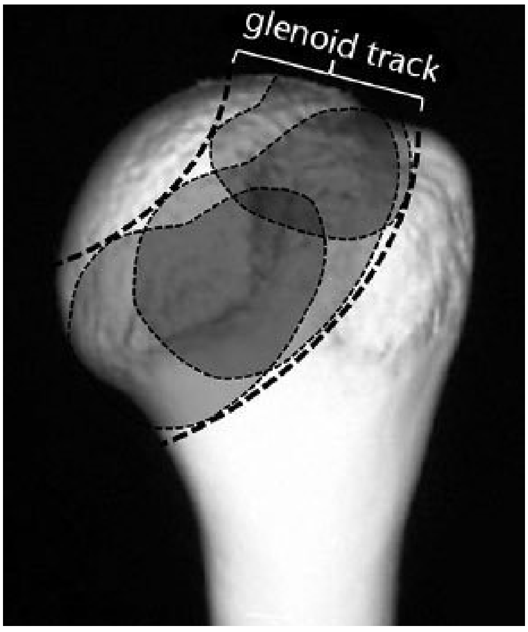


From ITOI (2017).

In contrast to other assessment methods, the glenoid track concept dictates that the most important factor is not the HSL size or depth, but rather its location. When the Hill-Sachs lesion stays within the glenoid track, there is no inherent risk of it causing a dislocation, and it is termed *on-track* HSL. However, if the medial margin of the HSL extends beyond the glenoid track, it is referred to as *off-track*, and it has the potential to override the glenoid rim, leading to a dislocation. The study conducted by YANG *et al*. (2018) found that the recurrence rate in patients with off-track lesions was significantly higher (69,2%) than in patients with on-track lesions (8,8%).

Figure 14 – Hill-Sachs lesion (a) *on track* and (b) *off-track*.

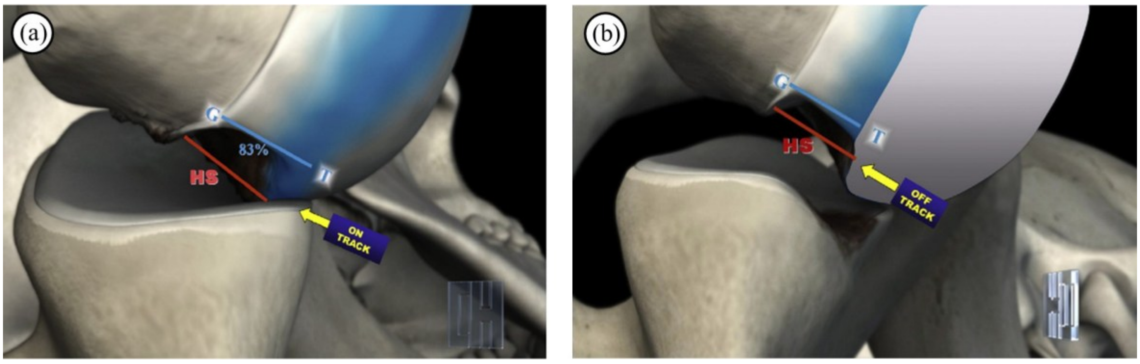


Adapted from *DI GIACOMO et al*. (2014).

Figure 15 – Measurement of the Hill-Sachs interval (HIS) as the sum of the Hill-Sachs width (HS) and the bone bridge (BB). Dotted line L1 represents que medial margin of the rotator cuff attachments and dotted line L2 represents que medial margin of the glenoid track.

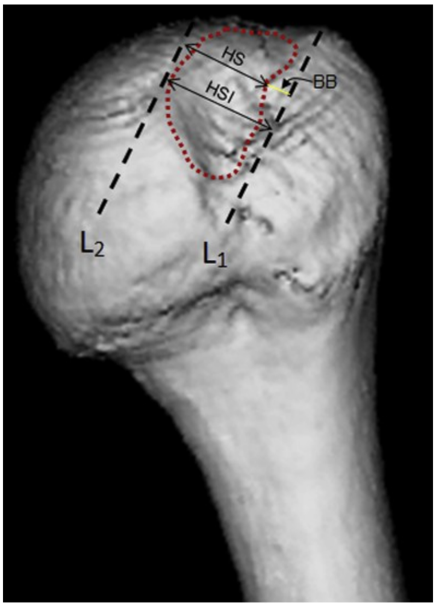


From DI GIACOMO *et al.*, 2016.

The aforementioned concepts allow the use of quantitative data to assess the risks of recurring dislocations by comparing the values between the Hill-Sachs interval (HSI) and the glenoid track width. The Hill-Sachs interval is quantitatively determined by the sum of the width of the Hill-Sachs lesion and the width of the bone bridge, specifically defined as the area of exposed bone that lies between the Hill-Sachs lesion and the medial footprint of the rotator cuff, as illustrated in Figure 15.

The *in vivo* measurement of glenoid track width, as described by OMORI *et al.*, 2014, begins with the acquisition of joint images from MRI scans, from which a three-dimensional model of the joint is constructed. Within this 3D model, a plane is created to approximate the anatomical neck of the humerus, creating a section with a central reference point called Point G. From Point G, a line is drawn perpendicular to this plane until it intersects with the articular surface of the humeral head, defining Point C at the intersection. This entire procedure is illustrated in detail in Figure 16.

Figure 16 – In red, the plane approximating the humeral neck of the humerus (A). The section created by the plane and the center of this section, called point G (B). The perpendicular line connecting point G to the articular surface, thus defining the location of point C (C).

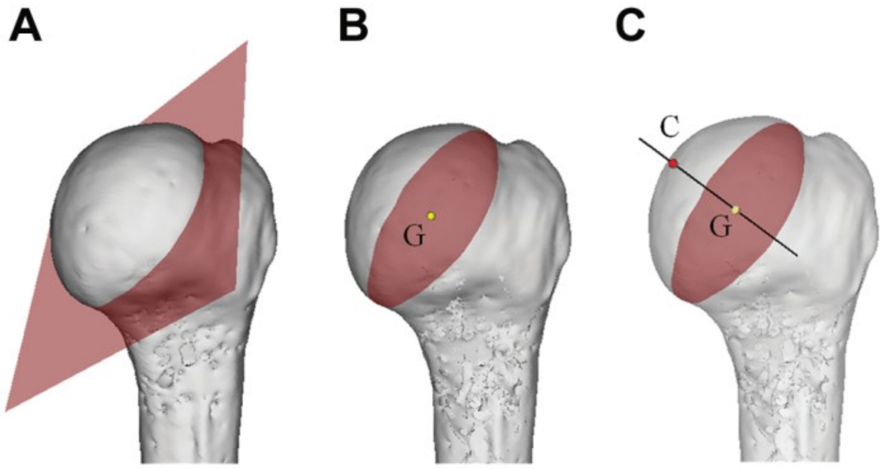


From OMORI *et al.*, 2014.

From an *en face* view of the glenoid, a vertical line is created connecting the 12 o’clock and 6 o’clock positions (Figure 17). Subsequently, a horizontal line is drawn through the midpoint of this vertical line. At the point where this horizontal line intersects with the anterior rim of the glenoid, Point M is identified. During shoulder abduction, Point M is projected onto the humeral head. At static abduction angles of interest, a line is traced onto the humeral head starting from Point C, passing through the projected Point M, and extending to the rotator cuff tendon's footprint on the greater tuberosity. The width of the glenoid track at each abduction angle is then measured as the distance from the projected Point M to the medial margin of the footprint of the rotator cuff. A cadaveric study has shown that the glenoid track width corresponds to $84\% \pm 14\%$ of the glenoid width (YAMAMOTO, N. *et al.*, 2007), while OMORI *et al*. (2014) found a corresponding value of $83\% \pm 12\%$. By comparing the values of the glenoid width and the HSI, the Hill-Sachs lesion can be defined as *on-track* if the glenoid track width is greater than the HSI or *off-track* if the glenoid track width is smaller than the HSI.

Figure 17 – Definitions of points L and M (A). Projection of the glenoid area onto the humeral head surface along with point M (B). Measurement of the glenoid track width (C).

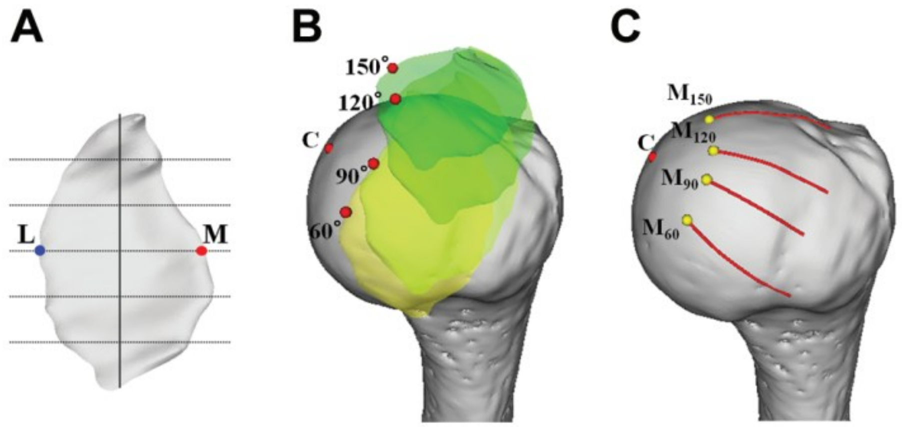


From OMORI *et al.*, 2014.

# 3 STATE OF ART

The understanding of the functions of the individual structures of the shoulder and how they cooperate with each other is paramount to develop better treatment techniques, better strategies to avoid the occurrence of damage to the tissues and even to design joint implants. However, there are many essential parameters that cannot be readily measurable due to ethical and technological limits (ZHENG *et al.*, 2016). Some procedures may be too invasive to perform (*e.g.*, muscle force measurement) (ERDEMIR *et al.*, 2007) or the devices may lack enough resolution to give correct measurements (*e.g.*, humeral head translations) (BOLSTERLEE; VEEGER; CHADWICK, 2013). In this context, computational shoulder models emerge as effectual tools that allow the investigation of aspects that are otherwise difficult or impossible to quantify.

The model to be used and its complexity is determined heavily by the desired output and should be realistic enough to replicate the behavior of the human musculoskeletal system (NIKOOYAN, A. A. *et al.*, 2011). It is possible to roughly classify musculoskeletal models into two major categories: multibody models and finite element models (ZHENG *et al.*, 2016). Multibody models are based on rigid body dynamics and can simulate the kinetics of a predefined movement. The skeletal description of multibody models is quite similar to each other. The bones are considered as rigid bodies, articulations are simplified as mechanical joints without translations and muscles are modeled as taut string connecting their insertions, tracing a path that wraps over bones and virtual soft tissues in the way. These types of models have low computational costs, allowing the consideration of not only the shoulder complex, but also its adjacent bones and the interactions between them. The resolution of the load-sharing problem is performed mainly by optimization procedures associated with inverse and/or forward dynamics methods. Traditionally, multibody models rely intrinsically on simplifications of the joint as congruent spherical surfaces without any contact model to simulate humeral head translations. Recent models, however, have managed to include elastic (KHANDARE and VIDT, 2022) and viscoelastic (SARSHARI *et al.*, 2017) contact models using contact meshes on the humeral head and glenoid fossa to simulate a more biofidelic joint contact, thus allowing some degree of humeral head translations.

Despite the evolution of multibody models, they are still not capable of providing a detailed assessment of the deformable and non-congruent joint contact like those provided by finite element models. Furthermore, FE models enable the inclusion of 3D geometries of soft tissues such as the musculotendon units of the rotator cuff, the glenohumeral ligaments and the glenoid labrum, thus permitting the assessment of several clinical related issues, among which:

- Effect of rotator cuff deficiency on the glenohumeral contact and joint stability (TERRIER *et al.*, 2007; ZHENG *et al.*, 2020);
- Influence of bone defects in the glenoid fossa and humeral head on joint stability (KLEMT *et al.*, 2019; WALIA *et al.*, 2015);
- Evaluation of the contact geometry and pressure distribution along the glenoid track (JUNIOR *et al.*, 2022); and
- Prediction of prosthesis performance (BOLA; SIMÕES; RAMOS, 2022).

This review aims to present and discuss many aspects of the development of shoulder models, beginning by tracing their evolution over the years and highlighting some important aspects and their uses in the **Development of Shoulder Models** section. In the **Modeling of Soft Tissues** section, the representation of muscles, cartilages, glenoid labrum, their material properties, and the interaction among them are discussed. The section **Muscle Force and the Load Sharing Problem** focuses on the several methods tailored to estimate the forces the muscles should exert to perform a certain movement. The last section, **Analysis of Glenoid Osseous Defects**, discuss the studies related to the effects of osseous defects on joint stability.

## 3.1 DEVELOPMENT OF SHOULDER MODELS

The development of shoulder models started at the very end of the 19$^{th}$ century with a physical model of the shoulder mechanism, where the muscles were represented by strings connected to a keyboard (Figure 18) and motions took place when the keys were pressed (VAN DER HELM, 1994a). Many decades later, two-dimensional models arose with the works of DELUCA and FORREST (1973), and POPPEN and WALKER (1978). These models described the motion of the humerus with respect to a nonmoving scapula. Although an advancement at the time, 2D representations were not enough to describe the complexities of the joint.

Three-dimensional musculoskeletal models of the human shoulder appeared at the end of the last century. KARLSSON and PETERSON (1992) introduced a shoulder model that was used to analyze static load sharing between the muscles, bones, and ligaments during the abduction movement on the scapular plane every 15º, up to 120º. According to them, earlier attempts on the development of shoulder models did not consider important aspects, such as the addition of all the muscles of the shoulder, not only the main ones. Being one of the first 3D models developed, some limitations could be observed, such as the issue of the glenohumeral joint stability and the lack of detailed data to better comprehend and reproduce the model.

Figure 18 – Physical shoulder mechanism.

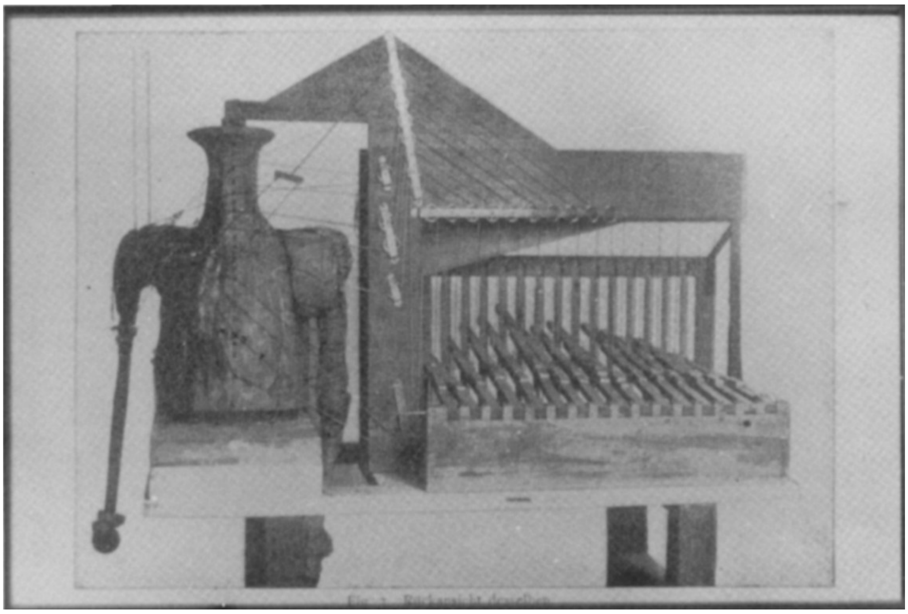

From van der Helm (1994).

In 1994, van der Helm published his work on the development of a finite element shoulder model that made notable contributions on shoulder model development throughout the years (VAN DER HELM, 1994a). Initially known as the Delft Shoulder Model (DSM), it consisted of the shoulder girdle, the humerus, three extracapsular ligaments, and 16 muscles divided into 95 muscle segments. The shoulder structures were derived from cadaver data and were represented as structural elements (Figure 19) on SPACAR, a software subroutine package for simulation of the behavior of biomechanical systems. The model itself consisted of motion equations describing the mechanical behavior of the shoulder mechanism, derived by using the finite element method. Recorded motions of the bones and external loads were used as inputs to find muscle and contact forces, muscle length and moment arms. Contributions were made on subsequent years to update the model, such as the use of a new morphological dataset (BRETELER; SPOOR; VAN DER HELM, 1999). Aspects and developments of this model since 1994 were described by NIKOOYAN, *et al.*, (2011) such as the addition of muscle dynamics data, new simulation frameworks combining inverse with forward dynamics optimization, and a new muscle load sharing cost function based on the energy consuming processes needed for a muscle to contract (PRAAGMAN *et al.*, 2006). With the addition of elbow data, this model is known as the Delft Shoulder and Elbow Model (DSEM). It was used to study goal-directed movements (HAPPEE; VAN DER HELM, 1995), wheelchair propulsion (VEEGER; ROZENDAAL; VAN DER HELM, 2002), and rotator cuff tears (STEENBRINK *et al.*, 2009).

Figure 19 – Shoulder model developed by van der Helm (1994).

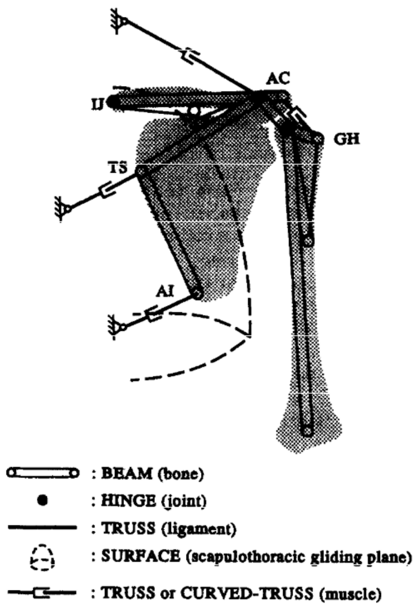


From van der Helm (1994).

The studies published by Brian A. Garner & Marcus G. Pandy on the years 1999-2001 influenced many studies in the area (GARNER; PANDY, 1999, 2000, 2001). They presented their model with data detailed enough that anyone could reconstruct a mathematical model using it. The musculoskeletal model included all the major joints of the shoulder, elbow and wrist. Up to that date, no other model had a musculoskeletal geometry so complete as this one. To develop such a model, they used data from the Visible Human Project, a public-domain library of clinical digital images of one male cadaver and one female cadaver with which it is possible to reconstruct musculoskeletal models[9]. They also introduced the concept of the obstacle-set method to correctly model the paths of muscles and their wrapping around bones and soft tissues.

Holzbaur and colleagues developed a musculoskeletal model of the upper limb including muscles and joints from the shoulder to the fingertip known as the Stanford Model (HOLZBAUR; MURRAY; DELP, 2005). It focuses on the relationship between joints on muscle force generation and its parameters were experimentally derived. In 2006, I. W. Charlton and G. R. Johnson published a musculoskeletal model of the upper limb named the Newcastle Model to study the muscle, ligaments and joint contact forces during the execution of ten activities of the daily living (CHARLTON; JOHNSON, 2006). Its geometry (Figure 20) was based on the cadaver studies made by JOHNSON *et al.* (1996), and by the DSEM. To simulate the geometry, the software SIMM was used, but the algorithm was implemented using Matlab. This model brought a novel approach to simulate the ligaments tensile properties.

Michael Damsgaard and co-authors published in 2006 a paper describing the Anybody Model, a musculoskeletal model of the entire human being (DAMSGAARD *et al.*, 2006). The model development started at the Aalborg University by the authors as a general modeling system to reproduce several activities of the daily living in a relatively easy way. In 2001 the AnyBody Modeling System was turned into a private company, the AnyBody Technology. Their model of the upper limb was based on the data published by the DSEM with slight differences and contains 118 muscle segments that wrap around the bones using contact mechanics. Using the AnyBody Modeling System a potential link between wheelchair use and shoulder pain was investigated by DUBOWSKY *et al.* (2008) and adaptations were made to use it in the context of nonconforming total shoulder arthroplasty (SINS *et al.*, 2015).

[9] Information about the Visible Human Project can be found at www.nlm.nih.gov/research/visible/visible_human.html.

Figure 20 – Geometry of the shoulder model developed by Charlton and Johnson (2006).

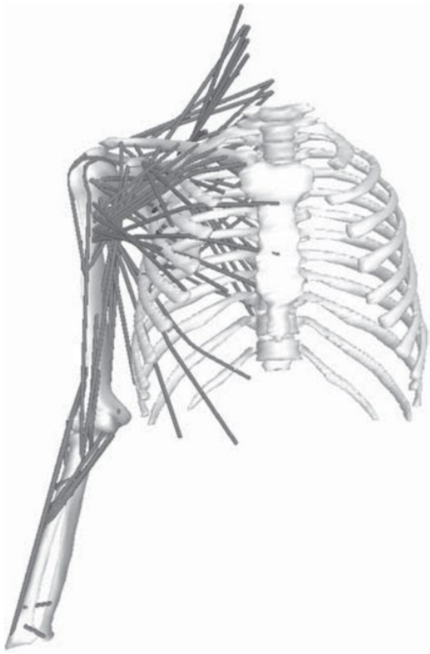

From CHARLTON and JOHNSON (2006).

Dickerson and colleagues developed a shoulder model to be used as an ergonomic analysis tool and to be compatible with existing popular ergonomics software at the time. Postural data were used as inputs to the model to obtain muscle forces and joint contact forces estimates (DICKERSON; CHAFFIN; HUGHES, 2007). Based on the work of LIPPITT and MATSEN (1993), empirical cadaver data on directional glenohumeral joint dislocation force ratios were converted into a set of linear equations to act as constraints on the joint reaction force, such that its direction did not exceed certain values that could theoretically lead to joint dislocation. This method is considered by the authors to be more physiologically consistent than the use of “an ellipsoid cone into which the glenohumeral contact force is constrained to be directed” (DICKERSON; CHAFFIN; HUGHES, 2007, p. 398).

TERRIER *et al.* (2007) developed a 3D finite element model of the shoulder using muscle activation to stabilize the glenohumeral joint. The model consists of the humerus, scapula, the rotator cuff muscles, the deltoid muscle and the cartilages of the glenohumeral joint. The muscles were partially modeled by 3D structures and partially by cables to represent the wrapping of the muscles over the humeral head (Figure 21). With six degrees of freedom, this model was used to evaluate the joint reaction force, muscle forces and the humeral head translation, highlighting the importance of the translational degrees of freedom on the evaluation of joint mechanics. Its solution to the load-sharing problem, however, involved too many simplifications, such as the merging of muscles to reduce the number of unknown variables and the use of muscle ratios based on physiological cross-sectional area (PCSA) and EMG data that was discontinued on further developments of the model.

Figure 21 – Model of the glenohumeral joint developed by Terrier *et al*. (2007). On the left its geometry is illustrated and, on the right, a simplified 2D model illustrating the forces acting on the joint and their application points.

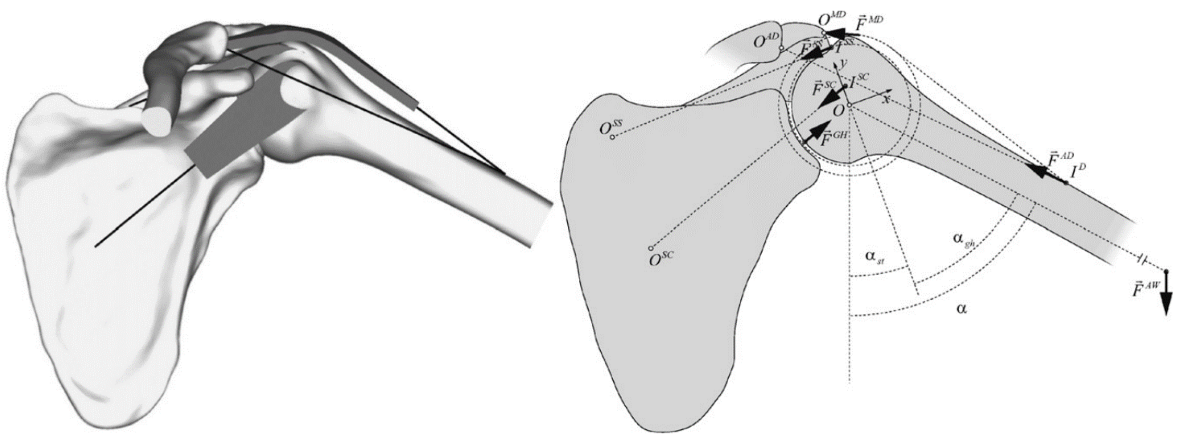

From TERRIER *et al*. (2007).

To design and test neuroprostheses, BLANA *et al.* (2008) developed a shoulder and elbow model on the software SIMM that simulates both the inverse and the forward dynamics methodologies. It was used to evaluate the restoration of the humeral elevation by stimulation of the rotator cuff muscles, highlighting their importance as humeral head elevators.

Favre and colleagues developed a six degrees of freedom finite element model of the glenohumeral joint to study its stability using an “active muscle driven humeral positioning without a priori kinematic constraint” (FAVRE *et al*., 2012, p. 2248). To that end they implemented an automated muscle wrapping technique that relied on the software contact mechanics (FAVRE; GERBER; SNEDEKER, 2010) and “an algorithm for distributing muscle forces according to their relative mechanical advantage for counteracting external moment components” (FAVRE *et al*., 2012, p. 2249). To allow all the six degrees of freedom of the joint they gradually released the translational DoF while applying the joint reaction force components calculated by their algorithm. The model was able to analyze muscle and joint reaction forces, humeral head translation and articular contact.

SINS *et al*., (2015) adapted the AnyBody model to allow five degrees of freedom on the glenohumeral joint in the context of a nonconforming total shoulder arthroplasty (SINS *et al.*, 2015). To account the two translational DoF (inferior-superior and anterior-posterior directions) an algorithm called *force-dependent kinematics* (FDK) was implemented. This algorithm describes the joint as force elements and its main assumption is “the quasi-static equilibrium between the FDK reaction forces acting between the humeral head component and the glenoid component in the directions of the FDK translations” (SINS *et al*., 2015, p. 3). The FKD also accounts the inferior glenohumeral ligament, assuming that this ligament is the primary stabilizer for inferior-superior translations. To account the articular contact, a penalty formulation was implemented to eliminate the penetration between the contact surfaces to ensure an appropriate contact representation.

Quental and co-authors published in 2016 their model of the upper limb that simulates the six degrees of freedom of the GH joint using “a novel inverse dynamics procedure that allows the evaluation of not only the muscle and joint reaction forces of the upper limb but also the GH joint translations” (QUENTAL *et al*., 2016, p. 969). Although the model is composed only of rigid bodies, they did not consider the joint as an ideal ball-and-socket. Instead, they used a spherical joint with clearance (FLORES; LANKARANI, 2010) and a Herz contact force model to describe the linear elastic force developed in the contact between the humeral head and the glenoid cavity, making it possible to account the humeral head translations. As stated by the authors, only three studies accounted the tri-dimensional humeral head translations: two finite element models (FAVRE *et al.*, 2012; TERRIER *et al.*, 2007) and one using the AnyBody model that accounted only for five degrees of freedom (SINS *et al.*, 2015). This consideration is an upgrade on their earlier model from 2012 (QUENTAL *et al.*, 2012) and showed that the joint reaction forces obtained from both models share some similarities.

A model focusing on the evaluation of the translational DoF of the humeral head was developed by SARSHARI *et al.* (2017) including a viscoelastic contact model on a non-conforming spherical glenohumeral joint to adequately define the joint contact reaction force and moment. To solve the load sharing problem (LSP), the unknown muscle and contact forces, as well as their associated moments, are defined as smooth function mappings of the generalized coordinate and velocity vectors, leading to a set of transformed equations of motion that is no longer indeterminate. Using a desired trajectory as input, this framework allows forward-dynamics simulation of the glenohumeral joint model with six degrees of freedom where the muscle forces amplitudes are defined such that the generalized coordinates and velocities of the glenohumeral joint follow their associated desired trajectories.

A model of the upper limb from OpenSim was used as a foundation by KHANDARE and VIDT (2022) to the development of a computational model that considers the 6 degrees of freedom of the glenohumeral joint. To include the three translational DoF of the humeral head, the authors included a contact mesh to the spherical surface of the humeral head and the scapula considering an elastic contact model available in OpenSim. Along with the muscles and bones from the upper limb, nine ligaments that cross the glenohumeral joint were added to the model, namely the coracohumeral ligament (one band), glenohumeral ligaments (five bands) and the posterior capsule (three bands). These ligaments were represented as non-linear elastic bands by considering normalized force-length curves obtained from the study by ELMORE and WAYNE (2013). The scapular plane abduction of the shoulder was simulated using the OpenSim's Computed Muscle Control algorithm that compute the muscle excitation by static optimization at angles 0º, 15º, 30º, and 45º, considering a set of desired kinematics and using as the objective function the weight quadratic sum of muscle activations and residual torques.

A finite element model of the shoulder complex was developed by ZHENG *et al.* (2020a) based on subject-specific data acquired from magnetic resonance imaging from the right shoulder of a volunteer. The FE model consists of 3D geometries of the rotator cuff muscles, humerus, scapula, clavicle, coracohumeral ligament, glenohumeral ligaments, and the cartilages of the humeral head and glenoid fossa. The cartilages and muscles were represented using a linear elastic material model while the ligaments were represented using a hypoelastic material model. The objective of this model was to analyze the glenohumeral motion, stress/strain distribution on soft tissues and mechanical contact characteristics. To this end, the FE model was coupled with a rigid body model using the OpenSim software, from which the muscle forces were determined using an inverse dynamic method based on data obtained from motion capture. In the FE model, the force exerted by the deltoid was applied on its insertion site pointing towards its origin in the scapula and clavicle while the forces exerted by the rotator cuff muscles were applied through muscle contraction by pre-stressing the muscle belly to match the forces calculated using the RB model. The tridimensional geometries of the soft tissues also acted as passive stabilizers by naturally constraining the humeral head, which was free to move in its six degrees of freedom throughout the simulation.

Another finite element model of the shoulder was developed by SADEQI *et al.* (2023) and made available to the community for download. The model was constructed in Abaqus/Explicit using data from the Visible Human Project and includes the humerus, scapula, clavicle, glenoid labrum and the cartilages from the humeral head and glenoid fossa. The cartilages were represented as thin layers with constant thickness covering their respective underlying bones using a Neo-Hookean hyperelastic material model. The muscle-tendon units were represented as 2D line actuators connecting the insertion and origin regions that do not wrap around the humeral head or adjacent tissues. To simulate the abduction motion of the shoulder in the scapular plane, muscle forces acquired from a previous study (YANAGAWA *et al.*, 2008) were applied directly to the connector elements of the muscle-tendon units along with displacement/rotation control boundary conditions.

In conclusion, recent advancements in shoulder modeling have increasingly focused on incorporating deformable cartilages of the glenohumeral joint to accurately compute humeral head translations and the moments generated by joint contact. This can be achieved through the integration of finite element models with rigid body models or by incorporating contact formulations directly within rigid body models. These approaches enhance the precision of biomechanical simulations, offering deeper insights into joint mechanics and stability.

## 3.2 MODELING OF SOFT TISSUES

### 3.2.1 Glenohumeral joint cartilages

The glenohumeral joint has been traditionally modeled as a spherical joint with no translations (IANNOTTI; SCHNECK; GABRIEL, 1992; SOSLOWSKY *et al.*, 1992). However, the study from ZUMSTEIN *et al.* (2014a) suggests that the articular surfaces of both cartilages of the humeral head and the glenoid fossa are not congruent and are better represented by ellipsoid surfaces. They measured the radius of the articular surfaces of the cartilages on several planes and verified by circle fitting the mismatch between the humeral head cartilage and the glenoid cartilage. It is hypothesized that these differences in radii along with the deformable nature of the cartilages induce humeral head translations similar to those that were first measured by GRAICHEN *et al.* (2000). The consideration of these translations in shoulder models is paramount to evaluate the correct joint biomechanics, such as its stabilizing mechanism (PRINOLD *et al.*, 2013; TERRIER *et al.*, 2010), and to analyze the contact area and pressure that are required to assess the glenoid track (PÉCORA *et al.*, 2020).

The deformable nature of the cartilages makes the measurement of cartilage thickness a non-trivial matter because it demands a great resolution from measurement devices and postprocessing methods (GRAICHEN *et al.*, 2003). Most of the evaluations were performed using cadaver data (GRAICHEN *et al.*, 2003; SOSLOWSKY *et al.*, 1992; ZUMSTEIN *et al.*, 2014b) at the risk of measuring altered geometry due to rigor mortis, cartilage degeneration, and absence of compression forces from muscles and passive structures (SCHLEICH *et al.*, 2017). To circumvent these problems, SCHLEICH *et al.* (2017) performed the measurements on healthy and young subjects using MRI. However, the assessment was performed using 2D images on three distinct planes parallel to the coronal plane, lacking detailed information about the overall cartilage thickness distribution. In a different study, ZUMSTEIN *et al.* (2014b) reported higher thickness at the periphery of the glenoid cartilage, mainly at the anterior-inferior region, whereas at the humeral head the cartilage is thicker at the central and superior region. A comparison of thickness values throughout different studies is presented at Table 1. Overall, the studies that evaluated data from cadavers display higher values when compared to the study of SCHLEICH *et al.* (2017). It is hypothesized that the thinner cartilages on *in vivo* subjects may be due to the compression forces at the joint.

Table 1 – Thickness distribution of the humeral head and the glenoid cartilages measured by different authors. The number and age of subjects are also included for a better analysis.

| | **Soslowski et al. (1992)** | **Greichen et al. (2003)** | **Zumstein et al. (2014b)** | **Schleich et al. (2017)** |
|---|---|---|---|---|
| Number of subjects | 32 | 8 | 9 | 38 |
| Age range [year] | 49 - 90 | 31 - 69 | 20 - 63 | 21 - 29 |
| **Humeral head cartilage** | | | | |
| Mean thickness [mm] | 1,44 ± 0,3 | 1,2 ± 0,09 | 1,74 (SD 0,45) | 1,2 - 1,5 |
| Min. thickness [mm] | 0,65 ± 0,32 | - | 0,92 | 0,8 |
| Max. thickness [mm] | 2,03 ± 0,66 | 2,3 ± 0,1 | 3,32 | 2,5 |
| **Glenoid cartilage** | | | | |
| Mean thickness [mm] | 2,16 ± 0,55 | 1,7 ± 0,13 | 1,93 (SD 0,59) | 1,2 - 1,5 |
| Min. thickness [mm] | 1,14 ± 0,6 | - | 0,98 | 1,0 |
| Max. thickness [mm] | 3,81 ± 0,72 | 3,1 ± 0,1 | 4,8 | 1,8 |

From the assumption of a ball-and-socket joint on early multibody models, the cartilages' role was not assessed, *i.e.*, the deformable behavior and the difference in radius that allow most of the joint translation were neglected. Biological soft tissues have complex material properties, presenting anisotropic and non-homogeneous nature with non-linear viscoelastic behavior (ZHENG *et al.*, 2016). To account the effects of the deformable cartilage tissue, some multibody models implemented a contact model based on the Hertz law (QUENTAL *et al.*, 2016; SINS *et al.*, 2015), a pure elastic model that does not represent the viscoelastic nature of human joints (MACHADO *et al.*, 2011). SARSHARI *et al.* (2017) circumvented this limitation by approximating the cartilage as a non-linear elastic material with the addition of a viscous damping term considering, however, only one thick layer of cartilage in a rigid-to-deformable contact model. The desired deformable-to-deformable contact model can be achieved using a finite element model, in which the material properties of the cartilages are often represented by a hyperelastic material model (FAVRE *et al.*, 2012; TERRIER *et al.*, 2007; WALIA *et al.*, 2015), such as the one presented in Section 4.2.1, first used by BÜCHLER *et al.* (2002) based on the work from BENVENUTI (1998).

### 3.2.2 Muscles

The geometry of a muscle can be described as an elongated volume composed by muscle fibers between its origin and insertion at adjacent bones. Their computational representation, however, often differs from this geometry. Mostly, muscles are modeled as frictionless taut strings connecting their attachment sites that are used to derive their lines of action (GARNER and PANDY, 2000). Although this simple representation cannot fully reproduce the physiological function of a muscle, they are preferred over a more accurate one. Tridimensional models of muscles have high computational costs and require much more input data than line-segment models, such as the specification of the spatial arrangement of fiber direction (WEBB; BLEMKER; DELP, 2014). Early models modeled muscles as a combination of 3D structures linked to insertion sites by cables (BÜCHLER *et al.*, 2002; TERRIER *et al.*, 2007), but subsequent models of did not continue this approach and moved back to muscle line-segment modeling.

Musculoskeletal models describe muscle function by the force it generates and the moment they exert in the joint. To this end, a muscle line of action must be defined through the path that it follows between attachment sites on the bones at a given joint configuration. A muscle path is often modeled through the shortest distance between its insertion and origin, ideally considering bony and soft tissue obstacles on the way. It can follow the centroids of the cross-section areas of a muscle volume or follow the bony contour. Models that use the centroid line to model the muscle path usually use the obstacle set method (Figure 22) presented by GARNER and PANDY (2000):

> The method is based on the premise that the resultant muscle force acts along the locus of the transverse cross-sectional centroids of the muscle. The path of the muscle is calculated by idealizing its centroid path as a frictionless elastic band, which moves freely over neighboring anatomical constraints such as bones and other muscles. The anatomical constraints, referred to as obstacles, are represented in the model by regular-shaped, rigid bodies such as spheres and cylinders. […] Assuming that the locus of muscle centroids is knows for an arbitrary joint configuration, the obstacle set method can be used to calculate the path of the muscle for all other joint configurations. The obstacle-set method accounts not only for the interaction between a muscle and a neighboring anatomical constraint, but also for the way in which this interaction changes with joint configuration. (GARNER and PANDY, 2000, pp. 1).

Although modeling a more realistic muscle path, this method relies on data that are difficult to obtain (PRINOLD *et al.*, 2013). The bony contour method, as the name suggests, follows the shortest distance adjacent to the bones, considering their own geometry (or a smooth, simplified one) as obstacles (Figure 23). It is easy to implement and can be used on CAE softwares to automatically define the muscle path (FAVRE *et al.*, 2012). Nonetheless, care must be taken as it may lead to unrealistic muscle moment arms (PRINOLD *et al.*, 2013).

Figure 22 – Usage of the obstacle set method to represent the paths of the three heads of the triceps brachii.

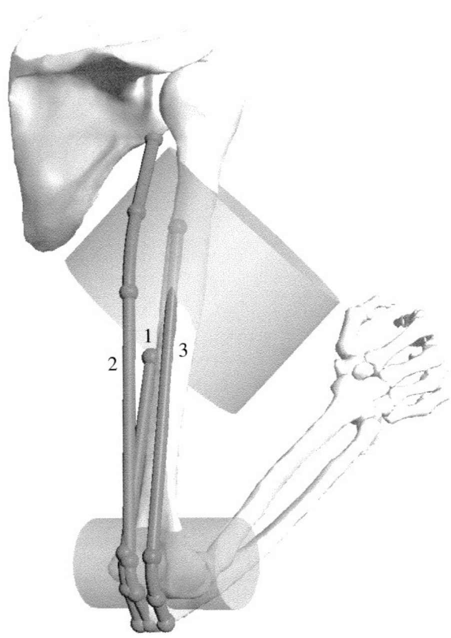


From GARNER and PANDY (2000).

Figure 23 – On the left the computational representation of the paths of shoulder muscles and on the right an artificial model of the glenohumeral joint developed by FAVRE *et al*. (2005). It depicts some of the muscles that cross the joint in which the path followed by them are adjacent to the bones.

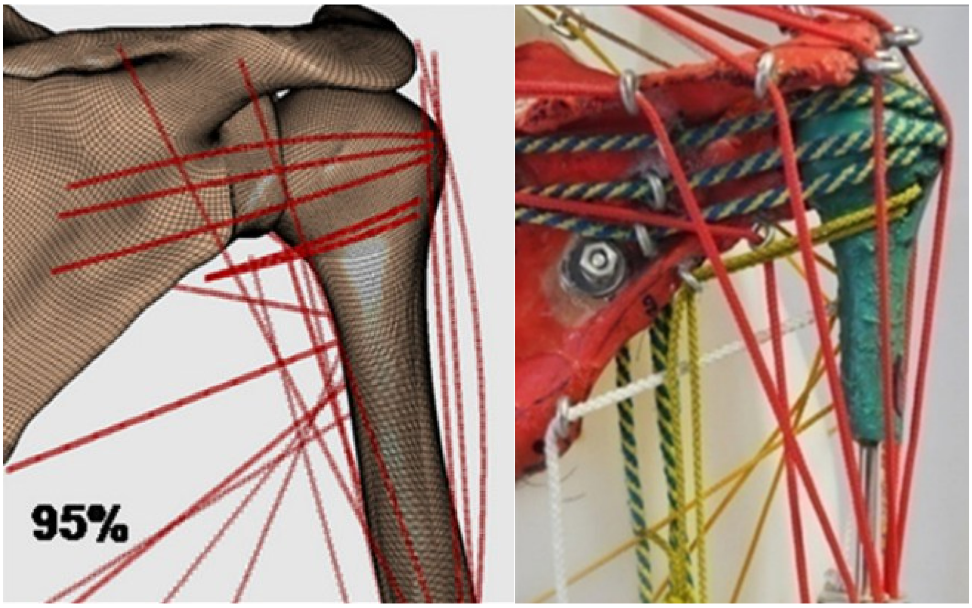


Adapted from FAVRE *et al*. (2010).

Some muscles have attachment sites big enough that they cannot be represented by a single string and are then divided into several segments “to allow for a differentiated action, as moment arm length and direction of tendon action can vary considerably within an individual muscle" (FAVRE *et al*., 2009, p. 2102). Thus, this segmentation better depicts a muscle's line of action and the force it exerts (VAN DER HELM and VEENBAAS, 1991). It can be done by homogenous division of the attachment site area (FAVRE *et al.*, 2012); by fascicular anatomy (CHARLTON and JOHNSON, 2006; JOHNSON *et al.*, 1996) ; or by its influence on a muscle's DoF (VAN DER HELM, 1994a). The number of segments that a muscle can be divided into is important for computational reasons, since it alters the number of unknowns of the problem and may influence the force exerted by a muscle. However, it is not an exact science. Several models depict muscles with different number of elements, as shown in Table 2. VAN DER HELM and VEENBAAS (1991) found that no more than six segments are necessary to represent a muscle and more than that is hardly effective.

Table 2 – Number of segments the 11 major muscles that cross the GH joint are divided into by different authors. Muscles with more than six segments are composed of sub volumes that act independently from each other and are segmented accordingly.

| Muscle | Charlton and Johnson (2006) | Dickerson et al. (2007) | Favre et al. (2010) | Nikooyan et al. (2011) | Quental et al. (2015) |
|---|---|---|---|---|---|
| Subscapularis | 3 | 3 | 3 | 11 | 11 |
| Supraspinatus | 1 | 1 | 2 | 4 | 4 |
| Infraspinatus | 3 | 2 | 3 | 6 | 6 |
| Teres minor | 1 | 1 | 2 | 3 | 3 |
| Deltoid | 5 | 3 | 6 | 15 | 15 |
| Triceps | 2 | 3 | 1 | 4 | 3 |
| Biceps | 2 | 2 | 2 | 4 | 2 |
| Coracobrachialis | 2 | - | 1 | 3 | 1 |
| Teres major | 1 | - | 1 | 4 | 1 |
| Latissimus dorsi | 5 | 2 | 3 | 6 | 3 |
| Pectoralis major | 10 | 1 | 3 | 8 | 3 |

### 3.2.3 Muscle forces and the Load Sharing Problem

Articulations such as the glenohumeral have more muscles that cross around it than joint degrees of freedom. The recruitment of adequate muscles to move the joint or to stabilize it in a certain position is performed by the neuronal control system. However, the recruitment criteria are not yet known. On musculoskeletal models, it is translated into an overactuated system, where the presence of more unknown variables than degrees of freedom prevent the finding of a unique solution. This problem is known as the load sharing problem and several methods were tailored to solve it, from reducing the number of unknown variables by merging muscles (TERRIER *et al.*, 2007) to the generally used optimization procedures that rely on cost functions and constraints to simulate biological function (ERDEMIR *et al.*, 2007).

The solution of the equations that describe the movement and the equilibrium of the musculoskeletal system requires the use of an adequate technique that depends on the available data. Many models use the inverse dynamics method to predict the torque on selected joints (BLANA *et al.*, 2008; CHARLTON; JOHNSON, 2006; NIKOOYAN, Ali Asadi *et al.*, 2011; QUENTAL *et al.*, 2016; VAN DER HELM, 1994a). This method uses as input kinematic data such as bone trajectory, and its first and second derivatives in time, of the joint degrees of freedom. The main advantage of this approach is the relative ease in which these data can be measured. The forward dynamics method uses muscle force estimations and joint torques to predict joint movement. Although it enables the inclusion of humeral head translations into the equations, the acquisition of input data is difficult at best.

To obtain more theoretically reliable answers, both methods can be coupled with optimization procedures. ERDEMIR *et al.* (2007) called these methods *inverse dynamics-based static optimization*, *forward dynamics data tracking* and *optimal control strategies*. In the *inverse dynamics-based static optimization*, the joint torques are calculated using the inverse dynamics method and at each instant in time the muscle load-sharing problem is solved by minimizing an adequate objective function. In the *forward dynamics assisted data tracking* an initial set of muscle excitations are used as input to obtain optimal muscle excitations. The cost function $J$ to be minimized is the tracking error and generally takes the form of $J = \left\|\boldsymbol{q} - \boldsymbol{q}_{exp}\right\|$, where $\boldsymbol{q}$ is the predicted trajectory from the forward dynamics' method, and $\boldsymbol{q}_{exp}$ is the experimental trajectory. *Optimal control strategies* are very similar to forward dynamics assisted data tracking. The inputs and outputs are the same, but instead of minimizing the error between predicted and experimental results, it optimizes a physiologically based or performance-based cost function.

Several alternative strategies have been proposed to solve the load-sharing problem. TERRIER *et al*. (2007) used a method similar to the inverse dynamics-based static optimization, where the input was the shortening of the middle deltoid. The muscle forces $F_k$ were defined as the product between a pre-defined muscle ratio $r_k$

and the force $F_{MD}$ exerted by the middle deltoid, an unknown, such that $F_k = r_k F_{MD}$. The ratios $r_k$ have constant values and are defined by multiplying the normalized values of EMG and PCSA. FAVRE *et al*. (2005) developed an algorithm involving decision-making loops to share the load between the muscles that cross the glenohumeral joint, with the goal of statically stabilizing the joint. For a given external moment, the algorithm selects an appropriate group of muscles based on their PCSA and the three orthogonal components of the moment they exert. Small force increments are iteratively assigned to these muscles to counterbalance the external moment and achieve joint stabilization. QUENTAL *et al*. (2016) introduced an inverse dynamics-based static optimization method that accounts for humeral head translations. In their approach, not only the internal forces (e.g., muscle and joint reaction forces) but also humeral head translations are considered design variables in the optimization process. SARSHARI *et al*. (2017) implemented a forward dynamics-assisted data tracking method, avoiding the use of inverse dynamics. They developed a framework to map unknown forces to unknown generalized coordinates and velocities, transforming the equations so that the system is no longer indeterminate. The load-sharing between muscles is achieved by minimizing an objective function.

### 3.2.4 Optimization procedures

Over the years many cost functions have been proposed to share load among muscles, from the minimization of physiological criteria to task-dependent ones (ERDEMIR *et al.*, 2007; PRAAGMAN *et al.*, 2006). Most shoulder models are used to analyze movements from activities of daily living, such as the abduction or flexion of the shoulder. These activities are often assumed to stimulate the muscles sub maximally and, thus, “most optimization algorithms are based on the notion that muscles are coordinated according to a minimal effort principle” (ERDEMIR *et al.*, 2007, p. 149).

Optimization procedures employ the use of objective functions related to the minimization of muscle activations, muscle forces, muscle stresses, and muscle energy, along with scaling factors based on physiological criteria. BECANOVIC *et al.* (2023) identified 15 of the most common objective functions used in the literature, from which 12 are presented in Table 3. Although the study focused on the gait movement, some of them have been applied to shoulder movements (VAN DER HELM, 1994b).

Table 3 – Examples of cost functions from the literature.

| **Name** | **Objective function** |
|---|---|
| Sum of muscle forces | $\frac{1}{n}\sum_{i=1}^{n} F_i$ |
| Sum of squares of muscle forces | $\left(\frac{1}{n}\sum_{i=1}^{n} F_i^2\right)^{1/2}$ |
| Sum of cubes of muscle forces | $\left(\frac{1}{n}\sum_{i=1}^{n} F_i^3\right)^{1/3}$ |
| Maximum of muscle forces | $\max_{i=1,\dots,n} F_i$ |
| Sum of muscle activations | $\frac{1}{n}\sum_{i=1}^{n} \frac{F_i - F_{min,i}}{F_{max,i} - F_{min,i}}$ |
| Sum of squares of muscle activation | $\left(\frac{1}{n}\sum_{i=1}^{n}\left(\frac{F_i - F_{min,i}}{F_{max,i} - F_{min,i}}\right)^2\right)^{1/2}$ |
| Sum of cubes of muscle activations | $\left(\frac{1}{n}\sum_{i=1}^{n}\left(\frac{F_i - F_{min,i}}{F_{max,i} - F_{min,i}}\right)^3\right)^{1/3}$ |
| Maximum of muscle activations | $\max_{i=1,\dots,n}\left(\frac{F_i - F_{min,i}}{F_{max,i} - F_{min,i}}\right)$ |
| Sum of muscle stresses | $\frac{1}{n}\sum_{i=1}^{n} \frac{F_i}{PCSA_i}$ |
| Sum of squares of muscle stresses | $\left(\frac{1}{n}\sum_{i=1}^{n}\left(\frac{F_i}{PCSA_i}\right)^2\right)^{1/2}$ |
| Sum of cubes of muscle stresses | $\left(\frac{1}{n}\sum_{i=1}^{n}\left(\frac{F_i}{PCSA_i}\right)^3\right)^{1/3}$ |
| Maximum of muscle stresses | $\max_{i=1,\dots,n} \frac{F_i}{PCSA_i}$ |

PRAAGMAN *et al.* (2006) argued that, although these mechanical cost functions may be related to physiological energy-consuming processes, a clear relationship have not been proven. They developed an energy-related cost function based on the two major energy-consuming processes during muscle contraction: the detachment of cross-bridges and the re-uptake of calcium. It takes upon consideration the muscle size (PCSA and length), force-length relationship and force-velocity relationships. They tested it and another cost function, the sum of muscle stress squared, using the DSEM and compared the results with experimental data that included muscle oxygen consumption. According to their results “the energy-related cost function appeared to be a better measure for muscle energy consumption than the stress cost function and led to more realistic predictions of muscle activation” (PRAAGMAN *et al.*, 2006, p. 758). However, the lack of adequate muscle force measurement techniques restricts the validation of cost functions and the analysis of which one better represents the role of the central nervous system.

### 3.2.5 Constraints on muscle forces and joint reaction force

To further improve the physiological aspects of optimization procedures, constraints are used collectively with cost functions. They are generally composed by the static balance equations, minimum and maximal values for muscle force amplitudes and a criterion that indicates joint stability. Models that use a Hill-type muscle model already have minimum and maximal values imbued within the equations. A simplified alternative to this method is to set a minimum value of zero, since a muscle can only provide a contraction force, and a maximum value according to the Fick law. It is based on the concept introduced by FICK (1910) that the maximum force a muscle can exert is linearly proportional to its PCSA, such that

$$F_i^{max} = K.PCSA_i,$$

where $K$ is a constant of proportionality estimated to range between $0.4$ to $1.0\ MN/m^2$ (CROWNINSHIELD and BRAND, 1981).

Amidst the calculations to determine the forces acting on the joint, it is important to guarantee that it will not dislocate. One way to do this is to enforce the joint reaction force to always point to the glenoid articular surface by the use of glenohumeral joint stability ratios (DICKERSON; CHAFFIN; HUGHES, 2007; FAVRE *et al.*, 2012; QUENTAL *et al.*, 2012). LIPPITT and MATSEN (1993) performed *in vitro* experiments to evaluate the stability of the humeral head on the glenoid fossa by applying a compressive force component perpendicular to the glenoid plane and tangential force components in eight equally spaced different directions until dislocation, as illustrated in Figure 24. The glenoid plane is essentially the *en face* view of the glenoid articular surface. The compressive force component is defined as the force vector perpendicular to the glenoid plane, while the tangential force components are parallel to it. They calculated the tangential to compressive force ratios in which dislocation occurred at each direction and set these values to be used as constraints, called glenohumeral joint stability ratios. These constraints are dependent on the magnitude of the applied compressive force and on the presence of the glenoid labrum.

Figure 24 – Stability ratios calculated when applying a compressive force of 50 N on a case with labrum (left) and without labrum (right).

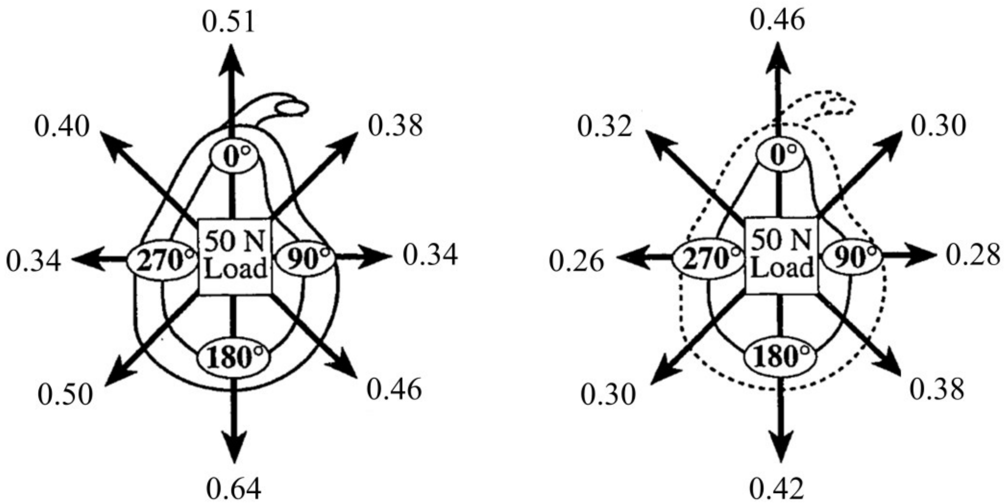


Adapted from LIPPITT and MATSEN (1993).

The relationship between the muscle segments of the same muscle should also be accounted. Most models consider that the segments of a given muscle act independently from each other (CHARLTON and JOHNSON, 2006; GARNER and PANDY, 2001; NIKOOYAN *et al.*, 2011; QUENTAL *et al.*, 2016), as done by VAN DER HELM (1994). TRICHEZ JR. *et al*. (2020) evaluated the implications of constraining the segments of the same muscle to have the same amplitude and compared it to the case where they act independently. Results showed differences on the forces exerted by the muscles in both cases and a reduction of the joint reaction force on the case with no constraints that may be due to a more flexible segment recruitment. The studies of BROWN *et al*. (2007) and RATHI *et al*. (2017) corroborates the hypothesis that muscles with large attachment sites may be divided into sub volumes that are recruited with lesser or greater intensity as a function of the movement performed. However, the evaluation of the mechanisms of muscle recruitment is still a challenge and more studies are needed to enlighten this process.

## 3.3 ANALYSIS OF GLENOID OSSEOUS DEFECTS

Most studies related to the analysis of glenoid osseous defects focused on the determination of a critical size from which bone grafting surgery becomes paramount to restore the glenohumeral joint stability. For a long time, it has been said that a bone defect of one-third of the glenoid or greater needed to be treated with bone grafting (MORREY; ITOI; AN, 1998). However, in a clinical setting, it is not practical to express the precise size of a defect as an area ratio. The definition of a critical size of a bone defect is paramount to help surgeons decide whether a bone grafting must be performed, since it is an invasive procedure with a considerable rate of complications when compared to que arthroscopic Bankart repair.

In their research, ITOI *et al.* (2000) proposed a novel approach for quantifying the size of osseous glenoid defects. Rather than using an area ratio, which had been commonly employed, they introduced the concept of expressing the defect size as a percentage of the glenoid length. This approach offered a more precise and standardized way to evaluate the extent of glenoid defects. In their study, they created and measured different sizes of osseous defects in the glenoid and assessed their effects on shoulder stability and motion after a Bankart repair. The osseous defects were created anteroinferiorly at the 4:30 clock position, as depicted in Figure 25. The procedure involved translating the humeral head 10 mm in the anteroinferior direction in the presence of a constant compressive force of 50 N with the arm in abduction and external rotation (end-range of shoulder movement) as well as with the arm in abduction and internal rotation (mid-range of shoulder movement). Results showed that the stability of the shoulder did not change significantly after Bankart repair with the arm in the end-range of movement, regardless of the size of the osseous defect. However, with the arm in the mid-range of motion, stability decreased significantly as the size of the osseous defect increased. They concluded an osseous defect with a width that is at least 21 percent of the glenoid length may lead to shoulder instability.

Figure 25 – Osteotomy lines for anteroinferior glenoid defects.

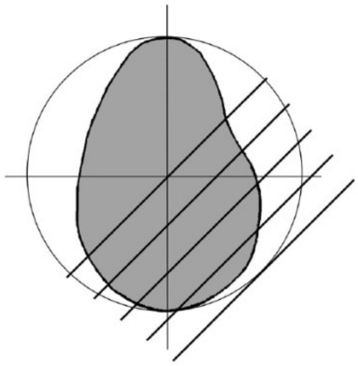

From ITOI, EIJI (2017).

Saito and colleagues (SAITO *et al.*, 2005) conducted a comprehensive analysis using 3D images of 123 patients who experienced recurrent anterior dislocation of the shoulder. Their findings revealed that the glenoid defect pointed toward 3:01 on the clock face of the glenoid (Figure 26), instead of the previously assumed 4:30 position. Based on this study, Yamamoto and colleagues (YAMAMOTO, N. *et al.*, 2009) investigated the effect of anterior glenoid defects on shoulder stability, as opposed to the formerly studied anteroinferior defects. The study concluded that an anterior glenoid defect at the 3 o'clock position, with a width equal to or greater than 20% of the glenoid length, significantly reduced anterior shoulder stability. This suggests that in cases where an anterior glenoid defect meets this criteria, reconstruction of the glenoid concavity may be necessary to restore stability.

Figure 26 – Osteotomy lines for anterior glenoid defects.

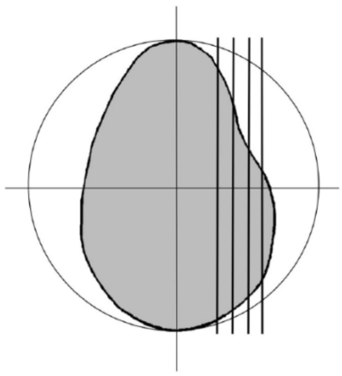

From ITOI, EIJI (2017).

YAMAMOTO *et al.* (2010) continued their investigation by delving into the stabilizing mechanism of bone-grafting in the context of glenoid defects. They sought to understand how bone-grafting could restore shoulder stability in cases of substantial defects. Testing was performed under various conditions, including the intact glenoid, simulated Bankart lesion, Bankart lesion repair, and the creation and subsequent bone-grafting of defects ranging from 2 mm to 8 mm in width. The study concluded that an osseous defect with a width equal to or greater than 19% of the glenoid length remains unstable even after Bankart lesion repair, needing a bone grafting to restore shoulder stability.

Regarding the analysis of the glenohumeral joint stability in the presence of articular bony defects, WALIA *et al.* (2015) developed a finite element model to "quantify the effect of different size combinations of Hill-Sachs defects and bony Bankart defects on shoulder instability across a broad range of motion". The model consists of the humerus, the scapula and their respective cartilages concerning the glenohumeral joint. Quasi-static analyses were performed every 10° from 40° internal rotation to 60° external rotation at 45° and 90° of abduction. To evaluate the joint stability, displacement control simulations were performed at each position of interest in the presence of a 50 N compressive load throughout the translation of the humeral head in the antero-inferior direction. Four defects were created on each articular surface with different sizes to analyze their individual and combined effects on joint stability. The size of the Hill-Sachs lesion was 6%, 19%, 31%, and 44% of the diameter of the humeral head at its anterior side and the size of the bony Bankart lesion was 12.5%, 25%, 37.5%, and 50% of the glenoid width at the antero-inferior quarter of the glenoid. A variable called distance to dislocation (DTD) was created to quantify joint stability. It measured the distance traveled by the humeral head until loss of contact. The lesser the DTD value, the lesser the joint stability. Their results show that the presence of bipolar bone losses is indeed a great risk factor to shoulder dislocation and subluxation.

One of the limitations of the aforementioned studies is the use of a non-physiological compressive force of 50 N. In contrast, the research from WESTERHOFF *et al.* (2009) have measured contact forces up to 151% body weight during activities of daily living with senior patients that had received instrumented shoulder implants. A similar trend has been observed with the use of computational shoulder models that allow humeral head translations, where the highest contact force varied between 550 N and 690 N (JUNIOR *et al.*, 2022; SARSHARI *et al.*, 2017; TERRIER *et al.*, 2007) during abduction of the shoulder.

In an effort to surpass the limitations from earlies studies, (KLEMT *et al.*, 2019) investigated the critical size of an osseous defect in the glenoid during 30 functional activities that could lead to further anterior instability of the shoulder despite undergoing a Bankart repair. The model consisted of the proximal humerus, the lateral scapula, the humeral head cartilage, the glenoid cartilage, and the glenoid labrum. For each size of the defect, a simulated Bankart repair was performed by reattaching the labrum to the osteotomy line, aiming to restore the natural concavity of the glenoid. They used physiological joint loading conditions that were calculated using the computational rigid body model from (CHARLTON and JOHNSON, 2006). Under compressive forces thus calculated, an anterior translation was applied to the humeral head and the tangential forces were measured. The highest tangential force obtained from this procedure was compared with the physiological tangential force obtained from the rigid body model to determine whether a dislocation occurred. The results indicated that there was a high risk of shoulder dislocation during the functional activities even after a Bankart repair had been performed. This high risk was observed for anterior defects that corresponded to as little as 16% of the length of the glenoid.

# 4 METHODS

## 4.1 MODELING OF THE GLENOHUMERAL JOINT

The computational model was developed based on magnetic resonance imaging (MRI) and computed tomography (CT) scan data acquired from the right shoulder of a healthy male subject, aged 24, with a body mass of 70 kg and a stature of 1.72 meters. The image acquisition procedure was conducted at the IOT-HC-FMUSP as part of another doctoral thesis (PÉCORA *et al.*, 2020). The MRI scan was executed with the subject in a supine position, while maintaining the arm at 0º of abduction and 90º of external rotation. This facilitated the collection of necessary data pertaining to the geometries of the humeral head cartilage, glenoid cartilage, and the insertion sites of the rotator cuff muscles on the scapula. The CT scan was conducted with the subject in a supine position and the arm positioned at 0º, 30º, 60º, 90º, 120º and 150º, while maintaining 90º of external rotation. This procedure was instrumental in acquiring data concerning the geometrical attributes of the skeletal structures and their respective spatial relationships.

The model encompasses the humerus, scapula, humeral head cartilage, glenoid cartilage, deltoid muscle, and rotator cuff muscles. The geometric representation of these structures (Figure 27) was made using a CAD software (SolidWorks) by a third-party personal, integrating information from image exams and relevant literature sources. To accommodate the insertion sites of the deltoid muscle, the humeral shaft was partially configured as a cylinder. The placement of these muscular insertion sites on the scapula is described in the work of FAVRE; GERBER and SNEDEKER (2010) and were adapted to match our model.

A local coordinate system, as depicted in Figure 28, is established with its origin coincident with the nominal rotation center. This center is determined by fitting a sphere, possessing a diameter similar to the dimensions of the articular surface of the humeral head cartilage, within the glenoid cartilage articular surface, as outlined by VEEGER (2000). In this system, the $z$ axis is oriented perpendicular to the center of the glenoid cartilage articular surface in the lateral-medial direction, intersecting through the center of the fitted sphere. The $y$ axis is defined along the inferior-superior direction, while the $x$ axis is orthogonal to the $yz$ plane, in the anterior-posterior direction. The $xy$ plane is also called the glenoid plane. This coordinate system, which is anchored to the scapula, provides a more effective framework for analyzing the forces exerted on the joint, particularly in relation to their stabilizing capacities.

Figure 27 – Model of the glenohumeral joint including the cartilages and the bones.

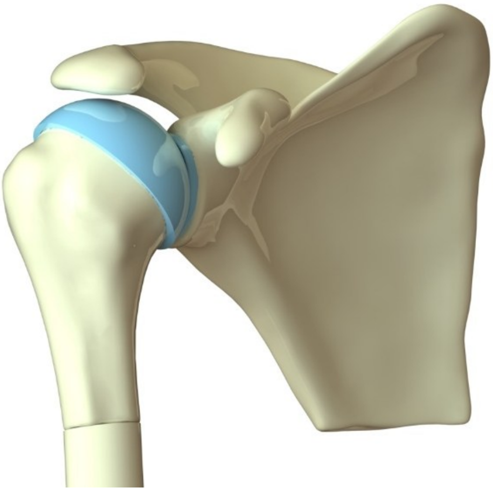

From the author.

Figure 28 – Local coordinate system.

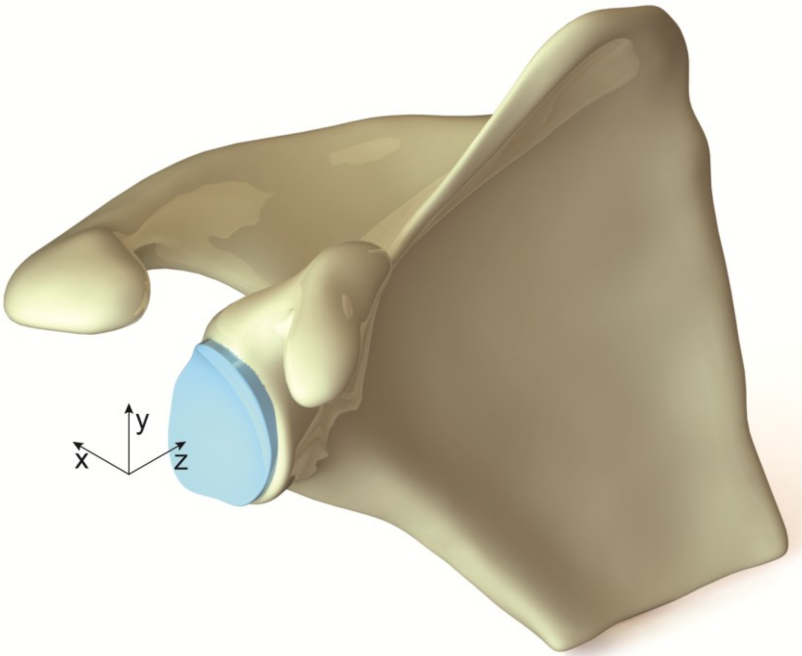


From the author.

The articular surfaces of the humeral head cartilage and the glenoid cartilage were characterized as non-congruent ellipsoid surfaces, replicating the geometry derived from clinical examinations of the individual from which the MRI and TC scan were performed. The radii of the ellipsoids used to design the cartilages are presented in Figure 29 and Figure 30. The thickness of these cartilaginous structures was determined from clinical imaging data, exhibiting variations in thickness due to the irregular bone morphology of the humeral head and glenoid fossa. Specifically, the humeral head cartilage displayed an average thickness of 1.96 mm, with a range from 0.72 mm to 3.25 mm. In contrast, the glenoid cartilage exhibited an average thickness of 2.23 mm, ranging from 1.35 mm to 4.86 mm. Details about the construction of each cartilage are presented in Appendix A.

Figure 29 – Radii of the ellipsoid structure used to create the articular surface of the glenoid cartilage.

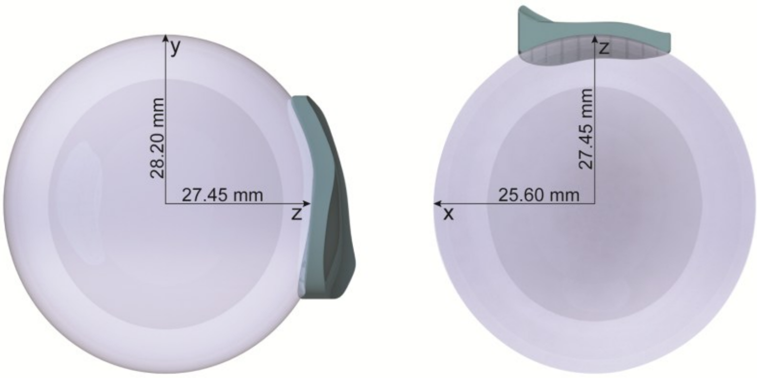


From the author.

Figure 30 – Radii of the humeral head cartilage.

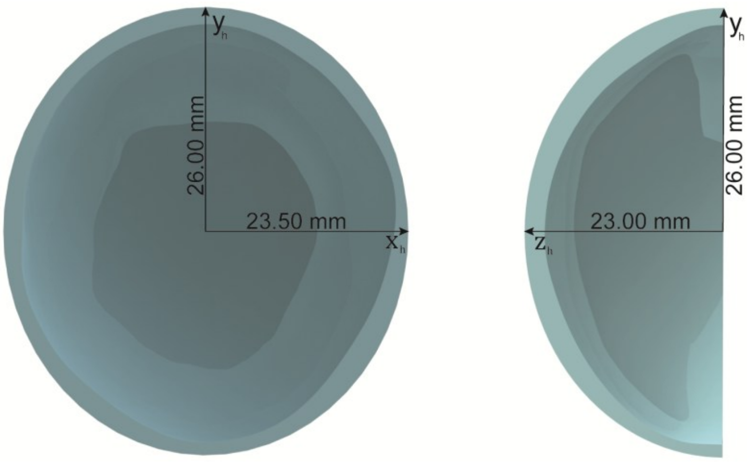


From the author.

The muscles are described as frictionless taut strings and are segmented to better represent their anatomical function, as there are muscle attachment footprints big enough that cannot be correctly represented using only one segment. The number of segments for each muscle are in accordance with the data provided by FAVRE; GERBER and SNEDEKER (2010), which is summarized in Table 4, to correspond to the attachment locations acquired from their study. Out of the eleven muscles traversing the glenohumeral joint, only five have been incorporated in this model: the deltoid, supraspinatus, subscapularis, infraspinatus, and teres minor. These specific muscles were selected due to their roles as primary stabilizers and abductors of the glenohumeral joint. The rotator cuff muscles were represented using two supraspinatus, three infraspinatus, three subscapularis, and two teres minor segments. The deltoid muscle was divided into six segments (one anterior, three middle, and two posterior segments).

Table 4 – Muscle segmentation.

| **Muscles** | **Segments** |
|---|---|
| Supraspinatus | Anterior supraspinatus |
| | Posterior supraspinatus |
| Subscapularis | Superior subscapularis |
| | Middle subscapularis |
| | Inferior subscapularis |
| Infraspinatus | Superior infraspinatus |
| | Middle infraspinatus |
| | Inferior infraspinatus |
| Teres minor | Superior teres minor |
| | Inferior teres minor |
| Anterior deltoid | Anterior deltoid |
| Middle deltoid | Anterior middle deltoid |
| | Middle middle deltoid |
| | Posterior middle deltoid |
| Posterior deltoid | Anterior posterior deltoid |
| | Posterior posterior deltoid |

The trajectory of each muscle is delineated in Abaqus/Explicit using the bony contour technique (FAVRE; GERBER; SNEDEKER, 2010), wherein the muscles envelop the bones between their respective attachment areas. This approach removes the requirement for predefined via points and wrapping surfaces, allowing for automatic, penetration-free, multi-object wrapping of muscles around complex bone geometries. A detailed explanation of this procedure is presented in Section 4.2.2.

## 4.2 FINITE ELEMENT MODEL

### 4.2.1 Finite element model using Abaqus/Standard

The finite element model was created using the Abaqus/Standard software platform (Figure 31). The bones were represented as rigid bodies, while the cartilages were characterized by a hyperelastic Neo-Hookean material model exhibiting isotropy and non-linearity, represented by the following elastic strain energy potential:

$$W = C_{10}(\bar{I}_1 - 3) + \frac{1}{D_1}(J - 1)^2,$$

where, for consistency with linear elasticity,

$$C_{10} = \frac{\mu}{2} \text{ and } D_1 = \frac{\lambda_L}{2}.$$

The parameters $\lambda_L$ and $\mu$ are the first and second Lamé parameters, respectively, and $\bar{I}_1$ is the first invariant of the isochoric part of the right Cauchy-Green deformation tensor. Alternatively,

$$C_{10} = \frac{E}{4(1+\nu)} \text{ and } D_1 = \frac{6(1-2\nu)}{E}.$$

where $E = 10\ MPa$ and $\nu = 0.4$ (BÜCHLER *et al.*, 2002; FAVRE *et al.*, 2012; TERRIER *et al.*, 2008; WALIA *et al.*, 2015). The reference point of the humerus is coincident with the origin of the local coordinate system. The interaction between cartilages was modeled as frictionless, following the approach by FAVRE *et al.* (2012). The bones were discretized using rigid elements (R3D3), while the cartilages were meshed with second-order tetrahedral elements (C3D10M), which are particularly well-suited for simulations involving contact, non-linear kinematics, and hyperelastic materials. The convergence study to determine the mesh size is presented in APPENDIX A.

Figure 31 – Mesh of the glenohumeral joint bones and cartilages.

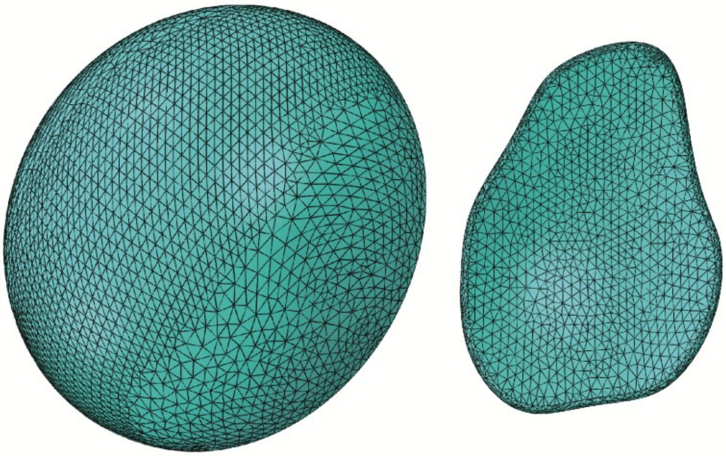

From the author.

### 4.2.2 Muscle path using Abaqus/Explicit

The tracing of the muscle path for the selected muscle segments is conducted utilizing the Abaqus/Explicit software package. This procedure is performed in a manner akin to the methodology described by FAVRE; GERBER and SNEDEKER (2010, p. 1932):

> The muscles are modeled as a straight series of beam elements with very low bending stiffness. They are anchored at their insertion to the humerus with a predefined orientation (insertion nodes are constrained to prohibit translations but allowed three degrees of freedom in rotation), but not yet attached at their origin on the scapula. A wrapping step then displaces the free end node of each segment toward its predefined origin on the scapula. Along the way, the muscle elements wrap around relevant bone surfaces, relying on contact detection of the FE software. […] the main benefit of our method over the obstacle-set method is the ability to wrap around complex geometries without the need to define artificial obstacles or via points. […] As with the obstacle-set and via point methods, the major benefit compared to volumetric models is drastically lower computational expense. […] This allows the complete shoulder model to run on a standard desktop PC and would permit simultaneous use of a wrapping algorithm in conjunction with muscle force estimation models.

Figure 32 – The muscle paths of the infraspinatus and of the teres minor are represented by black lines. The directions of the forces exerted by the infraspinatus segments are represented by red arrows and the directions of the forces exerted by the teres minor segments are represented by blue arrows.

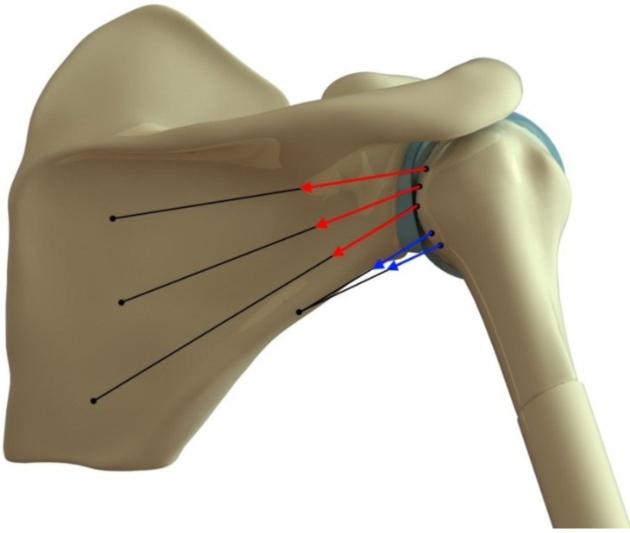

From the author.

Figure 33 – In black, the muscle path of the middle segment of the subscapularis. The red arrow represents the direction of the force exerted by this muscle segment.

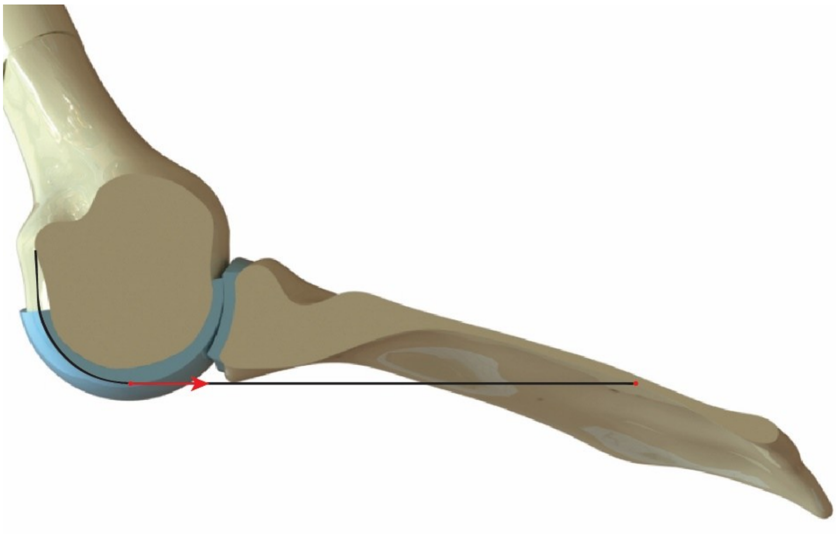

From the author.

The orientation of the muscle forces, represented as unitary vectors $\boldsymbol{d}_m$, are established based on their points of insertion on the humerus and the respective muscle paths. For muscle segments that do not wrap around bone surfaces, $\boldsymbol{d}_m$ is determined from their insertion points to their origin points, as illustrated in Figure 32.

In contrast, for muscle segments that do wrap around bone surfaces, $\boldsymbol{d}_m$ is derived from the final contact point (as detected using Abaqus) on the wrapped surface to the origin point on the scapula, as illustrated in Figure 33. The point where the muscle force vector is applied is called $\boldsymbol{x}_m$.

The point of application $\boldsymbol{x}_p$ for the arm weight $\boldsymbol{p} = P\boldsymbol{d}_p$, where $P$ is the arm weight amplitude, is situated 320 mm distant from the center of the humeral head (POPPEN and WALKER, 1978). The unitary direction $\boldsymbol{d}_p$ is defined with the arm at 0º of abduction along the humeral shaft, oriented downwards, under the assumption of an upright subject, as illustrated in Figure 34.

Figure 34 – Arm weight vector at 0º degrees of abduction.


From the author.

As described in Section 2, the abduction movement involves the combined motion of the glenohumeral and scapulothoracic joints, giving rise to the scapulohumeral rhythm. In the computational model, the scapula is assumed to remain fixed in space. To account for scapular rotation under this assumption, the arm weight vector $\boldsymbol{p}$ is rotated throughout the abduction movement. This adjustment ensures that the biomechanical representation remains realistic. Figure 35 illustrates this concept: instead of simulating scapular rotation (A), the arm weight vector $\boldsymbol{p}$ rotates (B) to align with the abduction movement in a biofidelic manner.

Figure 35 – Arm weight direction at 90º of abduction.

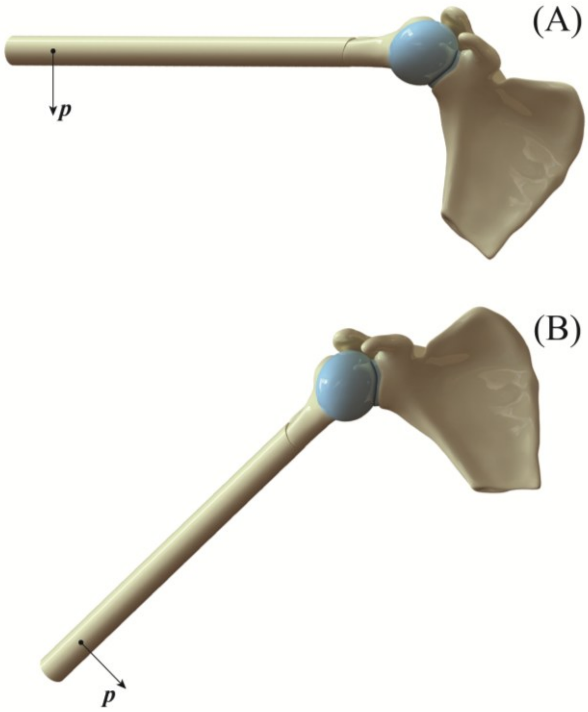


From the author.

## 4.3 THE LOAD SHARING PROBLEM AT THE GLENOHUMERAL JOINT

The forces acting on the glenohumeral joint are the arm weight $\boldsymbol{p}$, the forces exerted by the muscle segments $\boldsymbol{f}_m$, and the joint reaction force $\boldsymbol{r}_a$, which is defined as the resultant force due to the contact between the articular surfaces. To achieve joint stabilization at a specific abduction angle $\theta$, the system must be in mechanical balance:

$$\boldsymbol{f}_r = \boldsymbol{p} + \boldsymbol{r}_a + \sum_{m=1}^{M} \boldsymbol{f}_m = \boldsymbol{0}, \quad (1)$$

$$\boldsymbol{m}_r = \boldsymbol{m}_p + \boldsymbol{m}_a + \sum_{m=1}^{M} \boldsymbol{m}_m = \boldsymbol{0}. \quad (2)$$

In Equations (1) and (2):

- $M$ is the total number of muscles segments;

- $\boldsymbol{f}_m = F_m \boldsymbol{d}_m$ is the force exerted by muscle segment $m$, where $F_m$ is the force amplitude and $\boldsymbol{d}_m$ the muscle force direction;
- $\boldsymbol{m}_m = \boldsymbol{x}_m \times \boldsymbol{f}_m$ is the moment generated by muscle segment $m$, where $\boldsymbol{x}_m$ is the point of application of $\boldsymbol{f}_m$;
- $\boldsymbol{p} = P\boldsymbol{d}_{\boldsymbol{p}}$ is the arm weight vector with an amplitude $P = 35\ N$ (POPPEN; WALKER, 1978) and direction $\boldsymbol{d}_p$;
- $\boldsymbol{m}_p = \boldsymbol{x}_{\boldsymbol{p}} \times \boldsymbol{p}$ is the moment generated by $\boldsymbol{p}$, where $\boldsymbol{x}_p$ is its application point; and
- $\boldsymbol{r}_a$ and $\boldsymbol{m}_a$ are the joint reaction force and moment, respectively.

Assuming that the muscle force direction $\boldsymbol{d}_m$, the application points $\boldsymbol{x}_m,\ \boldsymbol{x}_p$, and the arm weight $\boldsymbol{p}$ are known, the system comprises a total of 16 unknown scalar variables and one unknown vector variable:

- the muscle forces amplitudes $F_1, \dots, F_M$ for $M = 16$, and
- the joint reaction moment three-dimensional vector $\boldsymbol{m}_a$.

Although not known a priori, the joint reaction force $\boldsymbol{r}_a$ is obtained from Eq. (1) as a linear combination of the arm weight and muscle forces:

$$\boldsymbol{r}_a = -\boldsymbol{p} - \sum_{m=1}^{M} \boldsymbol{f}_m. \tag{3}$$

Since only six equilibrium equations are available (Eq. (1 and (2), there is no single solution to this problem, called load sharing problem. In order to obtain a physiologically adequate solution among all the possible ones, an optimization problem was formulated. To this aim, let $\boldsymbol{F}$ be the array of variables containing the amplitudes of muscle forces,

$$\boldsymbol{F} = \{F_1, \dots,\ F_M\},$$

belonging to the design space

$$\boldsymbol{\Omega} = \{\boldsymbol{F} \in \mathbb{R}^M \colon 0 \le F_m \le F_m^{max} \mid \frac{r_{a,x}}{r_{a,z}} < C_x;\ \frac{r_{a,y}}{r_{a,z}} < C_y;\ \|\boldsymbol{r}_a\| < R_c;\ \boldsymbol{r}_a = -\boldsymbol{p} - \sum_{m=1}^{M} \boldsymbol{f}_m\}.$$

Note that, within this set,

- the muscle force amplitudes $F_m$ are submitted to side constraints, in which $F_m^{max}$ is the maximum force a muscle segment $m$ can exert. Values for $F_m^{max}$ were based on the literature (FAVRE *et al.*, 2005) and are presented in Table 5;
- $C_x$ and $C_y$ are the glenohumeral ratios in directions $x$ and $y$ of the local coordinate system, respectively. They enforce the direction of the joint reaction force $\boldsymbol{r}_a$ to be within a cone with axis direction $z$ ,*i.e.*, normal to the glenoid plane of reference (see Section 3.2.5). The procedure to determine the values for $C_x$ and $C_y$ and the results obtained are described in APPENDIX B;
- the reaction amplitude $\|\boldsymbol{r}_a\|$ is bounded by $R_c$, which, in effect, indirectly constrain the forces the muscle segments can exert;
- forces are constrained to satisfy linear momemtum balance.

Table 5 – Muscle segments maximum allowed forces.

| Muscles | Segments | Variable | Maximum force (N) |
|---|---|---|---|
| Supraspinatus | Anterior supraspinatus | $\boldsymbol{f}_1$ | 260 |
| | Posterior supraspinatus | $\boldsymbol{f}_2$ | 260 |
| Subscapularis | Superior subscapularis | $\boldsymbol{f}_3$ | 450 |
| | Middle subscapularis | $\boldsymbol{f}_4$ | 450 |
| | Inferior subscapularis | $\boldsymbol{f}_5$ | 450 |
| Infraspinatus | Superior infraspinatus | $\boldsymbol{f}_6$ | 320 |
| | Middle infraspinatus | $\boldsymbol{f}_7$ | 320 |
| | Inferior infraspinatus | $\boldsymbol{f}_8$ | 320 |
| Teres minor | Superior teres minor | $\boldsymbol{f}_9$ | 100 |
| | Inferior teres minor | $\boldsymbol{f}_{10}$ | 100 |
| Anterior deltoid | Anterior deltoid | $\boldsymbol{f}_{11}$ | 860 |
| Middle deltoid | Anterior middle deltoid | $\boldsymbol{f}_{12}$ | 290 |
| | Middle middle deltoid | $\boldsymbol{f}_{13}$ | 290 |
| | Posterior middle deltoid | $\boldsymbol{f}_{14}$ | 290 |
| Posterior deltoid | Anterior posterior deltoid | $\boldsymbol{f}_{15}$ | 430 |
| | Posterior posterior deltoid | $\boldsymbol{f}_{16}$ | 430 |

To solve the LSP, a performance function called relative residual moment is defined as

$$\varepsilon = \frac{\|\boldsymbol{m}_r\|}{\|\boldsymbol{m}_p\|}. \tag{4}$$

The relative residual moment $\varepsilon$ is a measure of the amplitude of the unbalanced moment $\boldsymbol{m}_r$ acting on the humeral head (Eq. 2) compared to the amplitude of the moment $\boldsymbol{m}_p$ generated by the arm weight. It is then postulated that a possible solution of the balance equations (1) and (2) can be found by solving the following minimization (LSP) problem:

$$LSP = min\,\varepsilon(\boldsymbol{F}) \tag{5}$$

$$\boldsymbol{F} \in \boldsymbol{\Omega}$$

This setup seeks a set of non-negative muscle forces amplitudes $\boldsymbol{F}$ that stabilize the glenohumeral joint at a given joint abduction angle $\theta$. Note that, by definition, the minimum attainable value of relative residual moment is $\varepsilon = 0$, which means that the angular momentum balance (Eq. 2) has been achieved. The numerical algorithm stops when $\varepsilon < tol_\varepsilon$ with $tol_\varepsilon = 10^{-6}$.

## 4.4 SIMULATION FRAMEWORK

Although the results from solving the load sharing problem achieve mechanical balance, they represent only part of the solution for overall joint stabilization. Given the nature of the objective function, many global minimizers $\boldsymbol{F}$ are expected, justifying the use of a genetic algorithm for the optimization procedure. Among the possible solutions, the wanted solution is the one that satisfy the principle of the minimum effort (ERDEMIR *et al.*, 2007), *i.e.*, that minimizes the reaction force amplitude $\|\boldsymbol{r}_a\|$. This principle is implemented by a sequential reduction of the constraint value $R_c$ on the design space $\boldsymbol{\Omega} = \boldsymbol{\Omega}(R_c)$ driving the muscle forces to progressively lower values until there is no null minimum solution of Eq. (5), which means that mechanical balance is not achievable. From Eq. 3, $\boldsymbol{r}_a$ is a linear combination of the muscle forces $\boldsymbol{f}_m$ and the arm weight $\boldsymbol{p}$. Since the arm weight $\boldsymbol{p}$ remains constant during the resolution of the LSP, the constraint $R_c$ effectively limits the sum of the amplitude of the muscle forces. By imposing small values for $R_c$, the optimization procedure that solves the LSP is forced to find a solution set of muscle force amplitudes $\boldsymbol{F} = \{F_1, \ldots, F_M\}$ with minimal values.

The smallest set of balanced muscle forces $\boldsymbol{F}$ identified through the above-described process is then exported to the finite element model to determine the humeral head position where mechanical equilibrium is achieved. This new humeral head position differs, in general, from the initial assumption, inducing a joint reaction moment different from the one used in the LSP. The new geometry is then updated into the rigid body model for another iteration of the LSP. This iterative procedure continues until a stable convergent position is reached, defined as the humeral head position where the difference in joint reaction moment between the RB model and the FE model falls below a specified threshold.

The Simulation Framework is divided into four modules that are iteratively connected using the toolbox Abaqus2MatLab (PAPAZAFEIROPOULOS; MUÑIZ-CALVENTE; MARTÍNEZ-PAÑEDA, 2017): **Module Shoulder Abduction**, **Module Muscle Path**, **Module Muscle Forces**, and **Module Simulation**. The emphasis $\overline{(\cdot)}$ above some of the variables indicates that this variable is a function of the smallest set of muscle forces $\overline{\boldsymbol{F}}$ obtained from **Module Muscle Forces**. The interaction among the Modules is illustrated in Figure 36 and presented in Table 9 at the end of this Section.

Figure 36 – Fluxogram illustrating the interaction among Modules.

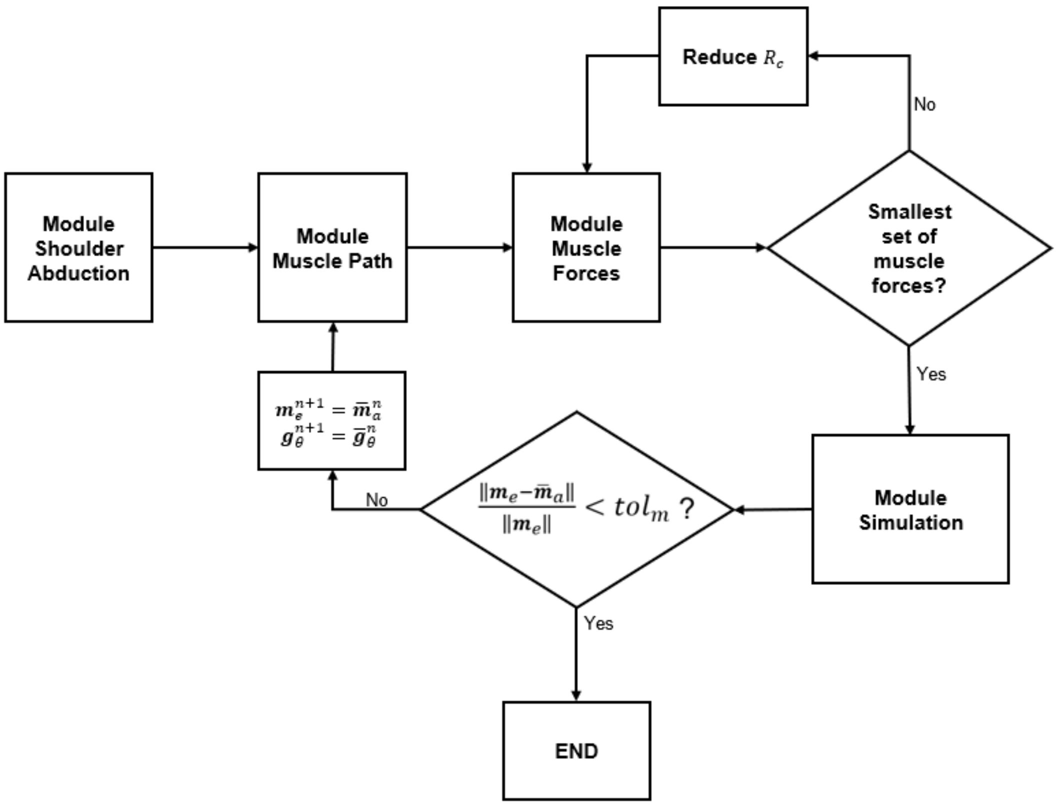

The **Module Shoulder Abduction** sets the initial geometric conditions. The humerus abduction angle $\theta \in [30°,\ 120°]$ is defined and the position of the humeral head center $\boldsymbol{g}_\theta^0$ is calculated (Table 6).

Table 6 – Inputs and output of Module Shoulder Abduction.

| | | |
|---|---|---|
| INPUT | $\theta$ | Humerus abduction angle |
| OUTPUT | $\boldsymbol{g}_\theta$ | Humeral head center |

Within the module **Muscle Path,** the paths of the muscles are defined, establishing their lines of action and the direction of the muscle forces (Table 7) as described in Section 4.2.2.

Table 7 – Inputs and outputs from Module Muscle Path.

| | | |
|---|---|---|
| INPUT | $\boldsymbol{g}_\theta$ | Humeral head center |
| OUTPUT | $\boldsymbol{d}_m$ | Direction of the muscle force vectors |
| | $\boldsymbol{x}_m$ | Insertion point for the muscle force vectors |
| | $\boldsymbol{d}_p$ | Direction of the arm weight |
| | $\boldsymbol{x}_m$ | Insertion point of the arm weight |

In **Module Muscle Forces**, a solution set $\boldsymbol{F} = \{F_1, \ldots, F_M\}$ of the Load Sharing Problem (LSP) is said to be feasible if it generates a relative residual moment $\varepsilon < tol_\varepsilon$, for $tol_\varepsilon = 10^{-6}$, which means that the mechanical balance has been achieved. This module solves the LSP iteratively for decreasing values of $R_c$ until the smallest set of feasible muscle forces $\overline{\boldsymbol{F}}$ are found (Table 8), defined as $\overline{\boldsymbol{F}} = \boldsymbol{F}^{K-1}$, where $K$ is the number of iterations performed.

The muscle forces $\overline{\boldsymbol{f}} = \boldsymbol{f}(\overline{\boldsymbol{F}})$ obtained from **Module Muscle Forces** and the arm weight $\boldsymbol{p}$ are applied directly to the humerus Reference Point in **Module Simulation**. Throughout the finite element simulation, the scapula maintains a fixed position in space, with only the humerus undergoing translational motion. To facilitate convergence, the translational degrees of freedom of the humerus are progressively released. This commences with the release of the $z$-axis DoF within the local coordinate system, followed by the $y$ and $x$ axes. Moreover, rotational DoF of the humerus are constrained to ensure convergence. To further enhance simulation stability and convergence, both automatic stabilization and adaptive stabilization techniques are employed, with a maximum stabilization-to-strain energy ratio set at 0.05 and a maximum dissipated energy fraction equal to 0.0002.

Table 8 – Inputs and outputs for Module Muscle Forces.

| | | |
|---|---|---|
| INPUT | $\boldsymbol{g}_\theta$ | Position of the humerus at joint angle $\theta$. |
| | $\boldsymbol{F}_{init}$ | Muscle force amplitudes to be used as initial population. |
| | $\boldsymbol{d}_m$ | Direction of the muscle force vectors. |
| | $\boldsymbol{x}_m$ | Application point for the muscle force vectors. |
| | $\boldsymbol{p}$ | Arm weight $\boldsymbol{p} = P\boldsymbol{d}_p$. |
| | $\boldsymbol{m}_p$ | Arm weight moment $\boldsymbol{m}_p = \boldsymbol{x}_p \times \boldsymbol{p}$. |
| | $C_x$ | Glenohumeral ratio constraint in direction $x$. |
| | $C_y$ | Glenohumeral ratio constraint in direction $y$. |
| | $R_c$ | Joint reaction force amplitude constraint. |
| | $F_m^{max}$ | Maximum force amplitude that a muscle segment $m$ can exert. |
| | $\boldsymbol{m}_e$ | Estimated joint reaction moment. |
| | $B$ | Reduction factor for $R_c$. |
| | $tol_\varepsilon$ | Specified tolerance for the relative residual moment. |
| | $\varepsilon_m$ | Relative residual moment. |
| | $\boldsymbol{r}_a$ | Joint reaction force. |
| OUTPUT | $\overline{\boldsymbol{F}}$ | Set of the smallest feasible muscle forces amplitudes. |
| | $\bar{\boldsymbol{f}}_m$ | Feasible muscle forces $\bar{\boldsymbol{f}}_m = \boldsymbol{f}_m(\bar{F}_m)$. |
| | $\bar{\boldsymbol{r}}_a$ | $\bar{\boldsymbol{r}}_a = \boldsymbol{r}_a(\overline{\boldsymbol{F}})$. |
| | $\bar{\varepsilon}_m$ | $\bar{\varepsilon}_m = \varepsilon_m(\overline{\boldsymbol{F}})$. |

The forces applied to the humerus cause it to move to a position of mechanical equilibrium, $\overline{\boldsymbol{g}}_\theta = \boldsymbol{g}_\theta(\overline{\boldsymbol{F}})$, which differs from the initially assumed position, $\boldsymbol{g}_\theta$. This new humeral head position results in a different contact location and induces a new joint reaction moment, $\overline{\boldsymbol{m}}_a = \boldsymbol{m}_a(\overline{\boldsymbol{F}})$, which also deviates from the initially estimated joint reaction moment, $\boldsymbol{m}_e$. To achieve an optimal solution, an additional iterative procedure takes place. In this approach, an optimal solution is attained when the difference between the joint reaction moment $\overline{\boldsymbol{m}}_a$ obtained from the FE model in the **Module Simulation** and the estimated joint reaction moment $\boldsymbol{m}_e$ utilized in the RB model in **Module Muscle Forces** is close enough to zero, *i.e.*, $\frac{\|\boldsymbol{m}_e - \overline{\boldsymbol{m}}_a\|}{\|\boldsymbol{m}_e\|} < tol_m$ for $tol_m = 10^{-6}$. This condition signifies a close alignment between the outcomes of the finite element and rigid body models, indicating that an optimal solution has been reached. If $\|\boldsymbol{m}_e - \overline{\boldsymbol{m}}_a\| > tol_m$, another iteration begins from which the estimated joint reaction moment $\boldsymbol{m}_e$ is updated to $\boldsymbol{m}_e^n = \overline{\boldsymbol{m}}_a^{n-1}$ and the position of the humerus $\boldsymbol{g}_\theta$ is updated to $\boldsymbol{g}_\theta^n = \overline{\boldsymbol{g}}_\theta^{n-1}$.

Table 9 – Simulation Framework.

**Module Shoulder Abduction**

$[\boldsymbol{g}_\theta^0] = humerus\_rotation(\theta)$

$n = 1$

$while\ \frac{\|\boldsymbol{m}_e^n - \overline{\boldsymbol{m}}_a^n\|}{\|\boldsymbol{m}_e^n\|} > tol_m$

**Module Muscle Path**

$\boldsymbol{g}_\theta^n = \overline{\boldsymbol{g}}_\theta^{n-1}$

$\left[\boldsymbol{d}_m^n, \boldsymbol{x}_m^n, \boldsymbol{d}_p^n, \boldsymbol{x}_p^n\right] = muscle\_path(\boldsymbol{g}_\theta^n)$

**Module Muscle Forces**

$k = 1$

$R_c^{n,k=1} = R_c^{n,0} = 1500\ N$

$\boldsymbol{F}_{init}^{n,k=1} = \boldsymbol{F}_{init}^{n,0} = \overline{\boldsymbol{F}}^{n-1}$

$\boldsymbol{m}_e^n = \overline{\boldsymbol{m}}_a^{n-1}$

**Load Sharing Problem**

$while\ \varepsilon^{n,k} < tol_\varepsilon$

$R_c^{n,k} = B\left\|\boldsymbol{r}_a^{n,k-1}\right\|, B = 0.975$

$\boldsymbol{F}_{init}^{n,k} = \boldsymbol{F}^{n,k-1}$

$[\boldsymbol{F}^{n,k}] = LSP(C_x, C_y, \boldsymbol{F}^{max}, \boldsymbol{d}_m^n, \boldsymbol{x}_m^n, \boldsymbol{d}_p^n, \boldsymbol{x}_p^n, P, \boldsymbol{F}_{init}^{n,k}, R_c^{n,k}, \boldsymbol{m}_e^n)$

$\boldsymbol{f}_m^{n,k} = \boldsymbol{f}_m^{n,k}(\boldsymbol{F}^{n,k})$

$\boldsymbol{r}_a^{n,k} = \boldsymbol{r}_a^{n,k}(\boldsymbol{F}^{n,k})$

$\varepsilon^{n,k} = \varepsilon^{n,k}(\boldsymbol{F}^{n,k})$

$k = k + 1$

$end$

$\overline{\boldsymbol{F}}^n = \boldsymbol{F}^{n,K-1}$

$\overline{\boldsymbol{f}}_m^n = \boldsymbol{f}_m^{n,K-1}$

$\overline{\boldsymbol{r}}_a^n = \boldsymbol{r}_a^{n,K-1}$

$\bar{\varepsilon}^n = \varepsilon^{n,K-1}$

**Module FE Simulation**

$[\overline{\boldsymbol{m}}_a^n, \overline{\boldsymbol{g}}_\theta^n] = FE\_simulation(\overline{\boldsymbol{f}}_m^n, \boldsymbol{p}, \boldsymbol{g}_\theta^n)$

$n = n + 1$

$end$

The Simulation Framework's overall operation is presented in Table 9 and illustrated. The functions are presented as $[output] = function(input)$. Building on the summary of the Simulation Framework presented earlier, a detailed explanation of the **Module Muscle Forces** can now be provided. As shown in Table 9, the **Module Muscle Forces** operates as an iterative procedure nested within another iterative procedure, which will be referred to as **iterative procedure K** and **iterative procedure** $\boldsymbol{n}$, respectively. Within **Module Muscle Forces**, the constraint $R_c$ is progressively reduced based on the joint reaction force amplitude $\left\|\boldsymbol{r}_a^{n,k-1}\right\|$ solution from the previous iteration $k$, multiplied by a reduction coefficient $B$. In the first iteration of iterative procedure $k$ $(k = 1)$, $\|\boldsymbol{r}_a^{n,k=1}\|$ is equal to $1500\,N$, which is sufficiently large for the purposes of the Simulation Framework. To ensure the effective reduction of $R_c$, the coefficient $B$ must be less than 1. In this study, $B = 0.975$ was selected, as it consistently produced satisfactory results.

The genetic optimization algorithm used to solve the load-sharing problem (LSP) utilizes a previously identified solution set of muscle forces as its initial population. For iterative procedure $k$, the initial population is defined as $\boldsymbol{F}_{init}^{n,k} = \boldsymbol{F}^{n,k-1}$. When $k = 1$, the initial population becomes $\boldsymbol{F}_{init}^{n,k=1} = \overline{\boldsymbol{F}}^{n-1}$, where $\overline{\boldsymbol{F}}^{n-1}$ is the solution set of muscle forces amplitudes of the previous iterative procedure n. If $n = 1$, a random set of muscle forces is selected as initial population. Additionally, to correctly solve the LSP, an estimated joint reaction moment must be provided, defined as $\boldsymbol{m}_e^n = \overline{\boldsymbol{m}}_a^{n-1}$, where $\overline{\boldsymbol{m}}_a^{n-1}$ is the joint reaction moment obtained from the solution of the previous iterative procedure $n$. If $n = 1$, the estimated joint reaction moment is $\boldsymbol{m}_e^{n=1} = [0\ 0\ 0]$, based on the assumption that the joint is a ball joint and the resultant force acting on the joint passes through the joint rotation center, thus generating no moment.

## 4.5 ANTERIOR OSSEOUS DEFECTS

Anterior glenoid osseous defects were created at the 3 o'clock position, following the procedure presented by YAMAMOTO, N. *et al.* (2009). Osteotomy lines were created at 2 mm, 3 mm, 4 mm, 5 mm, and 6 mm from the 0 mm osteotomy line, as illustrated in Figure 37. The 0 mm osteotomy line is the most anterior vertical line tangential to the glenoid projection on the glenoid plane and represents a clinical case of a Bankart lesion. The sizes of the osseous defects correspond to 5.67%, 8.51%, 11.34%, 14.18%, and 17.02% of the glenoid length, measuring 35.26 mm and defined as the diameter of the circumference that best fits around the projection of the glenoid on the glenoid plane, while the glenoid width measures 24.34 mm.

Figure 37 – Osteotomy lines in red. The dotted line represents the line by which point M is identified for each osseous defect size.

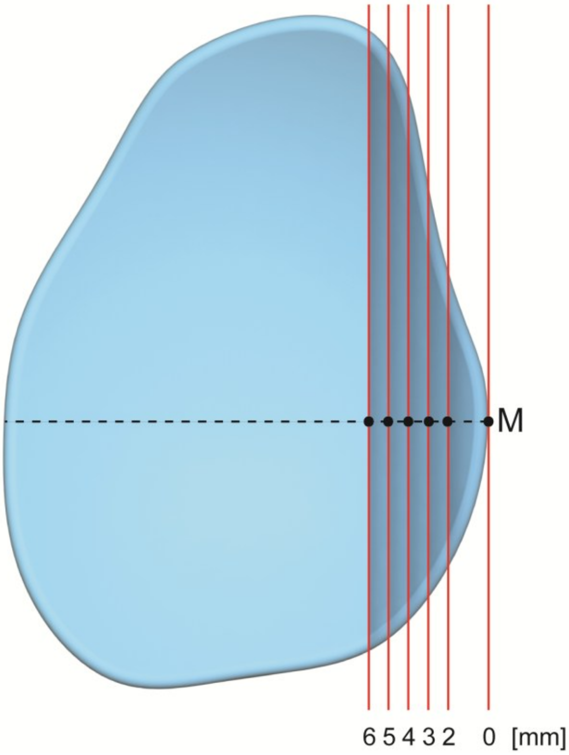


From the author.

The glenoid track concept was used to quantify the influence of the glenoid osseous defects on the contact area onto the humeral head cartilage. The measurement of the glenoid track width was performed as indicated by OMORI *et al.* (2014), albeit with adjustments on the location of certain landmarks. Point C, representing the articular center of the humeral head cartilage, is defined in alignment with OMORI *et al.*'s specifications, as illustrated in Figure 38. However, Point M, which OMORI *et al*. identify at the intersection of the medial-lateral line and the anterior glenoid rim, is instead defined in this study as the most anterior point of the glenoid surface, as shown in Figure 37. Additionally, the medial footprint of the rotator cuff is estimated using a plane derived from MRI images, and is set perpendicular to the humeral anatomical neck, represented as the green plane in Figure 38. The calculation of glenoid track width for each abduction angle and osseous defect size involves measuring the distance of line MT from the projection of point M onto the humeral head cartilage to point T on the plane that simulates the medial margin of the rotator cuff following the articular curve of the humeral head cartilage.

Figure 38 – Landmarks used to compute the glenoid track width at abduction angles of 60°, 90° and 120°.

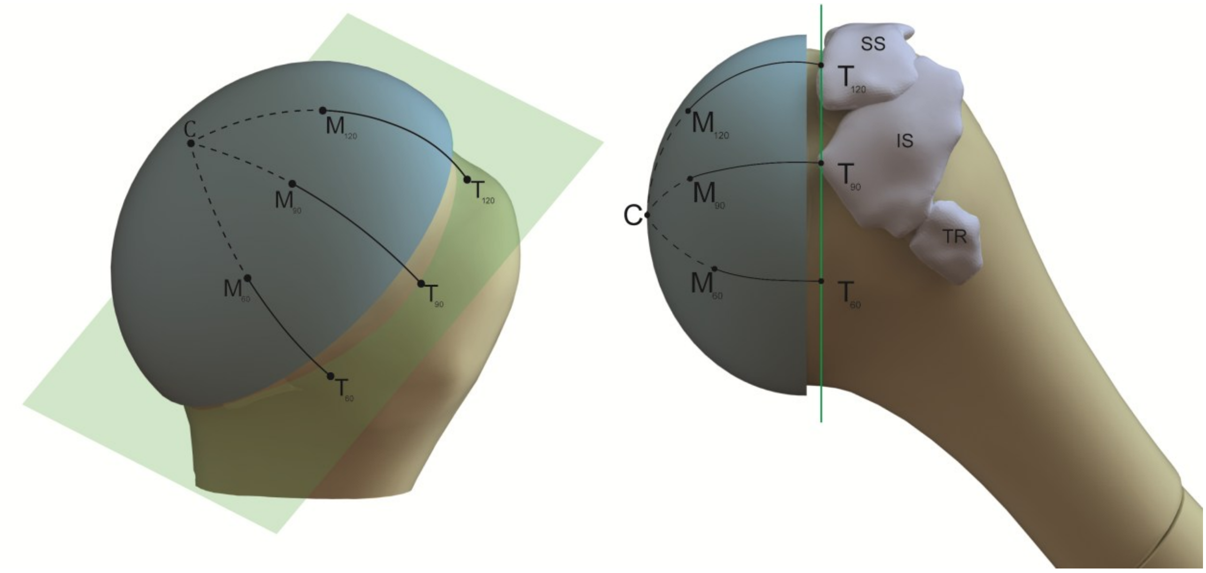


From the author.

# 5 SENSITIVITY ANALYSIS

To better understand the impact of arm weight on joint reaction force and humeral head translations, a sensitivity analysis was conducted. Simulations were performed at abduction angles of 30°, 45°, 60°, 75°, 90°, 105°, and 120°, considering arm weights of 35 N, 40 N, 45 N, and 50 N. A one-sample t-test was used to statistically compare the mean percentage increase in joint reaction force to the percentage increase in arm weight, with the null hypothesis that both values are equal. A significance level of $\alpha = 0.05$ was chosen for the two-tailed test, and with 6 degrees of freedom (7 samples), the critical t-value was 2.447. Humeral head translations were analyzed using the center of the humeral head as a reference in each abduction position, employing the minimum bounding sphere technique (RITTER, 1990; WELZL, 1991) to assess result dispersion. This technique calculates the center and diameter of the smallest sphere containing all data points. The analysis was performed for abduction angles from 30° to 90° and from 30° to 120° to evaluate the impact of arm elevation beyond 90° abduction.

## 5.1 RESULTS AND DISCUSSION

The joint reaction force increased proportionally with the rise in arm weight amplitude (Figure 39). Table 10 presents the joint reaction forces obtained for each case, while Table 11 details the corresponding percentage increases in relation to P = 35 N. Joint reaction forces are greatest in 90° abduction in all cases, corresponding to 92.83%, 110.27%, 125.86%, and 150.22% of body weight (70 kg). For arm weights of 40 N, 45 N, and 50 N, the mean percentual increase in joint reaction force was 16.86 % (SD 4.92 %), 36.29 % (SD 4.94 %), and 53.00 % (SD 10.72 %), respectively. For P = 40 N, there was no significant difference between the percentage increase in arm weight and the mean percentage increase in joint reaction force (t-value = 1.386 < 2.447). However, for P = 45 N (t-value = 3.804 > 2.447) and P = 50 N (t-value = 2.687 > 2.447), the mean percentual increase in joint reaction force was statistically greater than the percentual increase in arm weight amplitude. It is worth noting that if the significance level $\alpha$ is adjusted to 0.01, the critical t-value increases to 3.707. Under this stricter threshold, only the case where P = 45 N shows a marginally significant difference.

It has been observed that an increase in the amplitude of the joint reaction force also increases its compressive component, $r_a(z)$. As demonstrated in APPENDIX B, a rise in the compressive component leads to a decrease in the critical value of the glenohumeral ratio, thereby reducing the design space $\boldsymbol{\Omega}$. This reduction in the glenohumeral ratio forces the joint reaction force toward the center of the glenoid cartilage, further increasing the compressive component (as discussed in Chapter 7). This feedback loop continues to influence the glenohumeral ratio. Although this mechanism is self-limiting, it may explain the discrepancies between the percentage increases in arm weight and joint reaction force.

Figure 39 – Joint reaction force as a function of the arm weight amplitude.

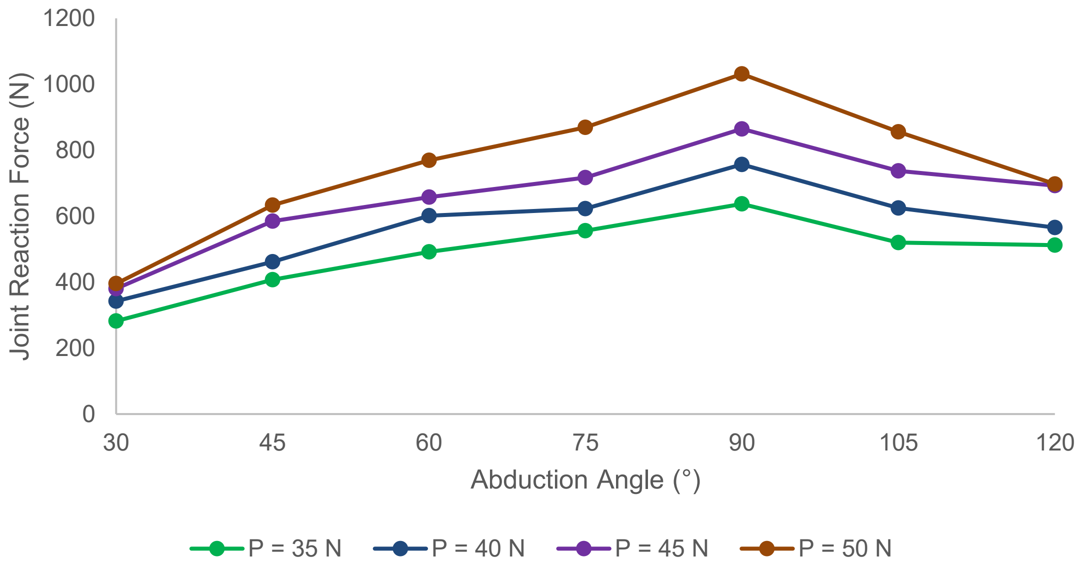


From the author.

Table 10 – Joint reaction force as a function of the arm weight amplitude.

| | **Joint reaction force (N)** | | | | | | |
|---|---|---|---|---|---|---|---|
| **Arm weight amplitude** | **30°** | **45°** | **60°** | **75°** | **90°** | **105°** | **120°** |
| P = 35 N | 281,96 | 407,52 | 491,73 | 556,20 | 637,23 | 520,11 | 512,45 |
| P = 40 N | 342,37 | 461,34 | 601,08 | 622,45 | 756,95 | 624,90 | 565,27 |
| P = 45 N | 380,28 | 585,03 | 658,28 | 717,17 | 864,95 | 737,52 | 693,09 |
| P = 50 N | 395,34 | 633,96 | 769,03 | 869,49 | 1031,25 | 855,89 | 697,51 |

Table 11 – Percentual increase in joint reaction force for arm weight amplitude equal to 40 N, 45 N, and 50 N, including mean value, variance and t value.

| | P = 40 N | P = 45 N | P = 50 N |
|---|---|---|---|
| **Arm weight increase** | 14,29% | 28,57% | 42,86% |
| **30°** | 21,43% | 34,87% | 40,21% |
| **45°** | 13,21% | 43,56% | 55,57% |
| **60°** | 22,24% | 33,87% | 56,39% |
| **75°** | 11,91% | 28,94% | 56,33% |
| **90°** | 18,79% | 35,74% | 61,83% |
| **105°** | 20,15% | 41,80% | 64,56% |
| **120°** | 10,31% | 35,25% | 36,11% |
| **Mean** | 16,86% | 36,29% | 53,00% |
| **SD** | 4.92% | 4.94% | 10.72% |
| **t-value** | 1.386 | 3.804 | 2.687 |

Starting from 30°, in all cases, humeral head translations followed the same pattern, moving slightly posterior up to 90° and inferior up to 120°. The center of the humeral head remained in the posterior and inferior region of the glenoid cartilage when observed from the glenoid plane, near the center of the coordinate system (Figure 40). Using the minimum bounding sphere technique, the diameter and center of the smallest sphere enclosing all humeral head centers were determined for each arm weight. For abduction motion from 30° to 120°, the largest minimum bounding sphere had a diameter of 2.808 mm (Table 12). When considering abduction from 30° to 90°, the largest sphere had a diameter of 1.758 mm (Table 13), showing how humeral head translations increase after 90° abduction. Figure 41 illustrates the size and location of these minimum bounding spheres relative to the glenoid cartilage, showing how the spheres overlap. This overlap indicates low dispersion in humeral head translations across all arm weight values.

Table 12 – Center coordinates, diameters and distances from the origin of the coordinate system of the minimum boundary spheres considering abduction from 30° to 120°.

| Abduction 30° - 120° | | | | | |
|---|---|---|---|---|---|
| **Case** | **X (mm)** | **Y (mm)** | **Z (mm)** | **Distance from origin (mm)** | **Diameter (mm)** |
| P = 35 N | 2.1067 | -1.6047 | 1.8706 | 3.2423 | 2.6136 |
| P = 40 N | 2.0304 | -1.6057 | 1.9278 | 3.2276 | 2.6056 |
| P = 45 N | 2.1161 | -1.5501 | 1.9717 | 3.2815 | 2.8074 |
| P = 50 N | 1.9858 | -1.2830 | 1.9936 | 3.0926 | 2.4402 |

Figure 40 – Humeral head translations for different values of arm weight $P$ project onto the glenoid plane. The cross in the illustration represents the origin of the coordinate system.

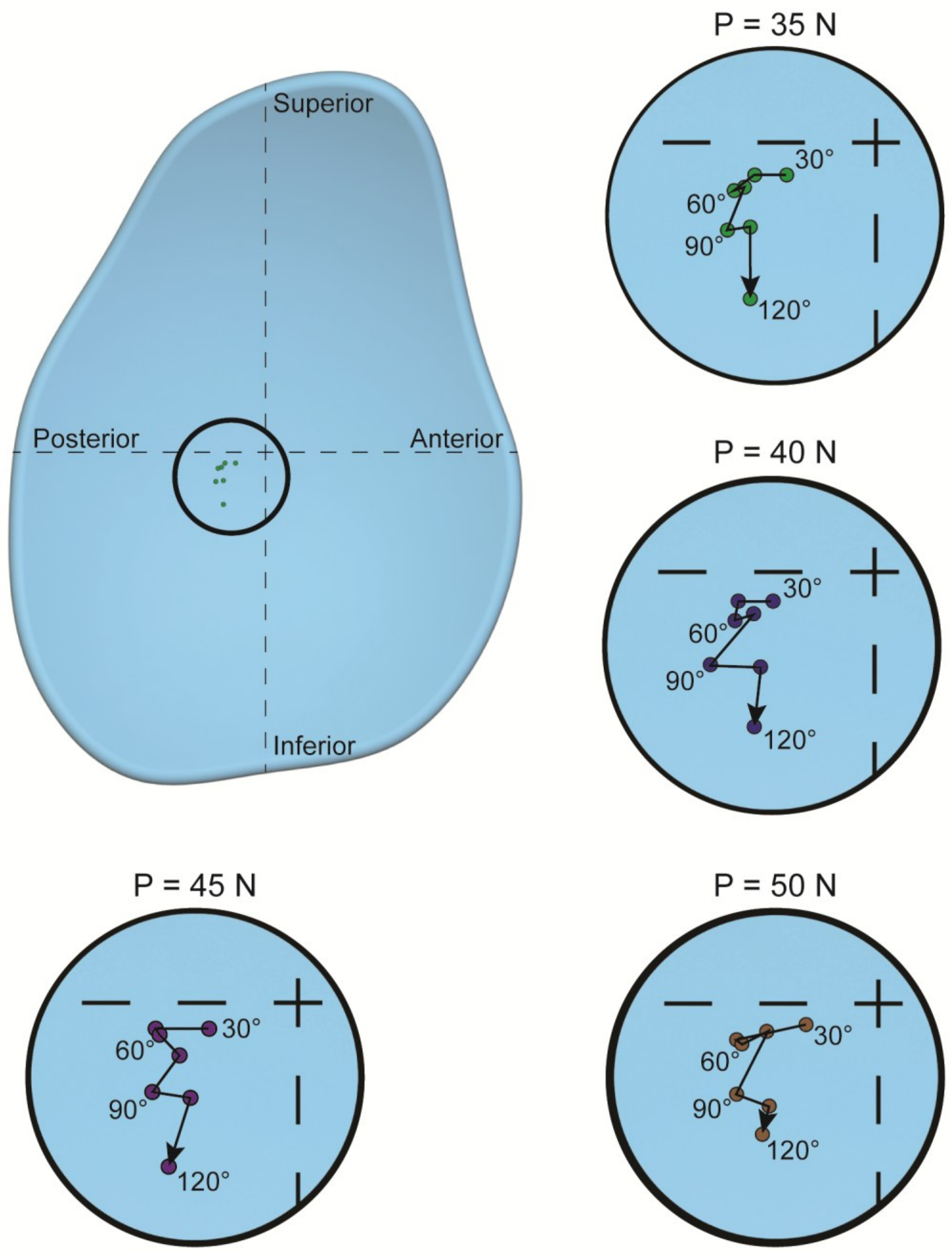


From the author.

Table 13 – Center coordinates, diameters and distances from the origin of the coordinate system of the minimum boundary spheres considering abduction from 30° to 90°.

| Case | X (mm) | Y (mm) | Z (mm) | Distance from origin (mm) | Diameter (mm) |
|---|---|---|---|---|---|
| **Abduction 30° - 90°** | | | | | |
| P = 35 N | 1.8848 | -0.7956 | 2.1817 | 2.9909 | 1.5140 |
| P = 40 N | 2.0314 | -0.9033 | 2.1579 | 3.0982 | 1.5706 |
| P = 45 N | 1.9017 | -0.7624 | 2.2299 | 3.0283 | 1.5666 |
| P = 50 N | 1.8038 | -0.7711 | 2.2355 | 2.9742 | 1.7588 |

Figure 41 – Minimum bounding spheres for abduction up to 90° (left) and up to 120° (right).

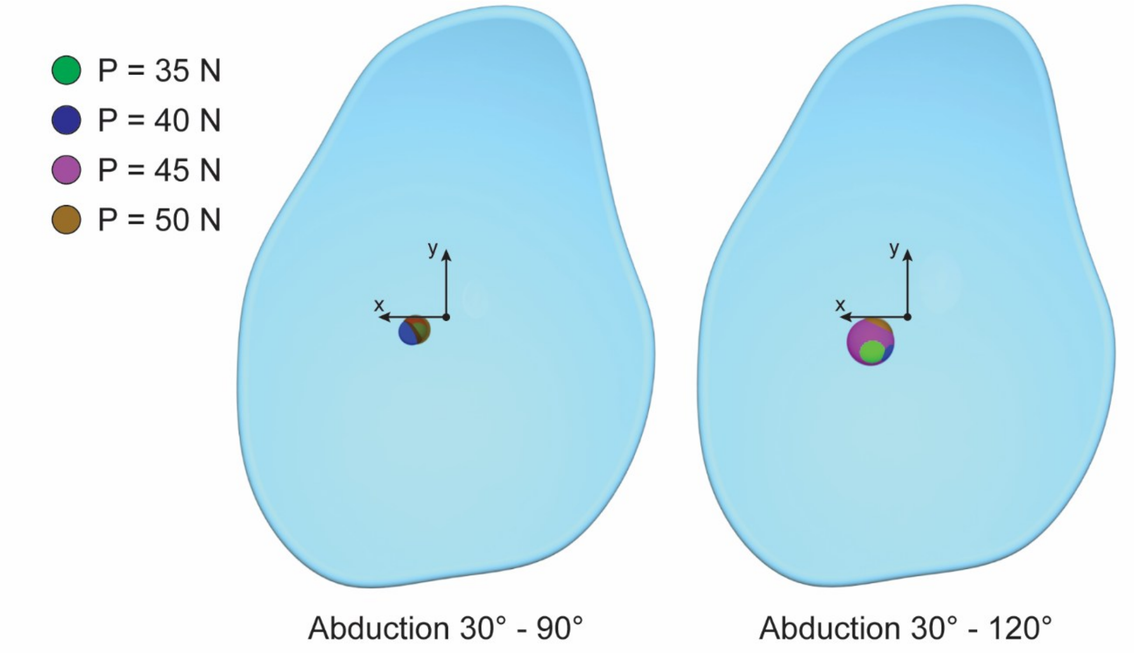


From the author.

# 6 RESULTS

In this research, whenever stability was successfully attained (Table 14), the values of the relative residual moment were consistently below $10^{-8}$. Specifically, for defects measuring 3 mm and 4 mm, stability was maintained up to an abduction angle of 105°. However, for larger defects of 5 mm and 6 mm, stability could only be achieved at abduction angles of 30° and 45°. In instances where stability was not attained, the relative residual moment exceeded the established tolerance of $10^{-6}$.

Table 14 – Joint stability. “OK” means that stability was achieved. “NOT OK” means otherwise.

| Osseous Defect | 30° | 45° | 60° | 75° | 90° | 105° | 120° |
|---|---|---|---|---|---|---|---|
| 0 mm | OK | OK | OK | OK | OK | OK | OK |
| 2 mm | OK | OK | OK | OK | OK | OK | OK |
| 3 mm | OK | OK | OK | OK | OK | OK | NOT OK |
| 4 mm | OK | OK | OK | OK | OK | OK | NOT OK |
| 5 mm | OK | OK | NOT OK | NOT OK | NOT OK | NOT OK | NOT OK |
| 6 mm | OK | OK | NOT OK | NOT OK | NOT OK | NOT OK | NOT OK |

The abduction position has a significant impact on the predicted joint reaction forces, with values increasing up to 90° abduction and then exhibiting a declining trend, as shown in Figure 42. Moreover, the size of the bone defect appears to influence the joint reaction force, with indications that larger defects may be associated with higher joint reaction force values, especially in higher abduction positions. The variability in the data suggests that this relationship may vary among different abduction positions, as in 30° and 45° abduction. The peak joint reaction force for defect sizes of 0 mm, 2 mm, 3 mm, and 4 mm are, respectively, 637.23 N, 687.14 N, 773.93 N, and 901.30 N. These values represent 92.83 %, 100.10 %, 112.74 %, and 131.29 % of the subject’s body weight, respectively.

The force exerted by the supraspinatus muscle shows great variability across abduction angles and osseous defect sizes (Figure 43). For defect sizes 0 mm and 2 mm, there is an increase of muscle force from 45° to 90° of abduction, while for defect size 3 mm this increase ends in 75°. This trend is not repeated when the defect size is 4 mm, where there is a peak of muscle force in 90° of abduction. The subscapularis muscle presents the same trend for all sizes of osseous defects: the force exerted by the subscapularis increases up to 90° followed by a slight fall on subsequent angles.

Furthermore, Figure 44 shows an increase in muscle force from 60° of abduction with the enlargement of the size of the osseous defect.

Figure 42 – Joint reaction force along the abduction movement for osseous defects measuring 0 mm, 2 mm, 3 mm, and 4 mm.

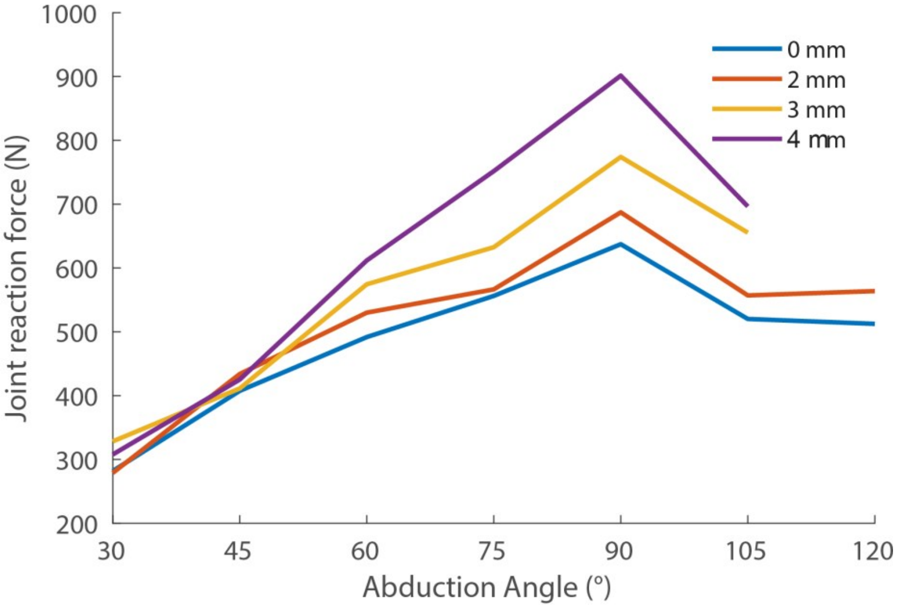


From the author.

Figure 43 – Force exerted by the supraspinatus muscle along the abduction movement for all sizes of osseous defects.

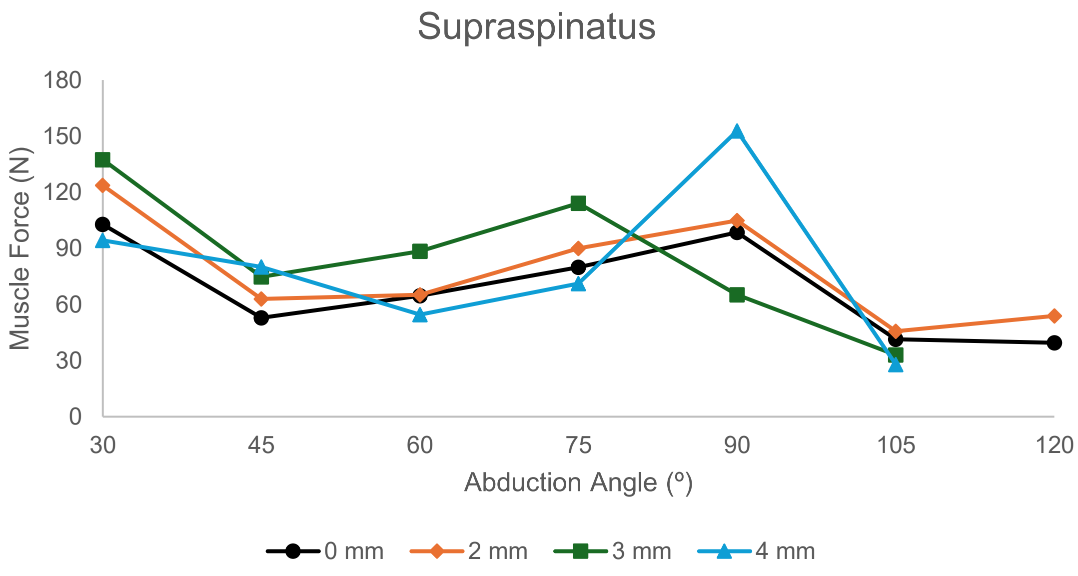


From the author.

Figure 44 – Force exerted by the subscapularis muscle along the abduction movement for all sizes of osseous defects.

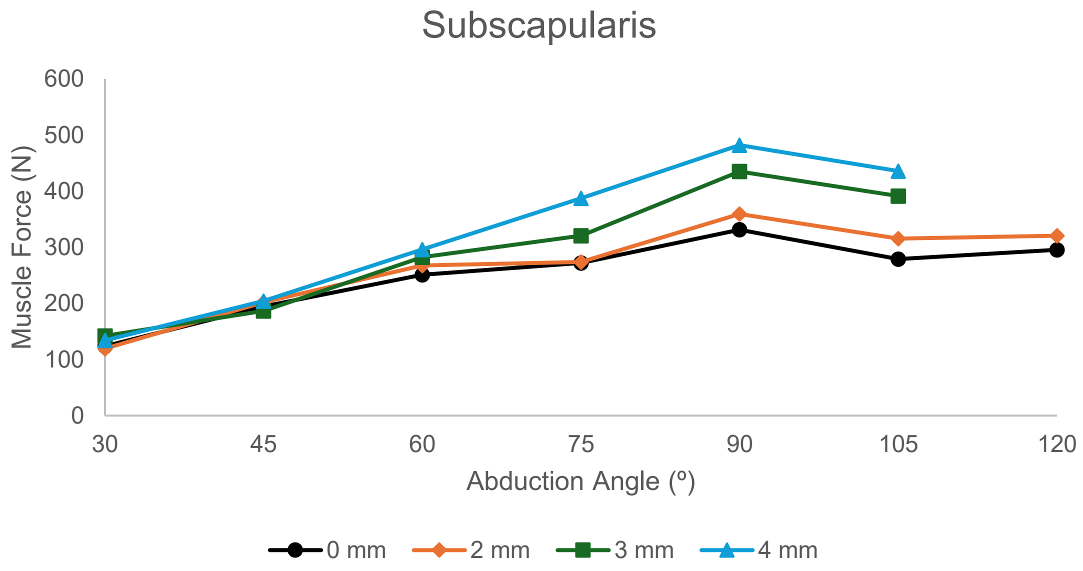


From the author.

With a similar tendency to the subscapularis muscle, the force exerted by the infraspinatus increases up to 60° of abduction and decreases at the following angles for all sizes of osseous defects. From 60° of abduction, it is observed in Figure 45 that there is an increase in muscle force along with an increase in the osseous defect. For all sizes of osseous defect, the force exerted by the intermediate segment of the deltoid increases up to 60° of abduction followed by a reduction until the end of the movement (Figure 46). From 75° onwards, there is a reduction in muscle force as the size of the osseous defect increases.

The posterior segment of the deltoid muscle starts to act from 60° of abduction for all sizes of osseous defects and the force it exerts increases up to 105° of abduction, as presented in Figure 47. Although there is a certain variability in defects sized 0 mm and 2 mm, the muscle force generally increases with the enlargement of the osseous defect. While the teres minor muscle and the posterior segment of the deltoid played a role in joint stabilization, their muscle forces were very small compared to the other muscles. In all cases, as depicted in Figure 48, Figure 49, Figure 50, and Figure 51, the supraspinatus muscle is the one that exerts the greatest force along the abduction movement, followed by the intermediate segment of the deltoid.

Figure 45 – Force exerted by the infraspinatus muscle along the abduction movement for all sizes of osseous defects.

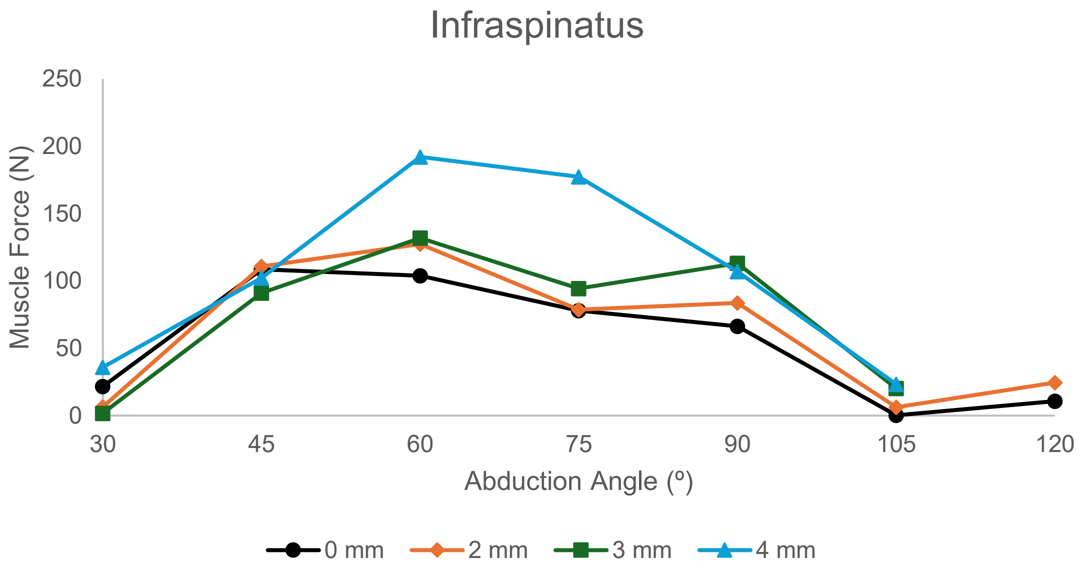


From the author.

Figure 46 – Force exerted by the intermediate segment of the deltoid muscle along the abduction movement for all sizes of osseous defects.

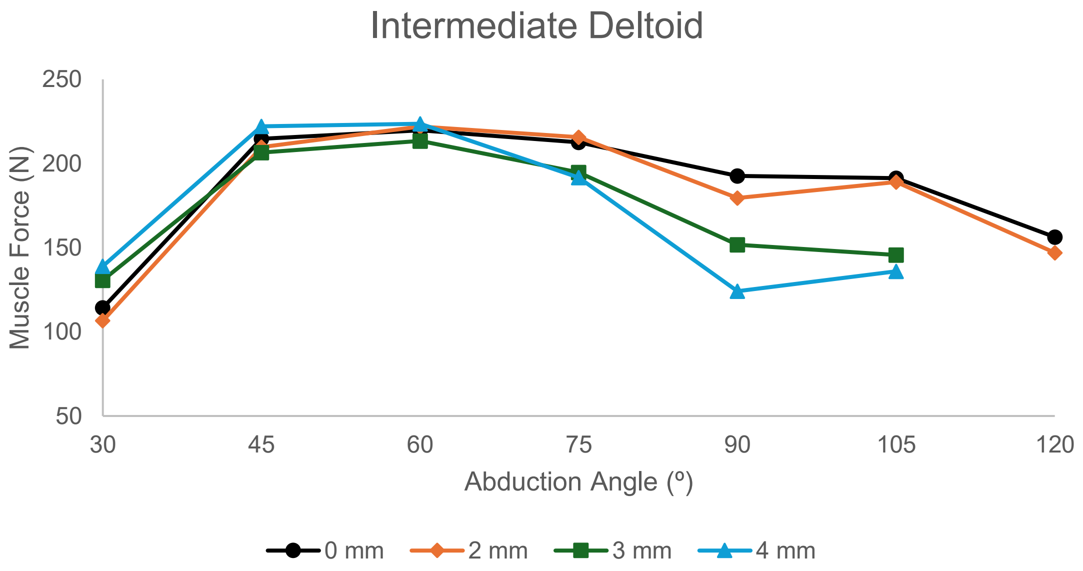


From the author.

Figure 47 – Force exerted by the posterior segment of the deltoid muscle along the abduction movement for all sizes of osseous defects.

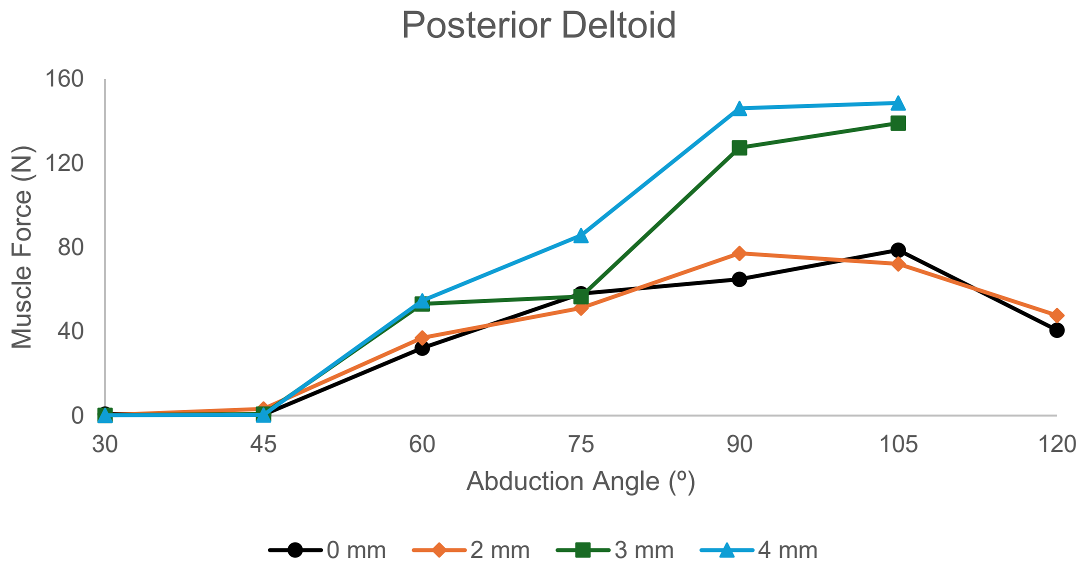


From the author.

Figure 48 – Muscle forces along the abduction movement for osseous defect sized 0 mm.

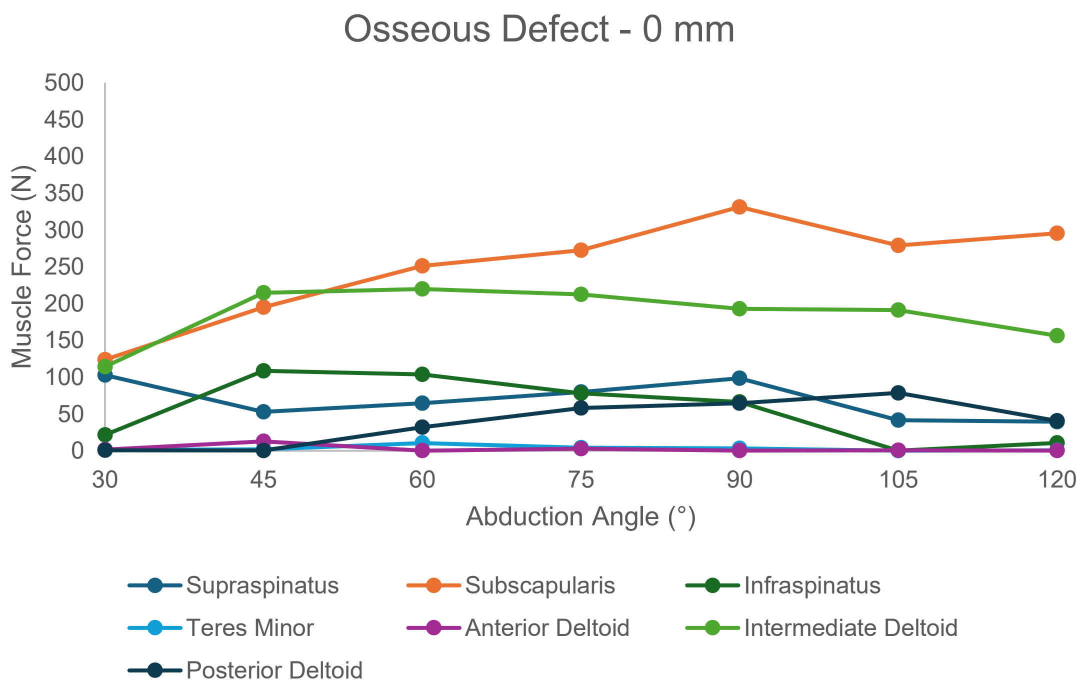


From the author.

Figure 49 – Muscle forces along the abduction movement for osseous defect sized 2 mm.

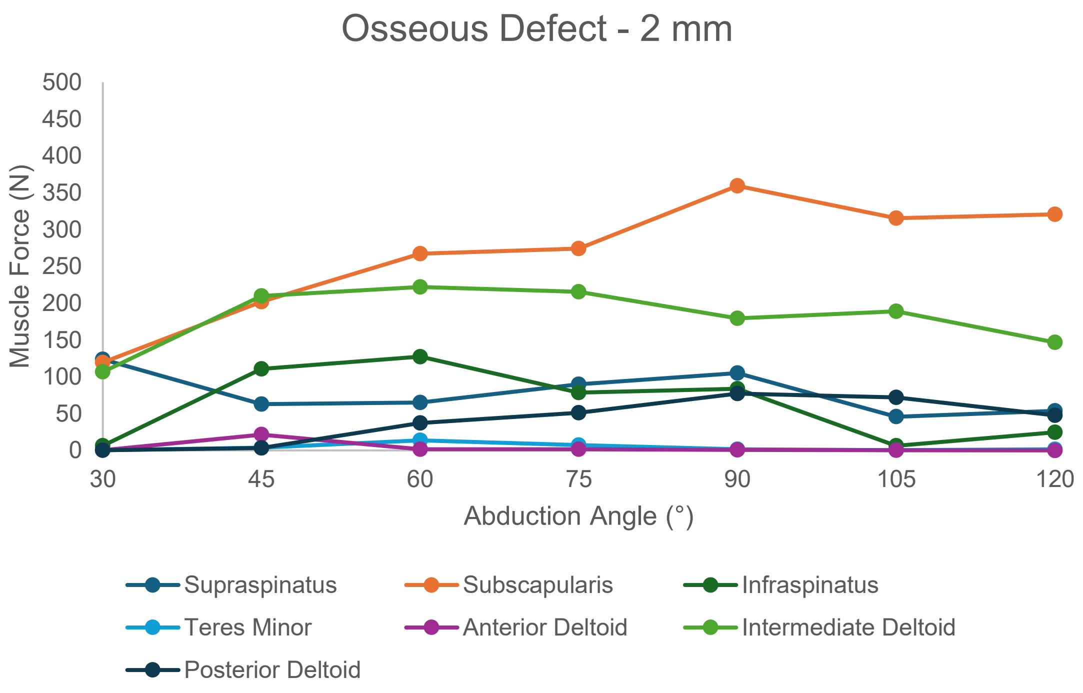


From the author.

Figure 50 – Muscle forces along the abduction movement for osseous defect sized 3 mm.

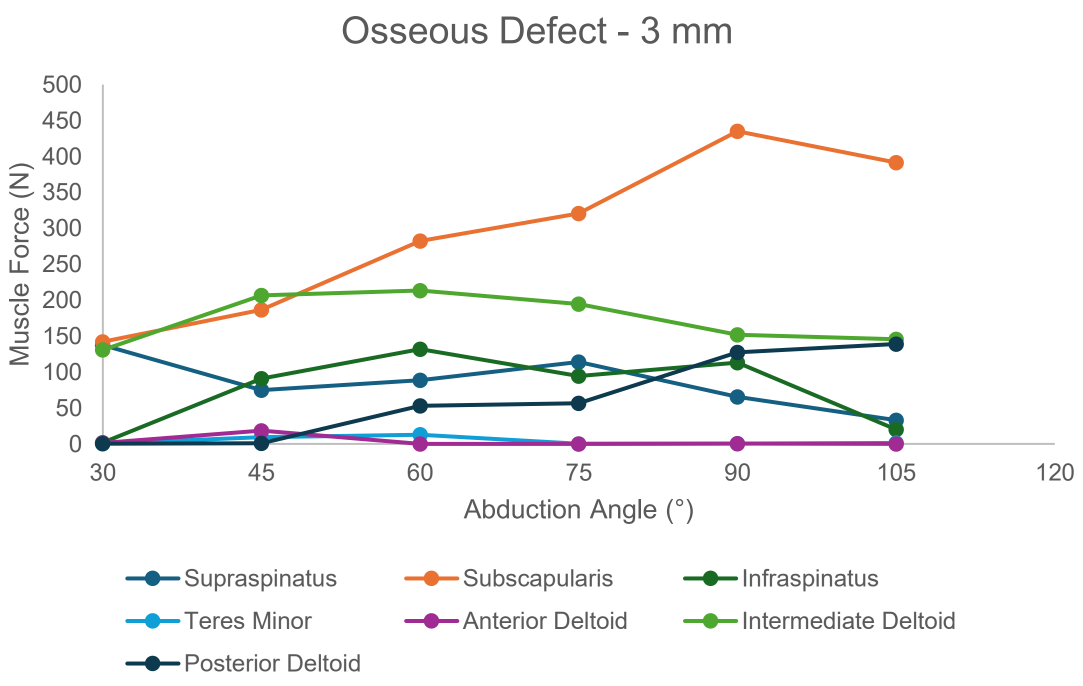


From the author.

Figure 51 – Muscle forces along the abduction movement for osseous defect sized 4 mm.

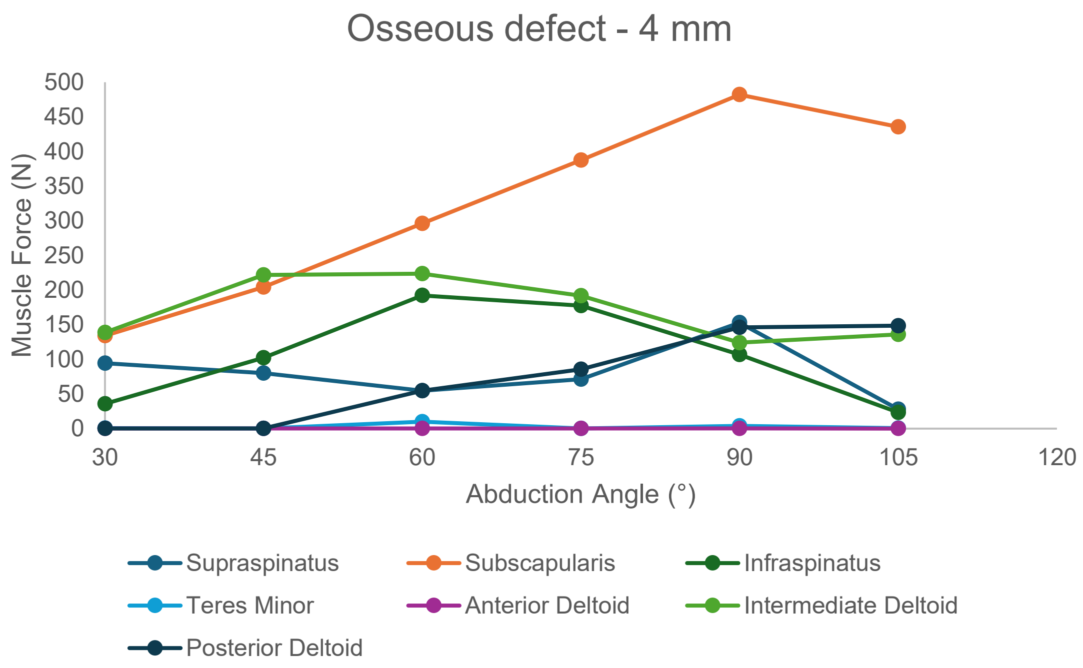


From the author.

Figure 52 and Figure 53 illustrate the distribution of contact pressure along the abduction movement on the articular surfaces of the glenoid cartilage and humeral head cartilage, respectively. In every scenario, the peak of contact pressure is noted around 75° or 90°, with values rising alongside the increase in osseous defect size, mirroring the trend observed in the joint reaction force. The geometric location of the peak contact pressure and the centroid of the contact area predominantly reside in the anterior segment of the glenoid, transitioning from the superior to the inferior portion as abduction increases, across all osseous defects analyzed. Table 15 presents the contact area for all abduction angles and osseous defects sizes.

Table 15 – Contact area for all abduction angles and osseous defect sizes.

| | **Contact area (mm²)** | | | | | | |
|---|---|---|---|---|---|---|---|
| **Osseous defect size** | **30** | **45** | **60** | **75** | **90** | **105** | **120** |
| 0 mm | 277,69 | 306,48 | 337,11 | 359,52 | 397,74 | 338,61 | 325,14 |
| 2 mm | 266,55 | 305,24 | 351,91 | 359,28 | 397,87 | 359,14 | 323,67 |
| 3 mm | 307,87 | 279,74 | 355,18 | 403,68 | 407,78 | 377,88 | --- |
| 4 mm | 272,07 | 306,41 | 360,34 | 421,10 | 392,64 | 369,58 | --- |

Figure 52 – Contact pressure distribution on the glenoid cartilage articular surface for each defect size.

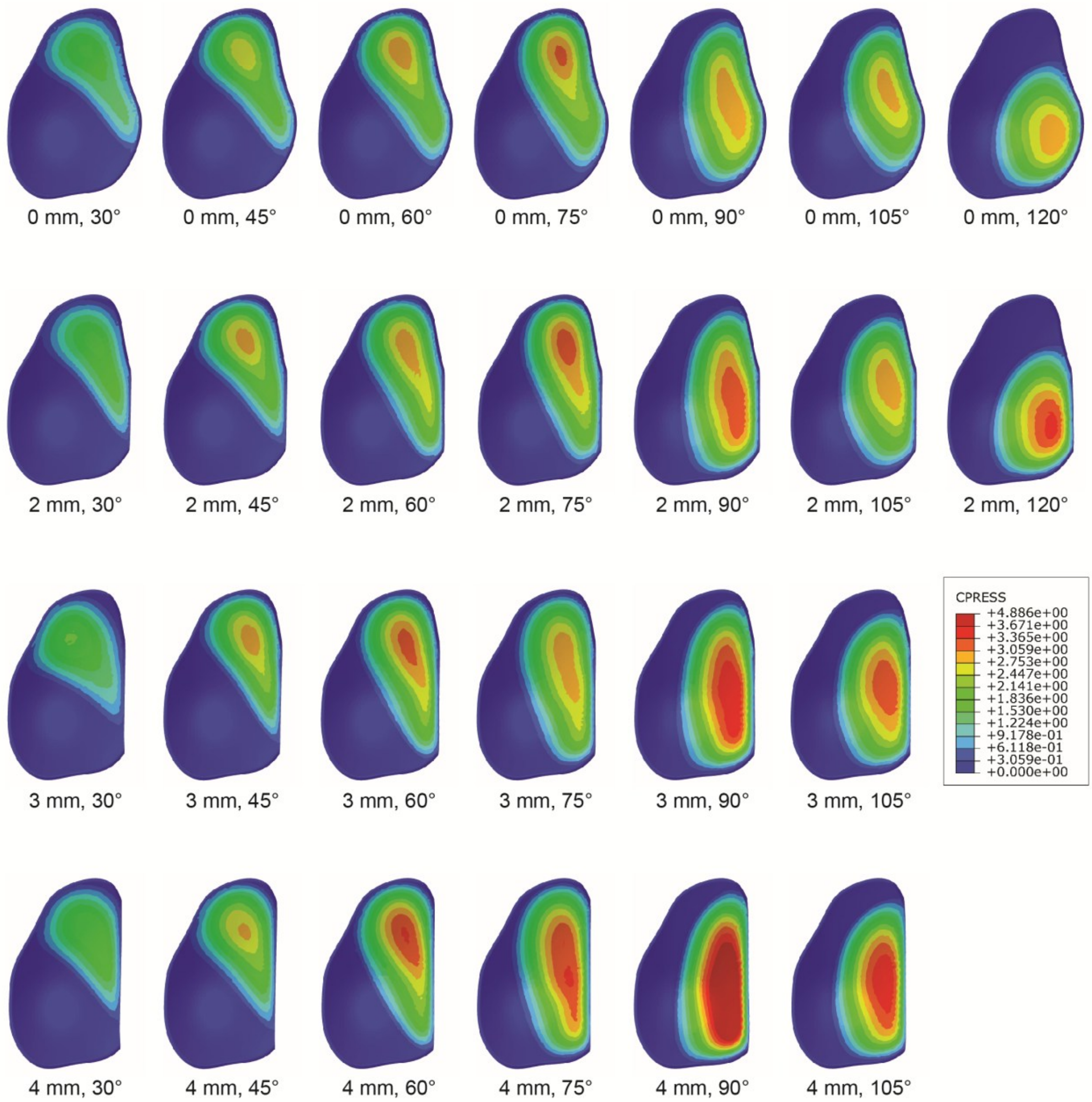


From the author.

Figure 53 – Contact pressure distribution on the humeral head cartilage articular surface for each defect size.

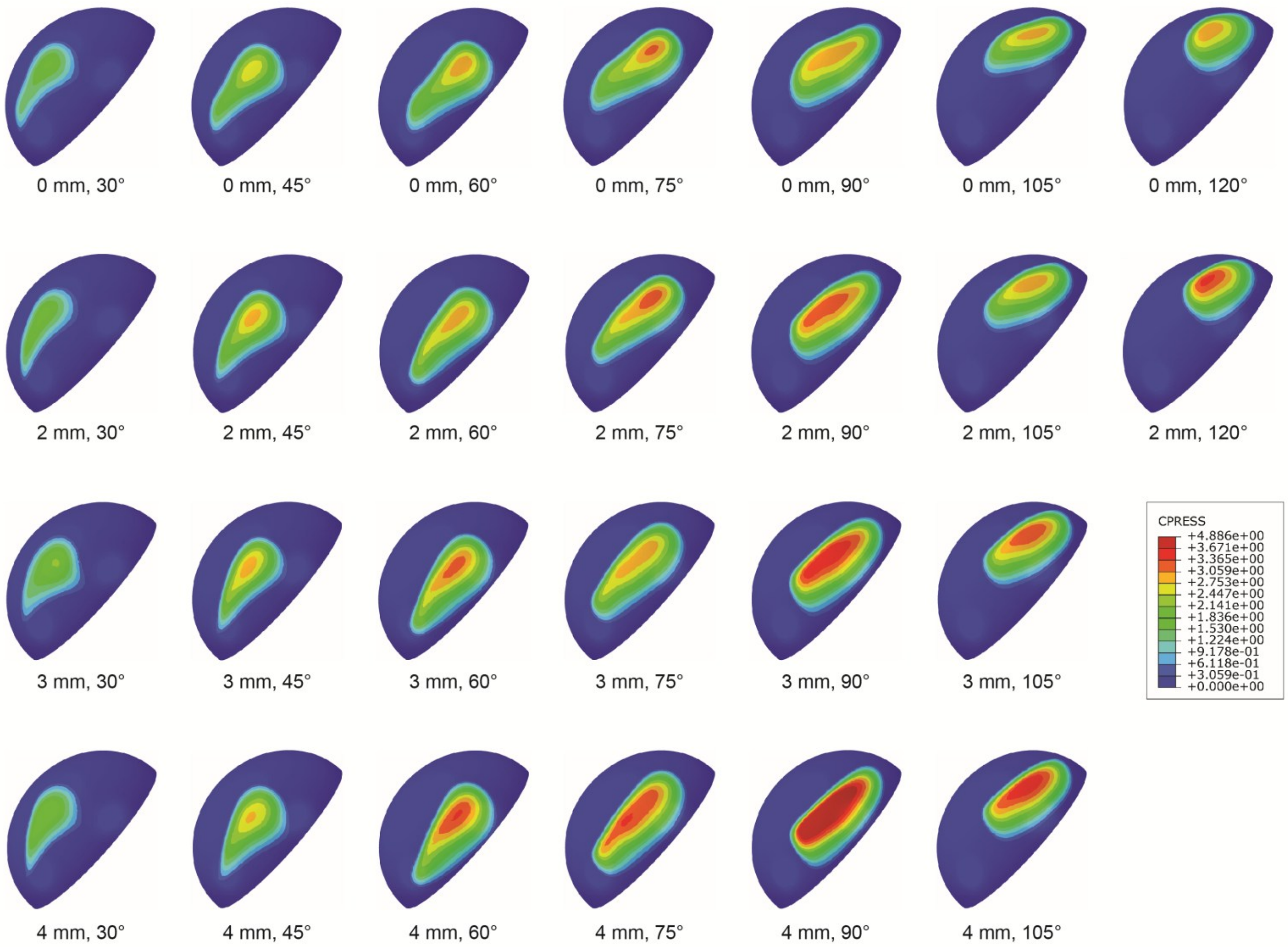


From the author.

On the humeral head cartilage, the contact area remained at the posterior region of the humerus and shifted from inferior to superior as the abduction movement progressed. As shown in Table 16, there is a clear trend of increasing glenoid track width as abduction position increases, suggesting that abduction position has a significant impact on the glenoid track. It is shown in Figure 54 the trajectory of Point M along the abduction movement and for each defect size. In general, the width of the glenoid track tends to decrease as the size of the bone defect increases as the location of Point M tends to move medially. This is evidenced by increasing through values and reduced glenoid track length for larger defects compared to a 0 mm defect.

Table 16 – Glenoid track widths along the abduction movement for each defect size in comparison to the values obtained by OMORI *et al*. (2014).

| | **Glenoid track width in mm (% of glenoid width)** | | | | |
|---|---|---|---|---|---|
| **Defect size** | **60** | **75** | **90** | **105** | **120** |
| 0 mm | 18.04 (74.1%) | 22.38 (91.9%) | 22.72 (93.3%) | 23.84 (97.9%) | 23.31 (95.7%) |
| 2 mm | 16.77 (68.8%) | 21.41 (87.9%) | 20.81 (85.4%) | 22.41 (92%) | 21.5 (88.3%) |
| 3 mm | 15.73 (64.6%) | 20.83 (85.5%) | 20.36 (83.6%) | 21.62 (88.8%) | --- |
| 4 mm | 15.03 (61.7%) | 19.11 (78.5%) | 18.14 (74.5%) | 20.03 (82.2%) | --- |
| OMORI *et al.* (2014) | 20.7 (89%) | --- | 19.4 (83%) | --- | 18.9 (81%) |

Figure 54 – Trajectory of Point M along the abduction movement for defect sizes 0 mm, 2 mm, 3 mm, and 4 mm.

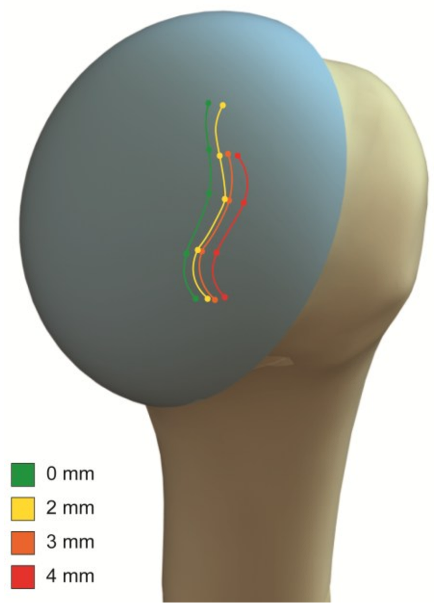


From the author.

The humeral head exhibits a posterior translation that reaches its maximum at 90° abduction for osseous defects measuring 0 mm, 2 mm, and 3 mm. For the osseous defect sized 4 mm, the maximum posterior translation is observed at 60° abduction. Furthermore, there is a general inferior translation of the humeral head center across all cases. The inferior translation reaches its peak at 120° of abduction for defects sized 0 mm and 2 mm, and at 105° for defects sized 3 mm and 4 mm. Using the minimum bounding sphere technique, the diameter and center of the smallest sphere enclosing all humeral head centers were determined for each defect size. When considering abduction from 30° to 90°, the largest sphere had a diameter of 1.676 mm (Table 17). In this case, the impact of greater abduction angles could not be thoroughly investigated since stability was achieved only up to 105° for defects sized 3 mm and 4 mm. Figure 55 illustrates the size and location of these minimum bounding spheres relative to the glenoid cartilage, showing how the spheres overlap. This overlap indicates low dispersion in humeral head translations across all osseous defect sizes. In relation to the glenoid plane, the humeral head center maintains its position within the inferior-posterior quadrant for all cases (Figure 56 and Figure 57), despite the variability in translation patterns.

Table 17 – Center coordinates, diameters and distances from the origin of the coordinate system of the minimum boundary spheres considering abduction from 30° to 90° and all osseous defects sizes.

| Abduction 30° - 90° | | | | | |
|---|---|---|---|---|---|
| **Defect size** | **X (mm)** | **Y (mm)** | **Z (mm)** | **Distance from origin (mm)** | **Diameter (mm)** |
| 0 mm | 1,8848 | -0,7956 | 2,1817 | 2,9909 | 1,5140 |
| 2 mm | 1,6783 | -0,9646 | 2,1791 | 2,9147 | 1,6759 |
| 3 mm | 1,9056 | -1,0796 | 2,3708 | 3,2276 | 1,2859 |
| 4 mm | 1,8045 | -1,0859 | 2,4032 | 3,1954 | 1,6231 |

Figure 55 – Minimum bounding spheres for abduction up to 90° including all osseous defects sizes.

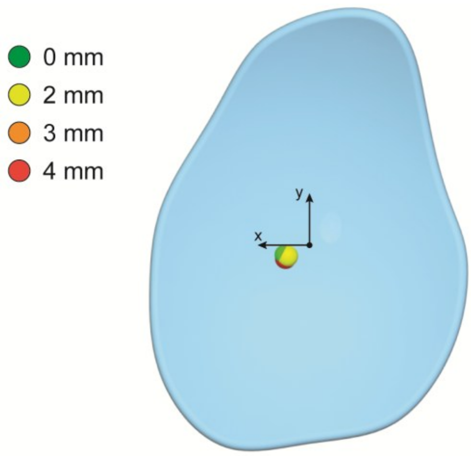


From the author.

Figure 56 – Center of the humeral head projected into the glenoid plane osseous defects sized 0 mm and 2 mm.

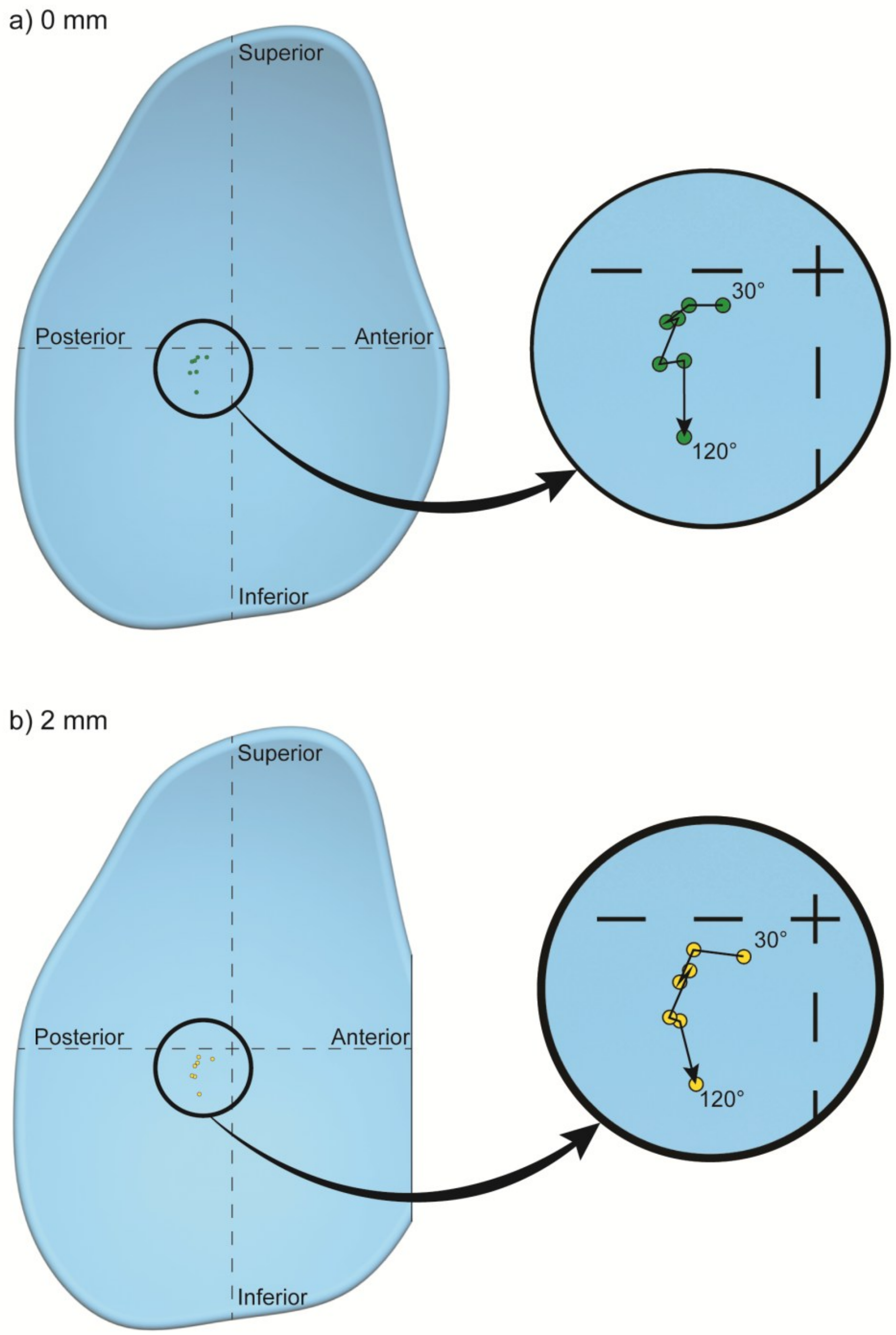


From the author.

Figure 57 – Center of the humeral head projected into the glenoid plane osseous defects sized 3 mm and 4 mm.

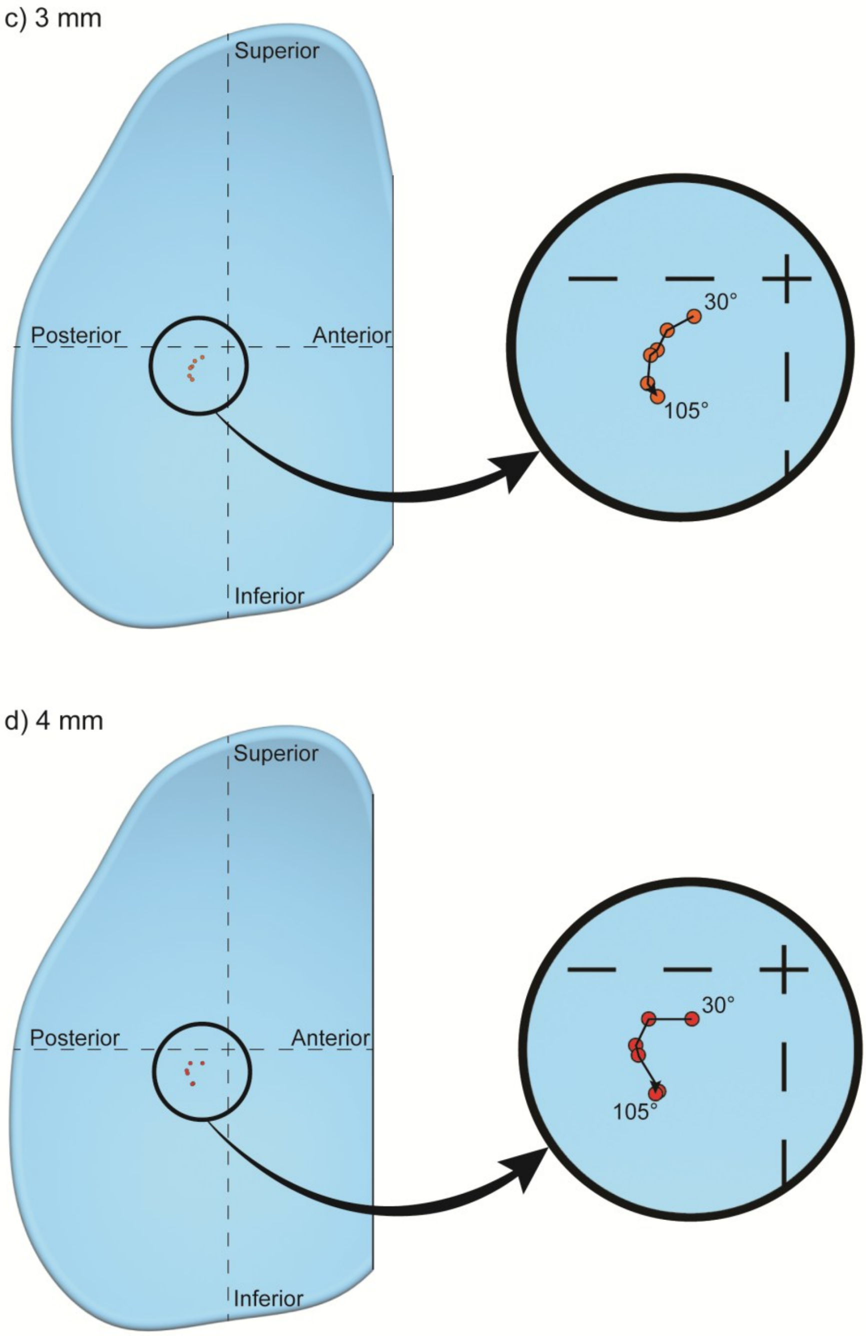


From the author.

# 7 DISCUSSION

The findings of this investigation elucidate the complex biomechanical interactions within the glenohumeral joint in the presence of anterior glenoid osseous defects, offering novel insights into how these defects affect joint stability and contact mechanics along the abduction movement in the coronal plane with the arm externally rotated. Using a computational model, it was possible to infer changes in joint reaction force, muscle forces, contact pressure, contact area, humeral head translations and glenoid track widths. Previous studies have indicated that an osseous defect and a Bankart lesion reduce the capability of the joint to sustain tangential forces acting on the glenoid cartilage due to the absence of anterior stabilizing structures, such as the labrum and glenohumeral ligaments (ITOI *et al.*, 2000; KLEMT *et al.*, 2019; YAMAMOTO, N. *et al.*, 2009, 2010). Mathematically, a bone defect lowers the threshold of tangential forces the glenohumeral joint can endure before dislocating, which, in turn, constricts the design space of admissible solutions for the underdetermined system. For certain abduction angles and osseous defect sizes, this constraint on the admissible solution space means that it may no longer contain feasible solutions that ensure mechanical balance.

The joint reaction force increases in concert with the size of osseous defects, a predictable outcome given the restrictions on admissible tangential forces (Figure 42). In all cases, the joint reaction force follows a trend already observed in other computational studies, where its value increases up to 90° abduction and decreases further along the abduction movement (JUNIOR *et al.*, 2022; SARSHARI *et al.*, 2017; TERRIER *et al.*, 2007). This trend is correlated with the increasing value of the moment generated by the arm weight reaching its peak at 90° abduction; as the external moment decreases, the load exerted by the muscles to achieve equilibrium also decreases, resulting in a lower estimated joint reaction force. However, this behavior contrasts with measurements obtained using an instrumented prosthesis after 90° abduction, which showed a continuous increase in joint contact force (BERGMANN *et al.*, 2007; WESTERHOFF *et al.*, 2009a). It is important to note that these measurements were taken from an elderly patient with a limited range of motion and diagnosed with osteoarthritis, albeit without "serious rotator cuff injuries." This description does not fully rule out the presence of minor injuries that could impact muscle recruitment and force exertion. A previous study reported that the use of a shoulder endoprosthesis alters the scapulohumeral rhythm, resulting in reduced humeral motion and increased scapular motion (DE WILDE; AUDENAERT; BERGHS, 2004). This shift leads to greater muscle force generation due to a less efficient shoulder mechanism and, consequently, to a greater joint reaction force.

The model includes the deltoid muscle, and the rotator cuff muscles divided into 16 individual muscular segments that are modeled as taut strings to represent their biomechanical function. They are the main muscles responsible for joint stability, shoulder abduction and internal/external rotation of the arm. The muscle forces predicted by the model are the minimum forces necessary to ensure mechanical balance, and thus joint stability, in a static position of the arm. The main finding is the force exerted by the subscapularis muscle, which is the greatest in all cases considered. Due to the nature of the analyzed movement, the subscapularis is stretched in all abduction angles, generating a passive force related to the elastic properties of the muscle. The absence of passive joint stabilizers, such as the glenoid labrum, glenohumeral ligaments and joint capsule, along with the restriction that the joint reaction force must point to the glenoid surface, may explain the high force exerted by the subscapularis, as it is the only anterior barrier impeding an anterior luxation of the shoulder. This behavior is in accordance with the theoretical biomechanical advantage of the Latarjet surgery which, by interposing the conjoined tendon after fixing the coracoid graft, potentiates the action of the subscapularis as an anterior stabilizer by creating a sling effect.

This study introduces a novel analysis of joint contact mechanics across different abduction angles and for varying sizes of osseous defects. The increase of the peak contact pressure along the abduction movement corresponds to the increase of the compressive component of the joint reaction force, that presents its maximum value at 90° abduction. Similarly, this tendency is observed with the enlargement of the osseous defect, that, in effect, constrain the admissible tangential forces to lower values, thus intensifying the compressive component. In terms of contact area, a similar trend is noted with abduction angles and defect size; as the resultant compressive force increases, there is a corresponding increase in the contact area. However, the deformable nature of the cartilages and the anterior location of the area’s centroid led to a compaction of the contact area in the anterior region, which may have mitigated the effect of the compressive force. Also, the contact surfaces between the cartilages, defined as non-conforming ellipsoids, introduce a unique shape to the contact area and a certain level of variability to the predicted values.

This study's findings on peak contact pressures and contact areas differ from other computational and *in-vitro* studies, which were mostly performed with the arm in neutral rotation and on the scapular plane. The finite element model developed by ZHENG *et al.* (2020), restricted to a 30° range of abduction motion and incorporating 3D ligament and muscle volumes, reported a peak contact pressure of 7.66 MPa over an 88.04 mm² area at 30° abduction, contrasting with this study's 1.919 MPa over 277.70 mm² at the same angle for a 0 mm defect. SARSHARI *et al*. (2017) found a peak pressure of 0.50 MPa over an 1838 mm² area at 30° abduction and 1.12 MPa over 2224 mm² at 90° abduction, while this study records 3.01 MPa over 397.73 mm² at 90° abduction. The integration of ligaments and the 3D volumes of muscles by ZHENG *et al.* (2020), alongside the specific contact model employed by SARSHARI *et al*. (2017), likely contribute to the variations in findings.

*In-vitro* studies by GREIS *et al.* (2002) and YAMAMOTO, A. *et al.* (2014) used Tekscan pressure sensors on cadaveric shoulders, applying a 440 N force for humeral head compression on a self-centering glenoid. Both studies documented peak pressures in the glenoid's posterior-superior quadrant, with GREIS *et al*. observing approximately 3.01 MPa and 3.30 MPa at 60° and 90° abduction, respectively, and YAMAMOTO *et al*. reporting 3.43 MPa at 90° abduction with external rotation. Beyond the evident difference in methodology, it's noteworthy that Tekscan sensors, as pointed out by YAMAMOTO, A. *et al.* (2014), are originally not designed for non-linear surfaces and have shown issues such as crinkling and damage to the sensels. Additionally, the self-centering glenoid mechanism does not replicate *in vivo* conditions, where there is a translation of the humeral head as a function of muscle activity and joint position (MASSIMINI; WARNER; LI, 2014).

In the glenoid frame of reference, the positioning of the contact area's centroid in this study shares similarities with the *in-vivo* study performed by MASSIMINI, WARNER, and LI (2014). Their research, which analyzed the abduction movement from 0° to 110° within the scapular plane with external arm rotation, mirrors the motion examined in the current study to a notable extent. In their findings, the centroid of the contact area predominantly occupied the anterior-inferior quadrant, initially moving superiorly up to about 66°, before shifting inferiorly through to the end of the abduction movement. However, a distinction lies in the plane of motion analyzed; this study explores abduction in the coronal plane, diverging from the scapular plane approach of MASSIMINI, WARNER, and LI (2014). Additionally, while subjects in their study were tasked with holding dumbbells amounting to 2% of their body weight, the present study takes into account only the weight of the arm. Although a dumbbell weighting 2% of body weight may not seem like much, at 90° abduction it can generate a torque in the glenohumeral joint equivalent to that of the arm weight alone, which may have influenced the contact area's centroid to be located at the anterior-inferior quadrant.

The glenoid track widths derived from this computational model show variations from the measurements conducted by OMORI *et al*., (2014). While this study indicates that glenoid track width expands with an increase in abduction angle, OMORI *et al*. observed a reduction in glenoid track width under similar conditions. The discrepancies can be attributed to several methodological differences. This analysis incorporates glenohumeral cartilages, a factor not considered by OMORI *et al*. Moreover, the definition of point M diverges; in this study, it's identified as the most anterior point on the glenoid cartilage, whereas OMORI *et al*. define it relative to a specific anatomical line. Another distinction is the inclusion of arm weight in our calculations, contrasting with the supine position used in OMORI *et al*.'s MRI images, where the arm weight exerts a different influence. Regarding the size of osseous defects, there is a decrease in glenoid track width as the defect size enlarges. This outcome is expected, as the osseous defect shifts the Point M laterally when projected over the humeral cartilage.

Anterior translations of the humeral head center have been observed in standing patients when the shoulder is externally rotated and the arm is at 90° abduction with the elbow flexed in 90° (BEY *et al.*, 2008; KIM *et al.*, 2017; PARK *et al.*, 2024). However, studies that have performed image acquisition with the patient in supine position have reported posterior translation of the humeral head (DI GIACOMO *et al.*, 2016; MATSUMURA *et al.*, 2019), highlighting a possible influence of the arm weight on humeral head translations. Regarding superior-inferior translations, the studies from BEY *et al*. (2008) and KIM *et al*. (2017) found that the abduction motion is associated with inferior translation of the humeral head center after an initial superior translation.

This study's findings present some correlations and discrepancies with the literature. The inferior translation along the abduction motion correlates well with the above-mentioned studies. However, the posterior translation presented in this study disagrees with the mostly observed anterior translation that happens during external rotation of the arm when the subject is in standing position. The posterior location of the humeral head center may be due to the restriction enforced on the direction of the joint reaction force to point towards the glenoid surface along with the sling effect of the subscapularis muscle. In computational models that exclude ligaments and other passive stabilizers, these two factors prevent the occurrence of anterior translations of the humeral head. Albeit the significant changes in the centroid of the contact area along the abduction movement, humeral head translations were observed to happen inside spheres with diameters smaller than 2.7 mm for all osseous defect sizes and very close to the center of the origin of the coordinate system. The minimum bounding sphere diameters become even smaller if motion is considered only up to 90° abduction, suggesting that there is minimal translational motion to ensure joint stability in static positions of the humerus along the abduction movement.

# 8 CONCLUSION

The glenohumeral joint, due to its inherently unstable geometry, is highly susceptible to dislocations, particularly in the anterior direction. This instability is often exacerbated by the presence of osseous defects in the anterior border of the glenoid, which further compromise joint stability. Although previous research has concentrated on identifying the critical defect size that requires bone grafting, the wider impact of these defects on the contact mechanics of the glenohumeral joint has not been thoroughly investigated.

This study presented a novel analysis of the glenohumeral joint contact mechanics along the shoulder abduction movement with external rotation of the arm in the presence of osseous defects in the anterior border of the glenoid. To this end, a subject-specific model of the glenohumeral joint was developed, incorporating deformable cartilages with non-congruent ellipsoidal articular surfaces. The model included a simulation framework that combined a rigid body model and a finite element model to calculate the smallest muscle forces needed to stabilize the glenohumeral joint. The RB and FE models work iteratively, feeding back humeral head translations and joint reaction moments to each other until a stable humeral position is achieved. Joint stabilization was assumed when the loads on the glenohumeral joint were in mechanical balance and the joint reaction force was directed toward the glenoid articular surface.

Through computational modeling, it was demonstrated how varying sizes of osseous defects influence joint stability, joint reaction force, peak contact pressure, contact area, humeral head translations, muscle forces and the width of the glenoid track. Joint stability was maintained up to 120° of abduction for bone defects of 0 mm and 2 mm, and up to 105° of abduction for bone defects of 3 mm and 4 mm, highlighting the abduction angle beyond which joint stability is compromised. For osseous defects size 5 mm and 6 mm, stability was achieved only up to 45° of abduction. The findings suggest that larger defects are associated with increased joint reaction forces and peak contact pressures, especially at higher abduction angles, which could potentially compromise joint stability and function. Moreover, the study has quantitatively demonstrated the variations in glenoid track width in response to different sizes of osseous defects. Humeral head translations presented no significant differences as a function of osseous defect size and remained within spheres with minimum diameters.

Despite these significant findings, this study acknowledges certain limitations, mainly related to the absence of muscles properties and joint elements that act as passive stabilizers. Firstly, only the deltoid and rotator cuff muscles were included, omitting other muscles that interact with the joint. While these excluded muscles are not central to the abduction or external rotation of the arm, their absence potentially limits the range of feasible solutions for the load sharing problem. Additionally, the modeling of muscles as frictionless taut strings and the use of a bony contour obstacle-set method for muscle path tracing may not fully capture the complexities of actual muscle function, which present full three-dimensional volumes. Finally, not all necessary data could be acquired from the subject, necessitating the use of data from the literature, which may have introduced variability and affect the accuracy of the model. This final limitation prevented the inclusion of a biofidelic muscle model that could have predicted better force estimations.

Future research should aim to integrate more sophisticated mathematical muscle models that include the effects of PCSA, force-length and force-velocity relationships on muscle force estimation. The incorporation of the muscles previously omitted, along with GH ligaments and the glenoid labrum, will offer a more complete understanding of joint stabilization and movement. Utilizing a new set of subject-specific anthropometric data, such as those from the Visual Human Project by the US National Library of Medicine, is recommended to minimize uncertainties stemming from individual anatomical differences. In addition, the inclusion of Hill-Sachs lesions in the models may yield deeper insights into the mechanisms underlying shoulder dislocations and their recurrence. Lastly, further refinement of the simulation framework to enhance computational efficiency and reduce convergence time is essential for practical and widespread application in clinical settings. To this end, it is recommended that additional sensitivity analyses be conducted to evaluate the effects of variations in material model coefficients, optimization parameters, and the number of muscle segments.

In conclusion, this research has provided valuable insights into the impact of osseous defects on the glenohumeral joint's stability and contact mechanics. These findings highlight the importance of quantitative evaluation in clinical decision-making and pave the way for future studies to further enhance our understanding and management of shoulder instability.

**REFERENCES**

ANDREWS, J. R.; CARSON, W. G.; MCLEOD, W. D. Glenoid labrum tears related to the long head of the biceps. **The American Journal of Sports Medicine**, [*s. l.*], v. 13, n. 5, p. 337–341, 1985.

BACLE, G. *et al.* Anatomy and relations of the infraspinatus and the teres minor muscles: a fresh cadaver dissection study. **Surgical and Radiologic Anatomy**, [*s. l.*], v. 39, n. 2, p. 119–126, 2017. Available at: https://doi.org/10.1007/s00276-016-1707-9

BANDHA, D. **Scapulohumeral Rhythm**. [*S. l.*], 2015. Available at: https://www.youtube.com/watch?v=rpzBGlOEW4E. Acesso em: 12 jul. 2021.

BECANOVIC, F. *et al.* Force Sharing Problem During Gait Using Inverse Optimal Control. **IEEE Robotics and Automation Letters**, [*s. l.*], v. 8, n. 2, p. 872–879, 2023. Available at: https://doi.org/10.1109/LRA.2022.3217398

BELTRAN, J. *et al.* The middle glenohumeral ligament: Normal anatomy, variants and pathology. **Skeletal Radiology**, [*s. l.*], v. 31, n. 5, p. 253–262, 2002. Available at: https://doi.org/10.1007/s00256-002-0492-1

BENVENUTI, J. F. **Modélisation tridimensionelle du genou humain**. 1998. [*s. l.*], 1998.

BERGMANN, G. Biomechanics and Pathomechanics of the Shoulder Joint with Reference to Prosthetic Joint Replacement. *In*: KÖLBEL, R.; HELBIG, B.; BLAUTH, W. (org.). **Shoulder replacement**. [*S. l.*]: Springer, Berlin, Heidelberg, 1987.

BERGMANN, G. *et al.* In vivo glenohumeral contact forces-Measurements in the first patient 7 months postoperatively. **Journal of Biomechanics**, [*s. l.*], v. 40, n. 10, p. 2139–2149, 2007. Available at: https://doi.org/10.1016/j.jbiomech.2006.10.037

BEY, M. J. *et al.* Measuring dynamic in-vivo glenohumeral joint kinematics: Technique and preliminary results. **Journal of Biomechanics**, [*s. l.*], v. 41, n. 3, p. 711–714, 2008. Available at: https://doi.org/10.1016/j.jbiomech.2007.09.029

BLANA, D. *et al.* A musculoskeletal model of the upper extremity for use in the development of neuroprosthetic systems. **J Biomech**, [*s. l.*], v. 41, n. 8, p. 1714–1721, 2008. Available at: https://doi.org/10.1016/j.jbiomech.2008.03.001

BOLA, M.; SIMÕES, J.; RAMOS, A. Finite element analysis to predict short and medium-term performance of the anatomical Comprehensive® Total Shoulder System. **Computer Methods and Programs in Biomedicine**, [*s. l.*], v. 219, p. 106751, 2022. Available at: https://doi.org/10.1016/j.cmpb.2022.106751

BOLSTERLEE, B.; VEEGER, H. E. J.; CHADWICK, E. K. Clinical applications of musculoskeletal modelling for the shoulder and upper limb. **Medical and Biological Engineering and Computing**, [*s. l.*], v. 51, n. 9, p. 953–963, 2013. Available at: https://doi.org/10.1007/s11517-013-1099-5

BRETELER, M. D. K.; SPOOR, C. W.; VAN DER HELM, F. C. T. Measuring muscle and joint geometry parameters of a shoulder for modeling purposes. **Journal of Biomechanics**, [*s. l.*], v. 32, n. 11, p. 1191–1197, 1999. Available at:

https://doi.org/10.1016/S0021-9290(99)00122-0

BROWN, J. M. M. *et al.* Muscles within muscles: Coordination of 19 muscle segments within three shoulder muscles during isometric motor tasks. **Journal of Electromyography and Kinesiology**, [*s. l.*], v. 17, n. 1, p. 57–73, 2007. Available at: https://doi.org/10.1016/j.jelekin.2005.10.007

BÜCHLER, P. *et al.* A finite element model of the shoulder: Application to the comparison of normal and osteoarthritic joints. **Clinical Biomechanics**, [*s. l.*], v. 17, n. 9–10, p. 630–639, 2002. Available at: https://doi.org/10.1016/S0268-0033(02)00106-7

BURKART, A. C.; DEBSKI, R. E. Anatomy and function of the glenohumeral ligaments in anterior shoulder instability. **Clinical Orthopaedics and Related Research**, [*s. l.*], n. 400, p. 32–39, 2002. Available at: https://doi.org/10.1097/00003086-200207000-00005

CHARLTON, I. W.; JOHNSON, G. R. A model for the prediction of the forces at the glenohumeral joint. **Proceedings of the Institution of Mechanical Engineers, Part H: Journal of Engineering in Medicine**, [*s. l.*], v. 220, n. 8, p. 801–812, 2006. Available at: https://doi.org/10.1243/09544119JEIM147

CROWNINSHIELD, R. D.; BRAND, R. A. A physiologically based criterion of muscle force prediction in locomotion. **Journal of Biomechanics**, [*s. l.*], v. 14, n. 11, p. 793–801, 1981. Available at: https://doi.org/10.1016/0021-9290(81)90035-X

CUTTS, S.; PREMPEH, M.; DREW, S. Anterior shoulder dislocation. **Annals of the Royal College of Surgeons of England**, [*s. l.*], v. 91, n. 1, p. 2–7, 2009. Available at: https://doi.org/10.1308/003588409X359123

DAMSGAARD, M. *et al.* Analysis of musculoskeletal systems in the AnyBody Modeling System. **Simulation Modelling Practice and Theory**, [*s. l.*], v. 14, n. 8, p. 1100–1111, 2006. Available at: https://doi.org/10.1016/j.simpat.2006.09.001

DE WILDE, L. F.; AUDENAERT, E. A.; BERGHS, B. M. Shoulder prostheses treating cuff tear arthropathy: A comparative biomechanical study. **Journal of Orthopaedic Research**, [*s. l.*], v. 22, n. 6, p. 1222–1230, 2004. Available at: https://doi.org/10.1016/j.orthres.2004.03.010

DEFRODA, S. *et al.* Arthroscopic Bankart Repair for the Management of Anterior Shoulder Instability: Indications and Outcomes. **Current Reviews in Musculoskeletal Medicine**, [*s. l.*], v. 10, n. 4, p. 442–451, 2017. Available at: https://doi.org/10.1007/s12178-017-9435-2

DELUCA, C. J.; FORREST, W. J. Force analysis of individual muscles acting simultaneously on the shoulder during isometric abduction. **J. Biomechanics**, [*s. l.*], v. 6, p. 385–393, 1973.

DEPALMA, A. F.; COOKE, A. J.; PRABHAKAR, M. The role of the subscapularis in recurrent anterior dislocations of the shoulder. **Clin Orthop Relat Res**, [*s. l.*], v. 54, p. 35–49, 1967.

DI GIACOMO, G. *et al.* Glenohumeral translation in ABER position during muscle activity in patients treated with Latarjet procedure: an in vivo MRI study. **Knee Surgery, Sports Traumatology, Arthroscopy**, [*s. l.*], v. 24, n. 2, p. 521–525, 2016. Available at: https://doi.org/10.1007/s00167-015-3896-x

DI GIACOMO, G.; ITOI, E.; BURKHART, S. S. Evolving concept of bipolar bone loss and the hill-sachs lesion: From “engaging/non-engaging” lesion to “on-track/off-track” lesion. **Arthroscopy - Journal of Arthroscopic and Related Surgery**, [*s. l.*], v. 30, n. 1, p. 90–98, 2014. Available at: https://doi.org/10.1016/j.arthro.2013.10.004

DICKERSON, C. R.; CHAFFIN, D. B.; HUGHES, R. E. A mathematical musculoskeletal shoulder model for proactive ergonomic analysis. **Computer Methods in Biomechanics and Biomedical Engineering**, [*s. l.*], v. 10, n. 6, p. 389–400, 2007. Available at: https://doi.org/10.1080/10255840701592727

DOODY, S. G.; FREEDMAN, L.; WATERLAND, J. C. Shoulder movements during abduction in the scapular plane. **Arch Phys Med Rehabil**, [*s. l.*], v. 51, n. 10, p. 595–604, 1970.

DUBOWSKY, S. R. *et al.* Validation of a musculoskeletal model of wheelchair propulsion and its application to minimizing shoulder joint forces. **Journal of Biomechanics**, [*s. l.*], v. 41, p. 2981–2988, 2008. Available at: https://doi.org/10.1016/j.jbiomech.2008.07.032

ELMORE, K. A.; WAYNE, J. S. Soft tissue structures resisting anterior instability in a computational glenohumeral joint model. **Computer Methods in Biomechanics and Biomedical Engineering**, [*s. l.*], v. 16, n. 7, p. 781–789, 2013. Available at: https://doi.org/10.1080/10255842.2011.641120

ENGELHARDT, C. *et al.* Effects of glenoid inclination and acromion index on humeral head translation and glenoid articular cartilage strain. **Journal of Shoulder and Elbow Surgery**, [*s. l.*], v. 26, n. 1, p. 157–164, 2017. Available at: https://doi.org/10.1016/j.jse.2016.05.031

ENGIN, A. E.; CHEN, S.-M. Statistical Data Base for the Biomechanical Properties of the Human Shoulder Complex—I: Kinematics of the Shoulder Complex. **J Biomech Eng.**, [*s. l.*], v. 108, n. 3, p. 215–221, 1986.

ERDEMIR, A. *et al.* Model-based estimation of muscle forces exerted during movements. **Clinical Biomechanics**, [*s. l.*], v. 22, n. 2, p. 131–154, 2007. Available at: https://doi.org/10.1016/j.clinbiomech.2006.09.005

FAVRE, P. *et al.* An algorithm for estimation of shoulder muscle forces for clinical use. **Clinical Biomechanics**, [*s. l.*], v. 20, n. 8, p. 822–833, 2005. Available at: https://doi.org/10.1016/j.clinbiomech.2005.04.007

FAVRE, P. *et al.* An integrated model of active glenohumeral stability. **Journal of Biomechanics**, [*s. l.*], v. 45, n. 13, p. 2248–2255, 2012. Available at: https://doi.org/10.1016/j.jbiomech.2012.06.010

FAVRE, P.; GERBER, C.; SNEDEKER, J. G. Automated muscle wrapping using finite element contact detection. **Journal of Biomechanics**, [*s. l.*], v. 43, n. 10, p. 1931–1940, 2010. Available at: https://doi.org/10.1016/j.jbiomech.2010.03.018

FAVRE, P.; SNEDEKER, J. G.; GERBER, C. Numerical modelling of the shoulder for clinical applications. **Philosophical Transactions of the Royal Society A: Mathematical, Physical and Engineering Sciences**, [*s. l.*], v. 367, n. 1895, p. 2095–

2118, 2009. Available at: https://doi.org/10.1098/rsta.2008.0282

FICK, R. **Handbuch der Anatomie des Menschen, Vol 2**. [*S. l.*]: Gustav Fischer, 1910.

FLORES, P.; LANKARANI, H. M. Spatial rigid-multibody systems with lubricated spherical clearance joints: Modeling and simulation. **Nonlinear Dynamics**, [*s. l.*], v. 60, n. 1–2, p. 99–114, 2010. Available at: https://doi.org/10.1007/s11071-009-9583-z

GARNER, B. A.; PANDY, M. G. A kinematic model of the upper limb based on the visible human project (VHP) image dataset. **Computer Methods in Biomechanics and Biomedical Engineering**, [*s. l.*], v. 2, p. 107–124, 1999.

GARNER, B. A.; PANDY, M. G. Musculoskeletal Model of the Upper Limb Based on the Visible Human Male Dataset. **Computer methods in biomechanics …**, [*s. l.*], n. May 2013, p. 37–41, 2001. Available at: http://www.tandfonline.com/doi/full/10.1080/10255840008908000%5Cnpapers3://publication/uuid/321F1815-FBAA-4117-A760-43E33409B741

GARNER, B. A.; PANDY, M. G. The Obstacle-Set Method for Representing Muscle Paths in Musculoskeletal Models. [*s. l.*], v. 5842, 2000. Available at: https://doi.org/10.1080/10255840008915251

GRAICHEN, H. *et al.* Glenohumeral translation during active and passive elevation of the shoulder - A 3D open-MRI study. **Journal of Biomechanics**, [*s. l.*], v. 33, n. 5, p. 609–613, 2000. Available at: https://doi.org/10.1016/S0021-9290(99)00209-2

GRAICHEN, H. *et al.* Validation of cartilage volume and thickness measurements in the human shoulder with quantitative magnetic resonance imaging. **Osteoarthritis and Cartilage**, [*s. l.*], v. 11, n. 7, p. 475–482, 2003. Available at: https://doi.org/10.1016/S1063-4584(03)00077-3

GREIS, P. E. *et al.* Glenohumeral articular contact areas and pressures following labral and osseous injury to the anteroinferior quadrant of the glenoid. **Journal of Shoulder and Elbow Surgery**, [*s. l.*], v. 11, n. 5, p. 442–451, 2002. Available at: https://doi.org/10.1067/mse.2002.124526

HALDER, A. M. *et al.* Effects of the glenoid labrum and glenohumeral abduction on stability of the shoulder joint through concavity-compression: An in vitro study. **Journal of Bone and Joint Surgery - Series A**, [*s. l.*], v. 83, n. 7, p. 1062–1069, 2001. Available at: https://doi.org/10.2106/00004623-200107000-00013

HALL, S. J. **Basic Biomechanics**. 6 ed.ed. [*S. l.*]: McGraw-Hill, 2012.

HAPPEE, R.; VAN DER HELM, F. C. T. The control of shoulder muscles during goal directed movements, an inverse dynamic analysis. **Journal of Biomechanics**, [*s. l.*], v. 28, n. 10, p. 1179–1191, 1995. Available at: https://doi.org/10.1016/0021-9290(94)00181-3

HOLZBAUR, K. R. S.; MURRAY, W. M.; DELP, S. L. A model of the upper extremity for simulating musculoskeletal surgery and analyzing neuromuscular control. **Annals of Biomedical Engineering**, [*s. l.*], v. 33, n. 6, p. 829–840, 2005. Available at: https://doi.org/10.1007/s10439-005-3320-7

IANNOTTI, P.; SCHNECK, L.; GABRIEL, P. The Normal Glenohumeral Relationships. **The Journal of Bone and Joint Surgery**, [*s. l.*], v. 74, p. 491–500, 1992.

INMAN, V. T. Normal motions of the shoulder joint. **The Journal of Bone and Joint Surgery**, [*s. l.*], v. XLV, n. 2, p. 105–120, 1944.

INMAN, V. T.; SAUNDERS, J. B.; ABBOTT, L. C. Observations on the function of the shoulder joint. **The Journal of Bone and Joint Surgery**, [*s. l.*], v. XLV, n. 2, p. 105–120, 1944. Available at: https://doi.org/10.1016/S0022-3913(12)00134-5

ITOI, E. “On-track” and “off-track” shoulder lesions. **EFORT Open Reviews**, [*s. l.*], v. 2, n. 8, p. 343–351, 2017. Available at: https://doi.org/10.1302/2058-5241.2.170007

ITOI, E. *et al.* The Effect of a Glenoid Defect on Anteroinferior Stability of the Shoulder After Bankart Repair: A Cadaveric Study*. **The Journal of Bone and Joint Surgery-American Volume**, [*s. l.*], v. 82, n. 1, p. 35–46, 2000. Available at: https://doi.org/10.2106/00004623-200001000-00005

ITOI, E.; MORREY, B. F.; AN, K.-N. Biomechanics of the shoulder. *In*: ROCKWOOD JR., C. A.; MATSEN III, F. A. (org.). **The Shoulder**. [*S. l.*]: Saunders, 2009. p. 213–265. Available at: https://doi.org/10.1007/978-981-15-3159-0_6

JOBE, C. M.; PHIPATANAKUL, W. P.; COEN, M. J. Gross Anatomy of the Shoulder. *In*: ROCKWOOD JR., C. A.; MATSEN III, F. A. (org.). **Rockwood and Matsen’s The Shoulder**. 2. ed. [*S. l.*]: W.B. Saunders Company, 2009. p. 33–100. Available at: https://doi.org/10.1016/b978-1-4160-3427-8.50008-8

JOHNSON, G. R. *et al.* Modelling the muscles of the scapula morphometric and coordinate data and functional implications. **Journal of Biomechanics**, [*s. l.*], v. 29, n. 8, p. 1039–1051, 1996. Available at: https://doi.org/10.1016/0021-9290(95)00176-X

JUNIOR, A. N. T. *et al.* A numerical study of the contact geometry and pressure distribution along the glenoid track. **Medical Engineering and Physics**, [*s. l.*], v. 110, n. September, 2022. Available at: https://doi.org/10.1016/j.medengphy.2022.103898

KARLSSON, D.; PETERSON, B. Towards a model for force predictions in the human shoulder. **Journal of Biomechanics**, [*s. l.*], v. 25, n. 2, p. 189–199, 1992. Available at: https://doi.org/10.1016/0021-9290(92)90275-6

KEATING, J. *et al.* The relative strengths of the rotator cuff muscles. A cadaver study. **The Journal of Bone and Joint Surgery. British volume**, [*s. l.*], v. 75-B, n. 1, p. 137–140, 1993. Available at: https://doi.org/10.1302/0301-620X.75B1.8421011

KENHUB - BICEPS BRACHII MUSCLE. **Biceps brachii**. [*S. l.*], [*s. d.*]. Available at: https://www.kenhub.com/en/library/anatomy/biceps-brachii-muscle. Acesso em: 26 abr. 2021.

KENHUB - THE SHOULDER JOINT. **The shoulder joint**. [*S. l.*], [*s. d.*]. Available at: https://www.kenhub.com/en/library/anatomy/the-shoulder-joint. Acesso em: 27 abr. 2021.

KHANDARE, S.; ARCE, R. A.; VIDT, M. E. Muscle compensation strategies to maintain glenohumeral joint stability with increased rotator cuff tear severity: A simulation study. **Journal of Electromyography and Kinesiology**, [*s. l.*], v. 62, n. July 2019, p. 102335,

2022. Available at: https://doi.org/10.1016/j.jelekin.2019.07.005

KHANDARE, S.; VIDT, M. E. Development of a more biofidelic musculoskeletal model with humeral head translation and glenohumeral ligaments. **Computer Methods in Biomechanics and Biomedical Engineering**, [*s. l.*], v. 0, n. 0, p. 1–8, 2022. Available at: https://doi.org/10.1080/10255842.2022.2127319

KIM, D. S. *et al.* Comparison of dynamics in 3D glenohumeral position between primary dislocated shoulders and contralateral healthy shoulders. **Journal of Orthopaedics**, [*s. l.*], v. 14, n. 1, p. 195–200, 2017. Available at: https://doi.org/10.1016/j.jor.2016.12.014

KLEMT, C. *et al.* Analysis of shoulder compressive and shear forces during functional activities of daily life. **Clinical Biomechanics**, [*s. l.*], v. 54, n. March, p. 34–41, 2018. Available at: https://doi.org/10.1016/j.clinbiomech.2018.03.006

KLEMT, C. *et al.* The contribution of the glenoid labrum to glenohumeral stability under physiological joint loading using finite element analysis. **Computer Methods in Biomechanics and Biomedical Engineering**, [*s. l.*], v. 20, n. 15, p. 1613–1622, 2017. Available at: https://doi.org/10.1080/10255842.2017.1399262

KLEMT, C. *et al.* The critical size of a defect in the glenoid causing anterior instability of the shoulder after a Bankart repair , under physiological joint loading. **The Bone & Joint Journal**, [*s. l.*], v. 101, n. B, p. 68–74, 2019. Available at: https://doi.org/10.1302/0301-620X.101B1.BJJ-2018-0974.R1

LANDIN, D. *et al.* The role of the biceps brachii in shoulder elevation. **Journal of Electromyography and Kinesiology**, [*s. l.*], v. 18, p. 270–275, 2008. Available at: https://doi.org/10.1016/j.jelekin.2006.09.012

LANDIN, D.; THOMPSON, M.; JACKSON, M. R. Actions of the Biceps Brachii at the Shoulder : A Review. **J Clin Med Res**, [*s. l.*], v. 9, n. 8, p. 667–670, 2017.

LEVY, A. S. *et al.* Function of the long head of the biceps at the shoulder : Electromyographic analysis. **Journal of Shoulder and Elbow Surgery**, [*s. l.*], v. 10, n. 3, p. 250–255, 2001. Available at: https://doi.org/10.1067/mse.2001.113087

LIAVAAG, S. *et al.* The epidemiology of shoulder dislocations in Oslo. **Scandinavian Journal of Medicine and Science in Sports**, [*s. l.*], v. 21, n. 6, p. 334–340, 2011. Available at: https://doi.org/10.1111/j.1600-0838.2011.01300.x

LIPPITT, S.; MATSEN, F. Mechanism of glenohumeral joint stability. **Clinical Orthopaedics and Related Research**, [*s. l.*], v. 291, p. 20–28, 1993.

MACHADO, M. *et al.* Influence of the contact model on the dynamic response of the human knee joint. **Proceedings of the Institution of Mechanical Engineers, Part K: Journal of Multi-body Dynamics**, [*s. l.*], v. 225, n. 4, p. 344–358, 2011. Available at: https://doi.org/10.1177/1464419311413988

MARQUARDT, B. *et al.* The influence of arthroscopic subscapularis tendon and anterior capsular release on glenohumeral translation: A biomechanical model. **Journal of Shoulder and Elbow Surgery**, [*s. l.*], v. 15, n. 4, p. 502–508, 2006. Available at: https://doi.org/10.1016/j.jse.2005.09.018

MASSIMINI, D. F.; WARNER, J. J. P.; LI, G. Glenohumeral joint cartilage contact in the healthy adult during scapular plane elevation depression with external humeral rotation. **Journal of Biomechanics**, [*s. l.*], v. 47, n. 12, p. 3100–3106, 2014. Available at: https://doi.org/10.1016/j.jbiomech.2014.06.034

MATSUMURA, N. *et al.* Glenohumeral translation during active external rotation with the shoulder abducted in cases with glenohumeral instability: a 4-dimensional computed tomography analysis. **Journal of Shoulder and Elbow Surgery**, [*s. l.*], v. 28, n. 10, p. 1903–1910, 2019. Available at: https://doi.org/10.1016/j.jse.2019.03.008

MORREY, B.; ITOI, E.; AN, K. The Shoulder. *In*: ROCKWOOD, C. A. J. .; MATSEN, F. A. I. (org.). **The Shoulder**. 2nd. ed. Philadelphia: WB Saunders, 1998. p. 233–276.

MOSER, T. *et al.* The deltoid, a forgotten muscle of the shoulder. **Skeletal Radiology**, [*s. l.*], v. 42, n. 10, p. 1361–1375, 2013. Available at: https://doi.org/10.1007/s00256-013-1667-7

NIKOOYAN, A. A. *et al.* Development of a comprehensive musculoskeletal model of the shoulder and elbow. **Medical and Biological Engineering and Computing**, [*s. l.*], v. 49, n. 12, p. 1425–1435, 2011. Available at: https://doi.org/10.1007/s11517-011-0839-7

NIKOOYAN, Ali Asadi *et al.* Comparison of two methods for In Vivo estimation of the glenohumeral joint rotation center (GH-JRC) of the patients with shoulder hemiarthroplasty. **PLoS ONE**, [*s. l.*], v. 6, n. 3, p. 1–7, 2011. Available at: https://doi.org/10.1371/journal.pone.0018488

OMORI, Y. *et al.* Measurement of the glenoid track in vivo as investigated by 3-dimensional motion analysis using open MRI. **American Journal of Sports Medicine**, [*s. l.*], v. 42, n. 6, p. 1290–1295, 2014. Available at: https://doi.org/10.1177/0363546514527406

ORTOPEDIA E OMBRO. **A lesão de Hill Sachs e a lesão de Bankart explicadas**. [*S. l.*], [*s. d.*]. Available at: https://ortopediaeombro.com.br/lesao-de-hill-sachs-e-lesao-de-bankart-lesao-do-labio-anterior/. Acesso em: 28 abr. 2021.

PAGNANI, M. J. *et al.* Role of the long head of the biceps brachii in glenohumeral stability : A biomechanical study in cadavera. **Journal of Shoulder and Elbow Surgery**, [*s. l.*], v. 5, n. 4, p. 255–262, 1996. Available at: https://doi.org/10.1016/s1058-2746(96)80051-6

PAPAZAFEIROPOULOS, G.; MUÑIZ-CALVENTE, M.; MARTÍNEZ-PAÑEDA, E. Abaqus2Matlab: A suitable tool for finite element post-processing. **Advances in Engineering Software**, [*s. l.*], v. 105, p. 9–16, 2017. Available at: https://doi.org/10.1016/j.advengsoft.2017.01.006

PARK, J. *et al.* In Vivo 3-Dimensional Dynamic Evaluation of Shoulder Kinematics After the Latarjet Procedure: Comparison With the Contralateral Healthy Shoulder. **Orthopaedic Journal of Sports Medicine**, [*s. l.*], v. 12, n. 3, p. 1–7, 2024. Available at: https://doi.org/10.1177/23259671241226909

PASSANANTE, G. J. *et al.* Inferior glenohumeral ligament (IGHL) complex: anatomy, injuries, imaging features, and treatment options. **Emergency Radiology**, [*s. l.*], v. 24,

n. 1, p. 65–71, 2017. Available at: https://doi.org/10.1007/s10140-016-1431-0

PAULSEN, F.; WASCHKE, J. **Sobotta - Atlas of Human Anatomy, Vol. 1**. 15th. ed. [*S. l.*]: Urban & Fischer, 2013.

PÉCORA, J. O. R. *et al.* Glenoid track evaluation by a validated finite-element shoulder numerical model. **Orthopaedics and Traumatology: Surgery and Research**, [*s. l.*], v. 106, n. 4, p. 735–742, 2020. Available at: https://doi.org/10.1016/j.otsr.2020.03.004

POPPEN, N. K.; WALKER, P. S. Forces at the glenohumeral joint in abduction. **Clin Orthop Relat Res.**, [*s. l.*], v. Sep, n. 135, p. 165–170, 1978.

POPPEN, N. K.; WALKER, P. S. Normal and abnormal motion of the shoulder. **The Journal of Bone & Joint Surgery**, [*s. l.*], v. 58, n. 2, p. 195–201, 1976.

PRAAGMAN, M. *et al.* The relationship between two different mechanical cost functions and muscle oxygen consumption. **Journal of Biomechanics**, [*s. l.*], v. 39, n. 4, p. 758–765, 2006. Available at: https://doi.org/10.1016/j.jbiomech.2004.11.034

PRINOLD, J. A. I. *et al.* Musculoskeletal shoulder models: A technical review and proposals for research foci. **Proceedings of the Institution of Mechanical Engineers, Part H: Journal of Engineering in Medicine**, [*s. l.*], v. 227, n. 10, p. 1041–1057, 2013. Available at: https://doi.org/10.1177/0954411913492303

QUENTAL, C. *et al.* A multibody biomechanical model of the upper limb including the shoulder girdle. **Multibody System Dynamics**, [*s. l.*], v. 28, n. 1–2, p. 83–108, 2012. Available at: https://doi.org/10.1007/s11044-011-9297-0

QUENTAL, C. *et al.* A new shoulder model with a biologically inspired glenohumeral joint. **Medical Engineering and Physics**, [*s. l.*], v. 38, n. 9, p. 969–977, 2016. Available at: https://doi.org/10.1016/j.medengphy.2016.06.012

RATHI, S.; TAYLOR, N. F.; GREEN, R. A. The upper and lower segments of subscapularis muscle have different roles in glenohumeral joint functioning. **Journal of Biomechanics**, [*s. l.*], v. 63, p. 92–97, 2017. Available at: https://doi.org/10.1016/j.jbiomech.2017.08.007

RITTER, J. AN EFFICIENT BOUNDING SPHERE. *In*: GRAPHICS GEMS. [*S. l.*]: Elsevier, 1990. p. 301–303. Available at: https://doi.org/10.1016/B978-0-08-050753-8.50063-2

RODOSKY, M. W.; HARNER, C. D.; FU, F. H. The Role of the Long Head of the Biceps Muscle and Superior Glenoid Labrum in Anterior Stability of the Shoulder. **The American Journal of Sports Medicine**, [*s. l.*], v. 22, n. 1, p. 121–130, 1994. Available at: https://doi.org/10.1177/036354659402200119

SADEQI, S. *et al.* A Validated Open-Source Shoulder Finite Element Model and Investigation of the Effect of Analysis Precision. **Annals of Biomedical Engineering**, [*s. l.*], v. 51, n. 1, p. 24–33, 2023. Available at: https://doi.org/10.1007/s10439-022-03018-8

SAHARA, W. *et al.* Influence of humeral abduction angle on axial rotation and contact area at the glenohumeral joint. **Journal of Shoulder and Elbow Surgery**, [*s. l.*], v. 28, n. 3, p. 570–577, 2019. Available at: https://doi.org/10.1016/j.jse.2018.08.023

SAITO, H. *et al.* Location of the glenoid defect in shoulders with recurrent anterior dislocation. **American Journal of Sports Medicine**, [*s. l.*], v. 33, n. 6, p. 889–893, 2005. Available at: https://doi.org/10.1177/0363546504271521

SARSHARI, E. *et al.* A simulation framework for humeral head translations. **Medical Engineering and Physics**, [*s. l.*], v. 49, p. 140–147, 2017. Available at: https://doi.org/10.1016/j.medengphy.2017.08.013

SCHLEICH, C. *et al.* Thickness Distribution of Glenohumeral Joint Cartilage: A Normal Value Study on Asymptomatic Volunteers Using 3-Tesla Magnetic Resonance Tomography. **Cartilage**, [*s. l.*], v. 8, n. 2, p. 105–111, 2017. Available at: https://doi.org/10.1177/1947603516651669

SHAH, A. *et al.* Incidence of shoulder dislocations in the UK, 1995-2015: A population-based cohort study. **BMJ Open**, [*s. l.*], v. 7, n. 11, 2017. Available at: https://doi.org/10.1136/bmjopen-2017-016112

SINS, L. *et al.* Adaptation of the AnyBody$^{TM}$ Musculoskeletal Shoulder Model to the Nonconforming Total Shoulder Arthroplasty Context. **Journal of Biomechanical Engineering**, [*s. l.*], v. 137, n. 10, p. 1–7, 2015. Available at: https://doi.org/10.1115/1.4031330

SOSLOWSKY, L. J. *et al.* Articular Geometry of the GH Joint. **Clinical Orthopaedics and Related Research**, [*s. l.*], p. 181–190, 1992.

STEENBRINK, F. *et al.* Glenohumeral stability in simulated rotator cuff tears. **Journal of Biomechanics**, [*s. l.*], v. 42, n. 11, p. 1740–1745, 2009. Available at: https://doi.org/10.1016/j.jbiomech.2009.04.011

STEFANIAK, J. *et al.* Clinical and radiological examination of bony-mediated shoulder instability. **EFORT Open Reviews**, [*s. l.*], v. 5, n. 11, p. 815–827, 2020. Available at: https://doi.org/10.1302/2058-5241.5.200049

STEINBECK, J.; LILJENQVIST, U.; JEROSCH, J. The anatomy of the glenohumeral ligamentous complex and its contribution to anterior shoulder stability. **J Shoulder Elbow Surg**, [*s. l.*], v. 7, p. 122 – 126, 1998.

TERRIER, A. *et al.* **A musculoskeletal shoulder model based on pseudo-inverse and null-space optimization**. [*S. l.: s. n.*], 2010. Available at: https://doi.org/10.1016/j.medengphy.2010.07.006

TERRIER, A. *et al.* An algorithm to allow humerus translation in the indeterminate problem of shoulder abduction. **Medical Engineering and Physics**, [*s. l.*], v. 30, n. 6, p. 710–716, 2008. Available at: https://doi.org/10.1016/j.medengphy.2007.07.011

TERRIER, A. *et al.* Effect of supraspinatus deficiency on humerus translation and glenohumeral contact force during abduction. **Clinical Biomechanics**, [*s. l.*], v. 22, n. 6, p. 645–651, 2007. Available at: https://doi.org/10.1016/j.clinbiomech.2007.01.015

TORTORA, G. J.; DERRYCKSON, B. H. **Principles of Anatomy & Physiology**. 13th. ed. [*S. l.*]: Wiley, 2011.

TRICHEZ JR., A. N. *et al.* Estimativa das forças exercidas pelos segmentos musculares utilizando diferentes restrições. *In*: , 2020, Foz do Iguaçu, Paraná, Brasil.

**XLI Ibero-Latin-American Congress on Computational Methods in Engineering (CILAMCE)**. Foz do Iguaçu, Paraná, Brasil: [*s. n.*], 2020. p. 1–7.

TURKEL, S. J. *et al.* Stabilizing mechanisms preventing anterior dislocation of the glenohumeral joint. **J Bone Joint Surg Am.**, [*s. l.*], v. 63, n. 8, p. 1208–1217, 1981.

VAN DER HELM, F. C. T. A finite element musculoskeletal model of the shoulder mechanism. **Journal of Biomechanics**, [*s. l.*], v. 27, n. 5, 1994a. Available at: https://doi.org/10.1016/0021-9290(94)90065-5

VAN DER HELM, F. C. T. A finite element musculoskeletal model of the shoulder mechanism. **Journal of Biomechanics**, [*s. l.*], v. 27, n. 5, p. 551–596, 1994b. Available at: https://doi.org/10.1016/0021-9290(94)90065-5

VAN DER HELM, F. C. T.; VEENBAAS, R. Modelling the mechanical effect of muscles with large attachment sites: Application to the shoulder mechanism. **Journal of Biomechanics**, [*s. l.*], v. 24, n. 12, p. 1151–1163, 1991. Available at: https://doi.org/10.1016/0021-9290(91)90007-A

VEEGER, H. E. J. The position of the rotation center of the glenohumeral joint. **Journal of Biomechanics**, [*s. l.*], v. 33, n. 12, p. 1711–1715, 2000. Available at: https://doi.org/10.1016/S0021-9290(00)00141-X

VEEGER, H. E. J.; ROZENDAAL, L. A.; VAN DER HELM, F. C. T. Load on the shoulder in low intensity wheelchair propulsion. **Clinical Biomechanics**, [*s. l.*], v. 17, n. 3, p. 211–218, 2002. Available at: https://doi.org/10.1016/S0268-0033(02)00008-6

VIEWMEDICA. **Hill-Sachs lesion**. [*S. l.*], [*s. d.*]. Available at: https://viewmedica.com/vm/index/brochure/6559/hillsachs/en. Acesso em: 28 abr. 2021.

WALIA, P. *et al.* Influence of Combined Hill-Sachs and Bony Bankart Defects on Range of Motion in Anterior Instability of the Shoulder in a Finite Element Model. **Arthroscopy - Journal of Arthroscopic and Related Surgery**, [*s. l.*], v. 31, n. 11, p. 2119–2127, 2015. Available at: https://doi.org/10.1016/j.arthro.2015.04.099

WARNER, J. J. *et al.* Static capsuloligamentous restraints to superior-inferior translation of the glenohumeral joint. **Am J Sports Med**, [*s. l.*], v. 20, n. 6, p. 675–685, 1992.

WEBB, J. D.; BLEMKER, S. S.; DELP, S. L. 3D Finite Element Models of Shoulder Muscles for Computing Lines of Actions and Moment Arms. **Comput Methods Biomech Biomed Engin**, [*s. l.*], v. 17, n. 8, p. 829–837, 2014. Available at: https://doi.org/10.1038/jid.2014.371

WELZL, E. Smallest enclosing disks (balls and ellipsoids). *In*: NEW RESULTS AND NEW TRENDS IN COMPUTER SCIENCE. Berlin/Heidelberg: Springer-Verlag, 1991. p. 359–370. Available at: https://doi.org/10.1007/BFb0038202

WESTERHOFF, P. *et al.* An instrumented implant for in vivo measurement of contact forces and contact moments in the shoulder joint. **Medical Engineering and Physics**, [*s. l.*], v. 31, n. 2, p. 207–213, 2009a. Available at: https://doi.org/10.1016/j.medengphy.2008.07.011

WESTERHOFF, P. *et al.* In vivo measurement of shoulder joint loads during activities of daily living. **Journal of Biomechanics**, [*s. l.*], v. 42, n. 12, p. 1840–1849, 2009b. Available at: https://doi.org/10.1016/j.jbiomech.2009.05.035

WIKIPEDIA - DELTOID MUSCLE. **Deltoid muscle**. [*S. l.*], [*s. d.*]. Available at: https://en.wikipedia.org/wiki/Deltoid_muscle. Acesso em: 26 abr. 2021.

YAMAMOTO, A. *et al.* Glenohumeral contact pressure with simulated anterior labral and osseous defects in cadaveric shoulders before and after soft tissue repair. **American Journal of Sports Medicine**, [*s. l.*], v. 42, n. 8, p. 1947–1954, 2014. Available at: https://doi.org/10.1177/0363546514531905

YAMAMOTO, N. *et al.* Contact between the glenoid and the humeral head in abduction, external rotation, and horizontal extension: A new concept of glenoid track. **Journal of Shoulder and Elbow Surgery**, [*s. l.*], v. 16, n. 5, p. 649–656, 2007. Available at: https://doi.org/10.1016/j.jse.2006.12.012

YAMAMOTO, N. *et al.* Effect of an anterior glenoid defect on anterior shoulder stability: A cadaveric study. **American Journal of Sports Medicine**, [*s. l.*], v. 37, n. 5, p. 949–954, 2009. Available at: https://doi.org/10.1177/0363546508330139

YAMAMOTO, N. *et al.* Stabilizing mechanism in bone-grafting of a large glenoid defect. **Journal of Bone and Joint Surgery**, [*s. l.*], v. 92, n. 11, p. 2059–2066, 2010. Available at: https://doi.org/10.2106/JBJS.I.00261

YANAGAWA, T. *et al.* Contributions of the individual muscles of the shoulder to glenohumeral joint stability during abduction. **Journal of Biomechanical Engineering**, [*s. l.*], v. 130, n. 2, p. 1–9, 2008. Available at: https://doi.org/10.1115/1.2903422

YANG, T. C. *et al.* Using the “Hill–Sachs interval to glenoid track width ratio” for prediction of recurrent instability after arthroscopic Bankart repair. **Orthopaedics and Traumatology: Surgery and Research**, [*s. l.*], v. 104, n. 6, p. 797–801, 2018. Available at: https://doi.org/10.1016/j.otsr.2018.02.013

YOUM, T. *et al.* The effect of the long head of the biceps on glenohumeral kinematics. **J Shoulder Elbow Surg**, [*s. l.*], v. 18, p. 122–129, 2009. Available at: https://doi.org/10.1016/j.jse.2008.06.003

ZACCHILLI, M. A.; OWENS, B. D. Epidemiology of shoulder dislocations presenting to emergency departments in the United States. **Journal of Bone and Joint Surgery - Series A**, [*s. l.*], v. 92, n. 3, p. 542–549, 2010. Available at: https://doi.org/10.2106/JBJS.I.00450

ZHENG, M. *et al.* Finite element models of the human shoulder complex: a review of their clinical implications and modelling techniques. **Int. J. Numer. Meth. Biomed. Engng.**, [*s. l.*], p. 24, 2016. Available at: https://doi.org/10.1002/cnm

ZHENG, M. *et al.* Subject-specific Finite Element Modelling of the Human Shoulder Complex Part 1 : Model Construction and Quasi-static Abduction Simulation. [*s. l.*], v. 17, p. 1224–1238, 2020. Available at: https://doi.org/10.1007/s42235-020-0098-0

ZUMSTEIN, V. *et al.* The glenohumeral joint - a mismatching system? A morphological analysis of the cartilaginous and osseous curvature of the humeral head and the glenoid cavity. **Journal of Orthopaedic Surgery and Research**, [*s. l.*], v. 9, n. 1, p. 1–6, 2014a. Available at: https://doi.org/10.1186/1749-799X-9-34

ZUMSTEIN, V. *et al.* Thickness distribution of the glenohumeral joint cartilage: A quantitative study using computed tomography. **Surgical and Radiologic Anatomy**, [*s. l.*], v. 36, n. 4, p. 327–331, 2014b. Available at: https://doi.org/10.1007/s00276-013-1221-2

# APPENDIX A – GLENOHUMERAL CARTILAGES

The reconstruction of the tridimensional cartilages of the humeral head and glenoid fossa was performed using data from the literature and also from MRI and CT scans acquired from the right shoulder of a healthy male subject, aged 24, with a body mass of 70 kg and a stature of 1.72 meters (Section 4.1). The first step in modeling the humeral head cartilage was to define the anatomical neck of the humerus. To achieve this, curves were drawn along the surface of the humeral head, and inflection points were identified. A best-fit plane was then established using these inflection points, which was designated as the anatomical neck of the humerus. The center of the cross-section created by this plane is referred to as point U. Figure 58 illustrates the procedure.

Figure 58 – From left to right: curves used to identify the inflection points (A); lateral view of the section defined by the plane designated as the anatomical neck of the humerus in green; and frontal view of the section with point U at its center.

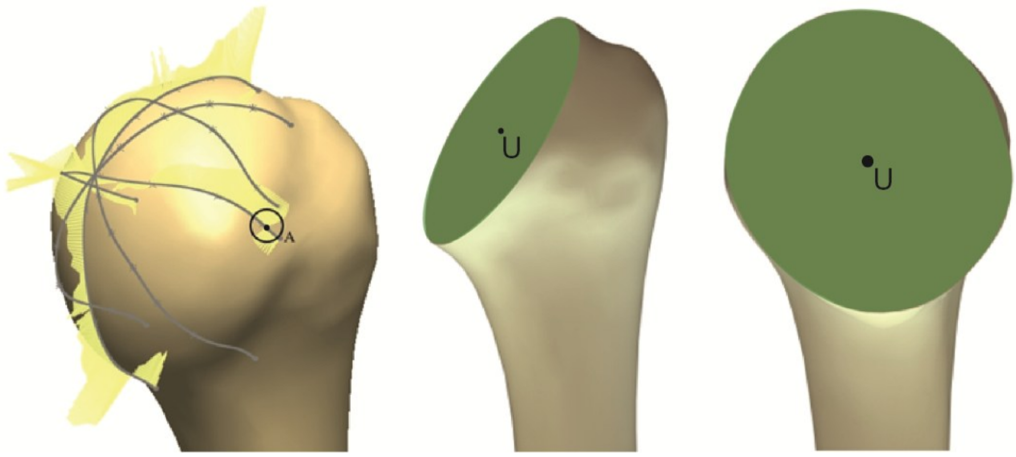


From the author.

The base of the cartilage is 2 mm distant from the anatomical neck of the humerus, as observed in the clinical exams. From point U, a line is traced orthogonally to the anatomical neck of the humerus up to the articular surface of the humeral head. This distance is used to define one of the radii of the cartilage's articular surface (outer surface) which is depicted in Figure 59. The radii parallel to the anatomical neck of the humerus, illustrated in Figure 30, were based on data from clinical exams and from the literature (SOSLOWSKY *et al.*, 1992; ZUMSTEIN *et al.*, 2014). The bone surface (inside surface) of the cartilage is congruent with the humeral head, resulting in a tridimensional volume with variable thickness, which is in accordance with the literature and clinical images (Figure 60).

Figure 59 – Plane of the anatomical neck of the humerus in blue, which was used to design the humeral head cartilage and the cartilages' articular surface radii.

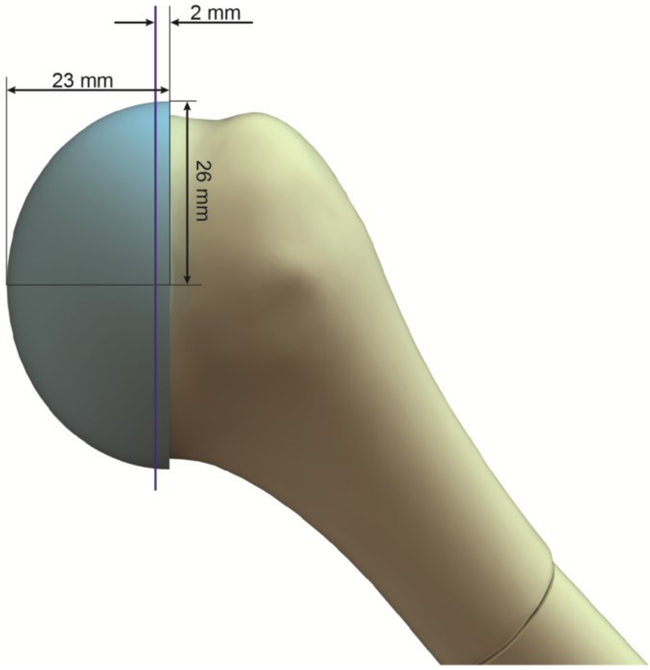


From the author.

Figure 60 – Thickness distribution of the humeral head cartilage.

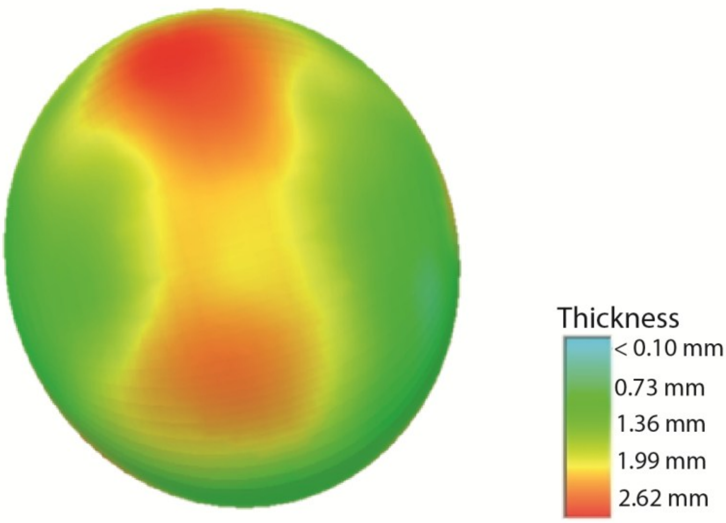


From the author.

The reconstruction of the glenoid cartilage starts by tracing the contour of the glenoid fossa in the glenoid plane (Figure 61) and extruding it up to the glenoid fossa. As with the humeral head cartilage, the bone surface (in this case, the outer surface) is congruent with the glenoid fossa, granting the cartilage a variable thickness (Figure 62) that is in accordance with the literature (ZUMSTEIN *et al*., 2014). The articular surface of the cartilage (in this case, the inside surface) is designed from radii obtained from the clinical exams data, which are presented in Figure 29.

Figure 61 – Contour of the glenoid fossa to design the glenoid cartilage.

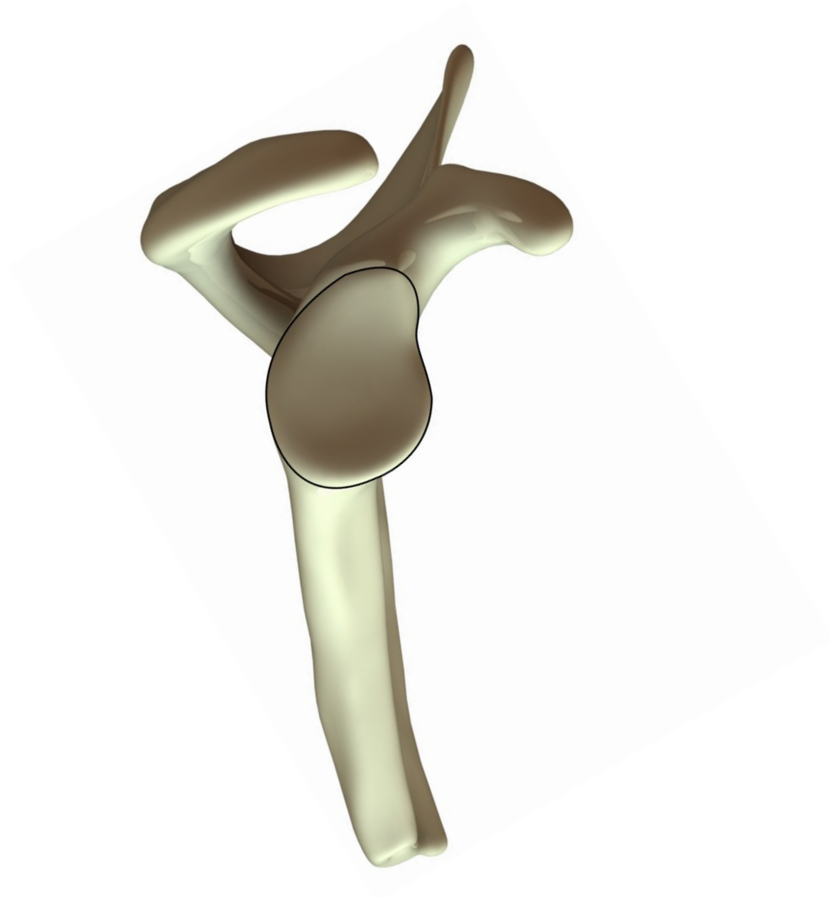

From the author.

Figure 62 – Thickness distribution of the glenoid cartilage.

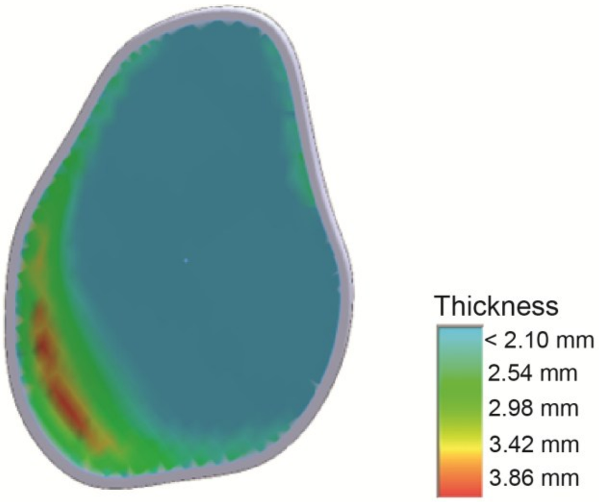


From the author.

# APPENDIX B – MESH CONVERGENCE STUDY

To ensure that the results are independent of mesh size, a mesh convergence study was performed for the joint cartilages. The procedure to find an adequate mesh size is similar to the procedure presented in Section 4. Here, a compressive force, as defined in Section 3.3.2, is applied to the humerus and the translational degrees of freedom are progressively released to ensure convergence. Starting with a coarse mesh, refinement is performed until there is a difference of less than 5% from all the desired outputs. The chosen output variables are percentage of distorted elements, peak contact pressure (CPRESS), contact area (CAREA) and maximum von Mises stress (MAXMISES). Based on the results presented in Table 18 and Table 19, the chosen mesh size is mesh D.

Table 18 – Mesh size for the mesh convergence study.

| Mesh | Cartilages | Approximate global size | Number of elements |
|---|---|---|---|
| A | Glenoid cartilage | 3 | 2066 |
| | Humeral head cartilage | 3.25 | 2761 |
| B | Glenoid cartilage | 2 | 4172 |
| | Humeral head cartilage | 2.25 | 6774 |
| C | Glenoid cartilage | 1.75 | 4920 |
| | Humeral head cartilage | 2 | 10610 |
| D | Glenoid cartilage | 1.25 | 11064 |
| | Humeral head cartilage | 1.5 | 23432 |
| E | Glenoid cartilage | 1 | 18845 |
| | Humeral head cartilage | 1.25 | 30628 |

Table 19 – Outputs obtained for the mesh convergence study.

| Mesh | Wallclock time (s) | CPRESS (MPa) | CAREA (mm²) | MAXMISES (MPa) |
|---|---|---|---|---|
| A | 344 | 2,531 | 454,022 | 1,901 |
| B | 601 | 2,602 | 460,321 | 1,997 |
| C | 737 | 2,581 | 463,699 | 2,097 |
| D | 1665 | 2,584 | 467,884 | 2,357 |
| E | 2739 | 2,592 | 469,279 | 2,37 |

# APPENDIX C – GLENOHUMERAL RATIOS

Assume $C_x$ to be the glenohumeral ratio in direction $x$ of the coordinate system described in Section 4. It is defined as the quotient $C_x = \|F_{translate,crit}/F_{compress}\|$, where $F_{compress}$ is the applied compression force and $F_{translate,crit}$ is the critic tangential force that causes a dislocation to occur. If the calculated joint reaction force $\boldsymbol{r}_a$ presents a compressive component $\|r_{a,z}\| = \|F_{compress}\|$ and a tangential component $\|r_{a,x}\| = \|F_{translate,1}\| < \|F_{translate,crit}\|$, then $\left\|\frac{r_{a,x}}{r_{a,z}}\right\| < C_x$, and dislocation does not occur. However, if the joint reaction force presents a tangential component $\|r_{a,x}\| = \|F_{translate,2}\| \geq \|F_{translate,crit}\|$, then $\left\|\frac{r_{a,x}}{r_{a,z}}\right\| \geq C_x$, and it is assumed that dislocation occurs. Figure 63 illustrates this explanation, where $F_{translate,1}$ is represented by a green vector, $F_{translate,2}$ is represented by a yellow vector, and $F_{translate,crit}$ is represented by a red vector

Figure 63 – Effect of the glenohumeral ratios in the $\boldsymbol{xz}$ plane to constrain the joint reaction force to point toward the glenoid surface.

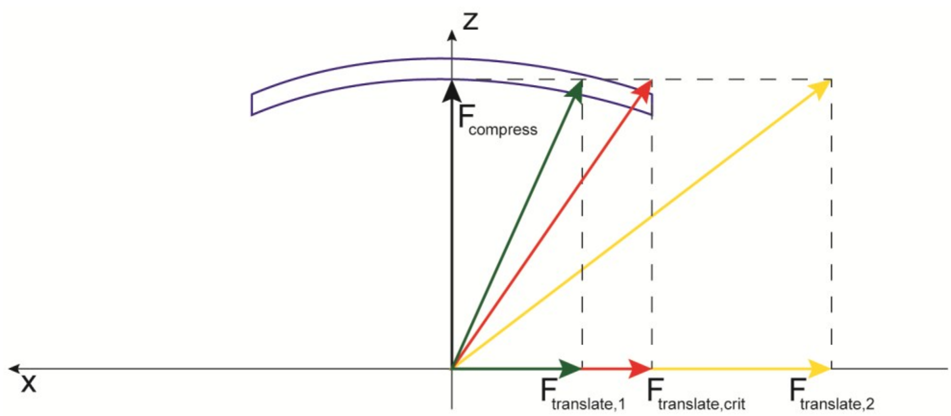


From the author

The calculation of the critical tangential force $F_{translate,crit}$ can be performed by means of a finite element model. The procedure involves the application of a compressive force, as defined in Section 3.3.2, on the humeral head that compresses it into the articular surface of the glenoid cartilage. Under sustained compression, the humeral head undergoes displacement in the directions illustrated in Figure 64, and the tangential forces generated during this displacement are recorded.

Figure 64 – Directions in which the humeral head translates. The variable $u$ represents the displacement in each direction.

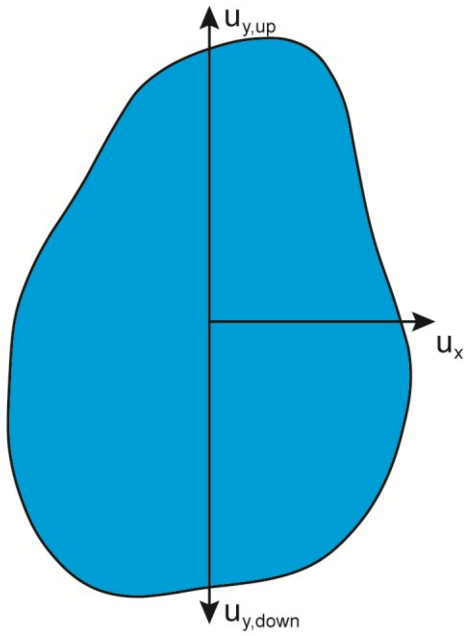


From the author.

The glenohumeral ratio $C_x$ is defined as the ratio between the maximum recorded tangential force in the $x$ direction and the applied compressive force. Similarly, the glenohumeral ratio $C_y$ is defined as the ratio between the maximum recorded tangential force in the $y$ direction and the applied compressive force. The value of the glenohumeral ratio is, however, dependent upon the value of the applied compressive force $F_{compress}$: the higher the value of $F_{compress}$, the lower the value of the glenohumeral ratio (HALDER *et al.*, 2001; KLEMT *et al.*, 2017). It is hypothesized that an increase in compressive force results in a flatter contact surface between the deformable cartilages, thereby reducing the constraint imposed by the curvature of the glenoid cartilage. Additionally, considering the ellipsoidal nature of the articular surfaces, the glenohumeral ratio becomes dependent on the abduction position. As the joint rotates during shoulder and arm movements, the congruency of contact between the ellipsoidal surfaces changes, altering the constraint potential of the glenoid cartilage's curvature.

For defect size 0 mm, the glenohumeral ratios $C_x, C_{y,up}$, and $C_{y,down}$ were calculated for abduction angles 30°, 60°, 90°, and 120°, using three different values for the compression forces for each abduction angle. The compressive forces values and dislocation's directions were based on outcomes from a previous study (JUNIOR *et al.*, 2022). The results are presented in Table 20, Table 21, Table 22, and Table 23. As the osseous defect are located at the anterior border of the glenoid, only the glenohumeral ratio $C_x$ was calculated for bone defects greater than 0 mm.

Table 20 – Maximum tangential forces for osseous defect size 0 mm.

| | **30°** | | | **60°** | | | **90°** | | | **120°** | | |
|---|---|---|---|---|---|---|---|---|---|---|---|---|
| $F_{compress}$ | $F_x$ | $F_{y,up}$ | $F_{y,down}$ | $F_x$ | $F_{y,up}$ | $F_{y,down}$ | $F_x$ | $F_{y,up}$ | $F_{y,down}$ | $F_x$ | $F_{y,up}$ | $F_{y,down}$ |
| 200 N | 52,74 | 81,65 | X | --- | --- | --- | --- | --- | --- | --- | --- | --- |
| 300 N | 72,22 | 115,9 | X | --- | --- | --- | --- | --- | --- | --- | --- | --- |
| 400 N | 89,4 | 148,1 | X | 89,91 | 146,3 | X | --- | --- | --- | --- | --- | --- |
| 500 N | --- | --- | --- | 105,4 | 175,7 | X | --- | --- | --- | 99,18 | X | 122 |
| 600 N | --- | --- | --- | 119,4 | 204,1 | X | 116,1 | 210,5 | 138,6 | 110,7 | X | 138,8 |
| 700 N | --- | --- | --- | --- | --- | --- | 128,3 | 220 | 154,2 | 123,1 | X | 154,3 |
| 800 N | --- | --- | --- | --- | --- | --- | 139,3 | 263,8 | 168,6 | --- | --- | --- |

Table 21 – Glenohumeral ratios for osseous defect size 0 mm.

| | **30°** | | | **60°** | | | **90°** | | | **120°** | | |
|---|---|---|---|---|---|---|---|---|---|---|---|---|
| $F_{compress}$ | $C_x$ | $C_{y,1}$ | $C_{y,2}$ | $C_x$ | $C_{y,1}$ | $C_{y,2}$ | $C_x$ | $C_{y,1}$ | $C_{y,2}$ | $C_x$ | $C_{y,1}$ | $C_{y,2}$ |
| 200 N | 0,264 | 0,408 | X | --- | --- | --- | --- | --- | --- | --- | --- | --- |
| 300 N | 0,241 | 0,386 | X | --- | --- | --- | --- | --- | --- | --- | --- | --- |
| 400 N | 0,224 | 0,370 | X | 0,225 | 0,366 | X | --- | --- | --- | --- | --- | --- |
| 500 N | --- | --- | --- | 0,211 | 0,351 | X | --- | --- | --- | 0,198 | X | 0,244 |
| 600 N | --- | --- | --- | 0,199 | 0,340 | X | 0,194 | 0,351 | 0,231 | 0,185 | X | 0,231 |
| 700 N | --- | --- | --- | --- | --- | --- | 0,183 | 0,314 | 0,220 | 0,176 | X | 0,220 |
| 800 N | --- | --- | --- | --- | --- | --- | 0,174 | 0,330 | 0,211 | --- | --- | --- |

Table 22 – Maximal tangential forces in the $x$ direction for osseous defect sizes 2 mm, 3 mm and 4 mm.

| | **2 mm** | | | | **3 mm** | | | | **4 mm** | | | |
|---|---|---|---|---|---|---|---|---|---|---|---|---|
| $F_{compress}$ | **30°** | **60°** | **90°** | **120°** | **30°** | **60°** | **90°** | **120°** | **30°** | **60°** | **90°** | **120°** |
| 200 N | 44,14 | --- | --- | --- | 37,5 | --- | --- | --- | 30,26 | --- | --- | --- |
| 300 N | 59,99 | --- | --- | --- | 50,55 | --- | --- | --- | 40 | --- | --- | --- |
| 400 N | 73,75 | 74,74 | --- | --- | 61,65 | 62,99 | --- | --- | 47,98 | 49,64 | --- | --- |
| 500 N | --- | 86,94 | --- | 82,07 | --- | 72,42 | --- | 68,24 | --- | 56,31 | --- | 52,05 |
| 600 N | --- | 97,75 | 97,18 | 91,74 | --- | 80,59 | 82,05 | 75,55 | --- | 61,68 | 63,86 | 56,43 |
| 700 N | --- | --- | 106,7 | 100,2 | --- | --- | 89,17 | 81,67 | --- | --- | 68,19 | 59,75 |
| 800 N | --- | --- | 115,1 | --- | --- | --- | 95,15 | --- | --- | --- | 71,57 | --- |

Table 23 – Glenohumeral ratio $C_x$ for osseous defect sizes 2 mm, 3 mm and 4 mm.

| | **2 mm** | | | | **3 mm** | | | | **4 mm** | | | |
|---|---|---|---|---|---|---|---|---|---|---|---|---|
| $F_{compress}$ | **30°** | **60°** | **90°** | **120°** | **30°** | **60°** | **90°** | **120°** | **30°** | **60°** | **90°** | **120°** |
| 200 N | 0,221 | --- | --- | --- | 0,188 | --- | --- | --- | 0,151 | --- | --- | --- |
| 300 N | 0,200 | --- | --- | --- | 0,169 | --- | --- | --- | 0,133 | --- | --- | --- |
| 400 N | 0,184 | 0,187 | --- | --- | 0,154 | 0,157 | --- | --- | 0,120 | 0,124 | --- | --- |
| 500 N | --- | 0,174 | --- | 0,164 | --- | 0,145 | --- | 0,136 | --- | 0,113 | --- | 0,104 |
| 600 N | --- | 0,163 | 0,162 | 0,153 | --- | 0,134 | 0,137 | 0,126 | --- | 0,103 | 0,106 | 0,094 |
| 700 N | --- | --- | 0,152 | 0,143 | --- | --- | 0,127 | 0,117 | --- | --- | 0,097 | 0,085 |
| 800 N | --- | --- | 0,144 | --- | --- | --- | 0,119 | --- | --- | --- | 0,089 | --- |